

Czech Technical University in Prague
Faculty of Electrical Engineering

Doctoral Thesis

February, 2023

Ing. Jan Cagán

Czech Technical University in Prague
Faculty of Electrical Engineering
Department of Measurement

***STRUCTURAL HEALTH MONITORING OF
CARBON COMPOSITE STRUCTURES BY
MEANS OF ELECTRICAL RESISTANCE
TOMOGRAPHY***

Doctoral Thesis

Ing. Jan Cagáň

Prague, *February, 2023*

Ph.D. program: P2612 Electrical Engineering and Information
Technology

Branch of Study: 2601V006 Measurement and Instrumentation

Supervisor: Prof. Ing. Radislav Šmíd, PhD.

Abstrakt

Monitorování životnosti konstrukcí z uhlíkového kompozitu je důležitá oblast pro stanovování životnosti těchto konstrukcí v rámci přístupu *damage tolerance*, a to zejména v oblasti letectví. Tato dizertační práce studuje možnosti využití elektrické odporové tomografie pro účely monitorování životnosti konstrukcí z uhlíkového kompozitu.

Elektrická odporová tomografie je metoda pro zobrazení prostorového rozložení elektrické vodivosti na základě měření okrajových napětí při buzení objektu elektrickým proudem. Tento inverzní problém je špatně určený a výsledné prostorové rozlišení elektrické vodivosti vymezuje použitelnost tomografie pouze pro určité aplikace.

Pozornost je zaměřena především na detekovatelnost sotva viditelných impaktů, které jsou jednou z nejsledovanějších vad. Dále je také věnována pozornost detekovatelnosti praskliny. Vedle experimentálního hodnocení detekovatelnosti je v rámci práce vyvinuto úsilí aplikovat nástroje pro zlepšení obrazové rekonstrukce, konkrétně aplikace anizotropního Gaussova filtru v případě rekonstrukce praskliny, nebo obecně optimalizace rozložení a velikosti elektrod.

Klíčová slova: elektrická odporová tomografie, kompozit vyztužený uhlíkovými vlákny, monitorování životnosti konstrukce, sotva viditelný impakt, poškození typu trhliny, anizotropní Gaussovo vyhlazování, hodnocení detekčních schopností, optimalizace polohy elektrody, přístrojové vybavení elektrické odporové tomografie

Abstract

Structural health monitoring of carbon composite structures is an important area for determining the lifetime of these structures within the damage-tolerant approach, especially in the aerospace domain. This thesis studies the possibilities of using electrical resistance tomography for the purposes of monitoring the lifetime of carbon composite structures.

Electrical resistance tomography is a method for imagining the spatial distribution of electrical conductivity based on the measurement of boundary voltages when an object is excited by an electric current. This inverse problem is ill-posed, and the resulting spatial resolution of electrical conductivity limits the applicability of tomography to only specific applications.

Attention is mainly focused on the detectability of barely visible impacts, one of the most monitored defects. Attention is also paid to the detectability of the crack. In addition to the experimental evaluation of detectability, efforts are made within the work to apply tools to improve image reconstruction, specifically the application of an anisotropic Gaussian filter in the case of crack reconstruction or, in general, the optimization of the distribution and size of the electrodes.

Keywords: electrical resistance tomography, carbon fiber reinforced composite, structural health monitoring, barely visible impact damage, crack damage, anisotropic Gaussian smoothing, detection capability assessment, electrode position optimization, electrical resistance tomography instrumentation

Declaration of authorship

I hereby declare I have written this thesis independently and have quoted all the sources of information used in accordance with the methodological instructions on ethical principles for writing an academic thesis. Moreover, I state that this thesis has neither been submitted nor accepted for any other degree.

In Prague

Acknowledgement

I am incredibly grateful to my supervisor Prof. Ing. Radislav Šmíd, PhD for his invaluable advice, continuous support, and patience during my Ph.D. study. I would also like to thank all the members of the VZLU for their kind help and support that have made my study a wonderful time. Finally, I would like to thank my parents, wife, and children. Without their tremendous understanding and encouragement over the past few years, it would be impossible for me to complete my study.

Contents

1	Introduction	10
1.1	Structural health monitoring of composite structures	10
1.2	Electrical Impedance Tomography	11
1.2.1	Geophysics	11
1.2.2	Process and chemical industries	11
1.2.3	Medicine	11
1.2.4	Structural health monitoring and other sensors	11
1.3	Motivation	12
2	State-of-the-art: Spatial conductivity image reconstruction	13
2.1	Inverse problem	13
2.1.1	Statistical inversion	14
2.1.2	Deterministic inversion	15
2.1.3	Tikhonov regularization	15
2.1.4	NOSER	16
2.1.5	Laplace's second-order high pass filter	16
2.1.6	Gaussian isotropic high-pass filter	16
2.1.7	Total variation regularization	17
2.1.8	Sensitivity matrix calculation	17
2.2	Forward problem	18
2.2.1	Forward problem formulation	18
2.2.2	Formulation of the solution using the finite element method	19
3	The aim of the work	22
3.1	Development of instrumentation and realization of experimental coupons	22
3.2	An evaluation of the detection capabilities of the ERT in the area of the BVID impact	22
3.3	Improvement of the detection capabilities of the ERT in case of crack damage	22
3.4	Optimization of electrode position and shape towards a BVID impact detection	22
4	Hardware implementation of ERT in the field of CFRP composites	23
4.1	Stimulation and measurement pattern	23
4.2	Hardware implementation of current stimulation and boundary voltage measurement	24
4.2.1	Experimental facilities	25
4.2.2	Electrode Implementation	31
5	Detection capability of ERT in case of BVID	33
5.1	Barely visible impacts	33
5.1.1	BVID structure	33
5.2	ERT setting for BVID detection	33
5.2.1	Forward and inverse model	34
5.3	Implementation of the experiment	36
5.4	BVID detection capability assessment	37
5.4.1	Position error	37
5.4.2	Amplitude response	38

6	Crack detection capability of ERT	44
6.1	Anisotropic Gaussian smoothing filter	44
6.1.1	Experimental verification of crack detection filter	45
6.1.2	Assessment of Gaussian anisotropic filter for crack detection	46
7	Optimization of electrode position and shape	53
7.1	Motivation to optimize electrode position and shape	53
7.2	Selection of tools and model parameters	54
7.2.1	Optimization scheme	54
7.2.2	Data representation of solution	55
7.2.3	Mutation operator	55
7.2.4	Crossover operator	55
7.2.5	Genetic algorithm	56
7.3	Numerical experiments	57
7.4	Experiments on a coupon with resistive network	63
7.4.1	Experimental coupon	63
7.4.2	Performed measurements and evaluations	63
7.4.3	Optimization usefulness evaluation	67
8	Discussion and further steps	69
8.1	Implementation and instrumentation of ERT	69
8.2	Barely visible impact detection	69
8.3	Crack detection	69
8.4	Optimization of electrode parameters	70
9	Conclusion	71
9.1	Instrumentation and experimental coupons	71
9.2	Detectability of BVID impact	72
9.3	Crack detectability	72
9.4	Selection of electrode position and size in case of BVID impact	72
	Bibliography - author's impacted articles	73
	Bibliography - other	74
A	Example of GA population	78
A.1	Position of inhomogeneity in the CENTER	79
A.2	Position of inhomogeneity on the TOP	80
A.3	Position of inhomogeneity on the LEFT	81
A.4	Position of inhomogeneity on the RIGHT	82

List of Figures

4.1	Example of the opposite stimulation pattern and the adjacent measurement pattern.	24
4.2	Block diagram of single and multi-current ERT system.	25
4.3	Block diagram of modular ERT system.	26
4.4	Block diagram of the 4x32 multiplexer.	27
4.5	Block diagram of stimulation, measurement, and post-processing.	27
4.6	Frequency spectrum of the measured signal on an intact specimen.	28
4.7	PXI measurement system and resistor network coupon.	29
4.8	Program window for tomographic measurements by means of PXI.	30
4.9	Diagram and photo of the cut between CFRP and conductor.	32
4.10	Circular composite coupon and measured contact resistance variations.	32
5.1	Measured boundary voltage potentials of typical specimens.	34
5.2	Differential boundary voltages of the coupon damaged by BVID.	35
5.3	A portion of the set of CFRP specimens of dimensions 150×100 mm with 24 electrodes.	36
5.4	An example of BVID.	37
5.5	Histograms of the position errors of the specimens with drilled thru-holes.	40
5.6	An example of the statistical model and relevant POD curve.	42
6.1	Filter setup according to the nominal position.	46
6.2	Set of CFRP specimens.	50
6.3	An example of the boundary voltages across the laminate stacking sequences.	51
7.1	Distribution map of damage to the fuselage.	53
7.2	Initial electrode configuration.	57
7.3	Fitness functions of the optimization without restriction.	58
7.4	Fitness functions of the optimization with restriction.	58
7.5	The image reconstructions of the point inhomogeneities.	59
7.7	Changes in the values of the position errors.	60
7.6	Fitness functions of the best candidates after 500 generations.	60
7.8	Changes in the normalized values of the electrical conductivity in COG.	61
7.9	Changes in the blur radius.	61
7.10	Fitness functions of the configuration with inhomogeneity at the top without restriction.	62
7.11	Experimental coupon based on the resistor network.	63
7.12	Verification of the model by comparing the boundary voltages.	64
7.13	Example of measured boundary voltages of the point inhomogeneity.	65
7.14	Example of reconstructions of point inhomogeneities.	66

List of Tables

4.1	Comparison of key parameters of the PXI system and the modular system.	29
5.1	The dent depths in relation to impact energy and stacking sequence.	34
5.2	BVID photos in detail at three observed energies.	38
5.3	Comparison of amplitude responses of drilled THRU-HOLES and BVID.	39
5.4	Estimates of regression parameters and the POD for the BVID damage (quasi-isotropic case).	39
5.5	Estimates of regression parameters and the POD for the BVID damage (orthotropic case).	41
5.6	Estimates of regression parameters and the POD for drilled thru-hole damage.	41
5.7	Overview of typical reconstructions across individual stacking sequences and image priors.	43
6.1	Values of the parameters of the Gaussian anisotropic smoothing filter.	45
6.2	Cross-correlation coefficients in the isotropic smoothing case.	47
6.3	Cross-correlation coefficients in the anisotropic smoothing case.	47
6.4	Percentage changes in the solution error for individual cut damages.	47
6.5	Solution error of the isotropic and anisotropic smoothing (cut on the right side).	48
6.6	Solution error of the isotropic and anisotropic smoothing (cut on both sides).	48
6.7	Examples of the images obtained by the isotropic and anisotropic smoothing filters.	49
6.8	Reconstruction error with cross-correlation for different assumptions about crack position and direction.	52
7.1	Positions of point inhomogeneities (relative to the coupon center).	57
7.2	Position of applied inhomogeneities in the further experimental verification of the impact of optimization.	64
7.4	Reconstruction error for homogeneity at left and right positions in combination with appropriate focus.	67
7.5	Position errors (mm) for homogeneity at the left and right positions in combination with the appropriate focus.	67
7.3	Position of applied inhomogeneities in further experimental verification of the impact of optimization.	68

List of Abbreviations

BCM	Basis Constraints Method.
BSF	Best So Far.
BVID	Barely Visible Impact Damage.
CEM	Complete Electrode Model.
CFRP	Carbon Fibre Reinforced Composite.
CNT	Carbon Nanotube.
ECT	Electrical Capacitance Tomography.
EIT	Electrical Impedance Tomography.
EITS	Electrical Impedance Tomography Spectroscopy.
ERT	Electrical Resistance Tomography.
FEM	Finite Element Method.
GA	Genetic Algorithm.
GCM	Grouping Constraints Method.
GHP	Gaussian High-Pass filter.
GREIT	Graz consensus reconstruction algorithm for EIT.
HA	Half Amplitude set.
LHP	Laplace 2nd-order High-Pass.
MAP	Maximum Aposteriory Probability.
MCMC	Monte Carlo Markov Chain.
ML	Maximum Likelihood.
MS	Minimal Square.
NDT	Non-Destructive Testing.
NOSER	Newton's One-Step Error Reconstructor.
POD	Probability Of Detection.
PXI	PCI eXtensions for Instrumentation.
SHM	Structural Health Monmitoring.
SVD	Singular Value Decomposition.
TIK	Tikhonov.
TSVD	Truncated Singular Value Decomposition.
TV	Total Variation.
UGW	Ultrasonic Guided Waves.
XC	Cross Corelation.

Chapter 1

Introduction

1.1 Structural health monitoring of composite structures

Non-destructive testing (NDT) and structural health monitoring (SHM) are important aspects across the industry due to the properties of the carbon composite. One of the important industries is aerospace, where NDT and SHM play a key role in the design method *damage-tolerant* and *safe-life*. These design methods assume that a structure can undergo certain operational loads even in the presence of defects that develop during its life cycle, and this development is monitored through periodic inspection checks by NDT or continuously by SHM.

Composite structures are widely used in aerospace due to their advantages of low weight, high stiffness, and high strength. Considerable effort has gone into the development of NDT and SHM methods. One of the reasons for this is, among others, that the cost of regular inspections of composite structures exceeds the cost of structures made of previously common materials (duralumin) many times over. The most basic and oldest NDT method is a visual inspection and tapping inspection, and thus based on mechanical and optical principles. More modern methods are mainly based on the principle of mechanical vibration, acoustic or thermographic. The basic divisions and the brief list in the previous paragraph are general. If we focus specifically on the aviation segment, for example, acoustic emission dominates, which by its very nature is capable of detecting a defect at its inception, but its resistance to a noisy environment is low. Another widely used method in the field of acoustic waves is ultrasonic testing or ultrasonic guided waves (UGW), which are at a high technological readiness level. Ultrasonic testing is exclusively used for NDT. However, UGW-assisted testing is already being sought to be used for continuous monitoring. Due to the sensitivity of UGW to the operating vibrations of the structure, monitoring is always performed at rest (offline), so we cannot speak of an online method.

Electromagnetic methods are also an integral part of the overall list of NDT tools. The fundamental division of imaging methods can be made according to the direction of propagation of the energy of the quantity on which the imaging method (so-called modality) is based. In the case of a constant direction of propagation from the source to the sensor, we speak of so-called "hard field" tomography, while in other cases, where the direction depends on the physical properties of the medium, it is "soft field" tomography. The group of "hard field" tomography is mainly represented by well-known medical methods such as X-ray (micro) tomography [1], magnetic resonance [2], or positron emission tomography [3]. The group of so-called "soft field" tomographic methods includes electrical capacitance tomography (ECT), electrical resistance tomography (ERT), electrical impedance tomography (EIT), microwave tomography [4], diffuse optical tomography [5], or magnetic induction tomography [6]. Magnetic induction tomography is otherwise known in the field of NDT as eddy current tomography. By combining individual modalities into multimodal tomography, images with high information value can be achieved. An example is magnetic resonance impedance tomography [7].

The aforementioned electrical resistivity tomography has recently been of interest in the field of structural health monitoring of carbon composite structures. A significant advantage of ERT over the methods in the paragraph above is its ability to on-line monitoring of the object of interest. Comparing the hardware requirements with the other methods, it can be concluded that ERT is a less demanding method, especially in the sensor part. The low sensor requirements allow the method to use *in-situ*. The fact that the method falls into the "soft field" category also puts it in the non-invasive category. However, due to the need for the direct contact of the electrodes with the carbon conducting fibers, the method distorts the object being measured and, therefore, further categorizes it as an intrusive method. A fundamental feature of ERT is the

low resolution of the conductivity image, which is due to the fact that the inverse problem of the image reconstruction is ill-defined. This is due to both the poor ratio of the known (boundary voltages and excitation currents) and unknown (pixels or voxels of the electrical conductivity image), but also the nonlocal nature of the electrical conductivity.

1.2 Electrical Impedance Tomography

Electrical impedance tomography is generally used to display the spatial distribution of electrical impedance. The display or reconstruction of the conductivity image is based on the knowledge of the values of the electric current flowing through the object under observation and the electric voltage measured most often at the accessible edges of the object under observation. The method is also sometimes referred to as general probing. In many cases, either the real component of the impedance is imaged, the aforementioned ERT, or the imaginary component, the ECT. A special use case of EIT is then in spectroscopy (EITS), where the frequency dependence of the conductance is used to identify the inhomogeneity of interest [8].

As EIT is at a low level of technological readiness level in the field of SHM, the following section will present the state of the art in other areas where EIT is used, focusing on assessing the technological maturity in each area.

1.2.1 Geophysics

Geophysics is one area where ERT has been widely used in recent years, as soil conductivity is affected by several factors that are desirable to monitor. Factors affecting conductivity include particle mineralogy, groundwater content, nature of the electrolyte, porosity, and of course, the inherent resistivity of the material. One of the most practical applications is in monitoring landslides [9].

1.2.2 Process and chemical industries

The process industry uses this type of tomography in several areas. These are mainly in mixing, separation, pipe conveying, and chemical reactors. In the case of mixing, the effects of rotor type, temporal and spatial variations of solids or multiphase mixtures, and, in general, the development and verification of mixing models are monitored. In the case of separation, tomography is applied to monitor the flow of the medium in hydrocyclones to identify its regime. In the case of pipe conveyors, tomography is used to measure the flow rate and flow regime of multiphase mixtures. Just as ERT has been used in previous cases to monitor the flow regime, it is also used for this purpose in the case of chemical reactors. Further applications in this area are possible in cases where the chemical process being monitored significantly affects the conductivity, e.g., in the case of polymerization of certain substances.

1.2.3 Medicine

In medicine, EIT has applications in several areas. For example, in gastroenterology, tomography is used to monitor gastric emptying [10]. Another everyday use case is the diagnosis of blockages in the cerebral arteries, as brain tissue changes its conductivity dramatically depending on oxygenation [11]. Another important use case is the diagnosis of breast cancer [12], where tomography solves both significant problems of the commonly used X-ray mammography, and thus the cost and harmfulness of the method. The last widely used area is lung monitoring for diagnosing lung oedema, apnoea, or cancer [13].

1.2.4 Structural health monitoring and other sensors

The above-mentioned essential characteristics of this type of tomography (ability to measure online, *in-situ* and non-invasively) go against the applications in structural health monitoring or sensors used in this and related fields. One of the first researches dealing with the application of ERT, specifically in the field of carbon composites (CFRP), was carried out by Baltopoulos and his collective [14], followed by the works of other authors [15, 16, 17, 18]. Other works on this topic can be found only minimally. More works can be found in the field with a related material namely carbon nanotube composite CNT, e.g. see the works [19, 20, 21, 22, 23, 24, 25, 26]. The above papers, whether working directly on CFRP or CNT, deal with experimental studies of the detectability of ERT in various situations. In most cases, the experiments are performed on a single sample.

1.3 Motivation

The motivation for this work is the potential of the ERT, which stems from the benefits mentioned above. Specifically, the high temporal resolution and low sensing requirements allow sensors to be built directly into the structure to monitor defects as they occur. The main disadvantage of ERT, the low spatial resolution, could discourage the intention to use the method for monitoring the lifetime of structures. However, it is important to consider the nature of SHM systems, which are synonymous with early warning systems. Knowing the exact shape of the defects being monitored is not necessarily necessary to meet the early warning requirement. For an immediate assessment of the level of risk, it is only required to know the probable location and likely extent of the emerging defect. For this reason, investigating the detection capabilities described in this paper is an essential step in approaching the deployment of ERT for SHM of composite structures.

However, the journey to the operational deployment of the method is quite long at this point. The technological readiness level of ERT is generally low, especially in the area of SHM/NDT. For example, in the medical field, the method is currently deployed sporadically for experimental verification of first prototypes. It is at a higher level in the manufacturing industry or geophysics. There are a number of fundamental problems in the deployment of the method for SHM/NDT. In addition to the more practical issue of implementing electrodes suitable for eventual mass production and field conditions, there is the broad topic of detection capabilities. The investigation of the detection capability is a crucial step that will further allow a proper marketing study to be carried out based on a defined set of potential use cases. Investigating detection capability is a daunting task due to the vast number of composite configurations combined with the large number of defect types that can occur in these materials. The numerous design variations are primarily due to a large number of carbon fiber types, the variety of fabrics, and ultimately the number of compositions that can be assembled from the fabrics based on the design requirements. The correlation of the multitude of design variations with detection capabilities is through the resulting conductivity of the composite part, which, combined with the magnitude of the change in conductivity due to defects, affects the signal-to-noise ratio on which the detection capabilities subsequently depend. The resulting conductivity is also influenced by the manufacturing process technology. Another relatively significant influence on conductivity, and therefore on the resulting sensitivity, is due to the mechanical bonding of the composite to the conductive parts of the structure via rivets or screws, which has not been investigated to date. Considering the low technological readiness level of ERT, all investigations in this work are carried out at the lowest level in terms of the *building block approach* [27], which sets out a systematic procedure for testing composite materials from primary samples (coupons), through individual components, to whole structural components.

Two types of defects are considered in this work. Impact in the barely visible area (BVID) and crack. The barely visible impact comes from a low-velocity impact. In terms of the aforementioned philosophy, *damage-tolerant* is one of the three fundamental defects considered and the most serious. The reason for the severity is primarily the immediate loss of static strength and the subsequent development and propagation of other defects from the impact site. This type of damage results from the crushing of the matrix and fibres of the composite by the contact force. The displacement of the material by the contact force leads to the formation of multiple delaminations due to interlaminar shear failures. The magnitude and location of the impact is determined by the stacking sequence of the composite, the material properties of the components used and, naturally, the energy of an impact. In most cases, the composite matrix is damaged to a greater extent and the fibers themselves to a lesser extent. Damage to the matrix then leads to a loss of the ability to stabilize the composite in compression. This is what makes BVID such a critical damage [27].

There are several ways in which defects can spread from the point of impact. Since ERT, in the case of CFRP composite, is mediated only by the conductivity of the fibers, it makes sense to focus only on those propagation modes that are related to the conductivity of the fibers, i.e. delamination or cracking.

Delamination will be further observed by investigating the detection capabilities of the BVID impact on a real defect. In contrast, the crack will be monitored through a coarse simulation using a milled groove through the specimen thickness.

Chapter 2

State-of-the-art: Spatial conductivity image reconstruction

The reconstruction of the electrical conductivity image is known in mathematics as the Calderón problem. It is an inverse problem of determining the electrical conductivity inside a medium by measuring the currents and voltages at its boundaries. It is a difficult problem mainly due to the scattering of the current field in the medium. Compared to classical x-ray computed tomography, where the attenuation of radiation is affected only by the mass standing in the path of the passing radiation, the magnitude of the current field is affected by a large part of the volume. These nonlocal properties of the current field are not the only obstacle, as the problem of reconstructing the conductivity image is inherently ill-posed, which, combined with the often low ratio of known to unknown variables, leads to a diffuse nature of the image. In particular, the ill-posedness of the image reconstruction problem manifests itself in the fact that arbitrarily large conductivity variations may occur in the image that cannot be detected by a boundary measurement. This fundamental problem is overcome by incorporating an assumption about the distribution of the conductivity or an assumption about its changes in the regularization of the inverse problem.

2.1 Inverse problem

The ERT inverse problem can be generally described as the determination of all parameters of a quasi-static electric field model that cannot be directly measured, based on a limited set of measurable parameters. The opposite of the inverse problem is the forward problem, which determines the set of measurable parameters based on arbitrary parameters of the field model (see section 2.2). The fundamental division of methods for solving inverse problems is into statistical and deterministic, with the deterministic ones being based on the statistical ones. Statistical methods are generally based on a Bayesian interpretation of probability, which evaluates given information as a measure of knowledge that it is true.

For the purpose of Bayesian inversion, it is helpful to distinguish the model space \mathcal{M} , the data space \mathcal{D} , and the space of physical parameters $\mathcal{F} = \mathcal{M} \times \mathcal{D}$. In this case, the model space is given by the quasi-static electric field described by the model parameter vector \mathbf{m} . The data space is given by the measurable parameters of the model \mathbf{d} (boundary voltages). The physical parameter space is then provided by the measured data of the corresponding models $\mathbf{f} = (\mathbf{m}, \mathbf{d})$. The essential sources of information that enter into the solution of the inverse problem within the statistical approach are the physical laws, the measured data, and also the assumption about the solution.

The Bayesian approach is based on the refinement of the initial assumption based on the knowledge of the model and observations (measurements) using the conditional probability $\sigma(\mathbf{m}|\mathbf{d})$ over the model \mathcal{M} expressed by a posteriori probability

$$\sigma(\mathbf{m}|\mathbf{d}) = \frac{\rho(\mathbf{d}|\mathbf{m})\Theta(\mathbf{m})}{\mu(\mathbf{d})}, \quad (2.1)$$

where the expression $\Theta(\mathbf{m})$ is called the a priori probability density or prior. The prior gives an initial estimate of the probability distribution of the indirectly observed states of the system and is independent of the measured data. The basic assumption is that the electrical conductivity will always be positive. It is also, e.g., a knowledge of the environment where the ERT is deployed; therefore, specific values of either homogeneous conductivity or the inhomogeneities sought can be assumed. The probability density

of the measured data $\mu(\mathbf{d})$ is another source of information for the solution, which gives some measure of information about the measurable parameters of the model. The last term $\rho(\mathbf{d}|\mathbf{m})$ is a likelihood function that is based on a forward physical model and gives the likelihood density for certain model parameters.

2.1.1 Statistical inversion

The Bayesian approach to the inverse ERT problem given by 2.1 is general. The specific solution consists in transforming the information from the data space \mathcal{D} into the model space \mathcal{M} by expressing the probability of the specific data of the model $\mathcal{M}_1 \in \mathcal{M}$ as follows

$$P(\mathbf{m} \in \mathcal{M}_1) = \int_{\mathcal{M}_1} \sigma(\mathbf{m}|\mathbf{d}) d\mathbf{m} \quad (2.2)$$

A common and intuitive way of understanding information, in this case, is point estimates and their reliability. The most commonly used estimators in inverse problems are the maximum a posterior probability (MAP), maximum likelihood (ML), and minimum squared deviation (MS) estimators.

Maximum likelihood estimation seeks the most likely combination of model parameters. However, its main disadvantage is that it does not guarantee a unique maximum. This is mainly because it is performed by point estimation over a Bayesian approach, which combines the entire probability distributions (from the three sources of information mentioned above), not the point information. The significant feature here is the prior, which is the source of the regularization. From a posterior probability 2.1, the estimator can be expressed in general as follows

$$\mathbf{m}_{MAP} = \min_{\mathbf{m} \in \mathcal{M}} \sigma(\mathbf{m}|\mathbf{d}). \quad (2.3)$$

A maximum likelihood estimate is a special case of MAP estimation that considers a prior with a uniform probability distribution. It is, therefore, an estimator without regularization. Express it in general as follows

$$\mathbf{m}_{ML} = \min_{\mathbf{m} \in \mathcal{M}} \sigma(\mathbf{m}|\mathbf{d}). \quad (2.4)$$

The last well-known single-point estimator is the minimum squared error estimator. It can be expressed as follows

$$\mathbf{m}_{MS} = E[\sigma(\mathbf{m}|\mathbf{d})]. \quad (2.5)$$

The confidence level of the point estimate can be expressed using the covariance of a posteriori probability as follows

$$\mathbf{C}_{\mathbf{m}|\mathbf{d}} = \int_{\mathcal{M}} (\mathbf{m} - \mathbf{m}_{MS})(\mathbf{m} - \mathbf{m}_{MS})^T \sigma(\mathbf{m}|\mathbf{d}) d\mathbf{m}. \quad (2.6)$$

However, the a posteriori covariance is most informative when the a posteriori probability density is close to a Gaussian distribution. This is not the only reason why the next derivation is based on the assumption that the probability distributions are Gaussian, since the introduction of this assumption also leads to a simplification of a posterior probability 2.1 to an analytical expression of the estimates of \mathbf{m}_{MAP} or \mathbf{m}_{ML} .

If model errors and measurement errors are assumed to be independent, additive, and with a Gaussian probability distribution with zero mean and covariance, the likelihood function of the forward model can be expressed as

$$\rho(\mathbf{d}|\mathbf{m}) = \exp \left\{ -\frac{1}{2}(\mathbf{d} - h(\mathbf{m}))^T \mathbf{C}_v^{-1}(\mathbf{d} - h(\mathbf{m})) \right\}, \quad (2.7)$$

while the a posteriori probability is as

$$\sigma(\mathbf{m}|\mathbf{d}) \propto \exp \left\{ -\frac{1}{2}(\mathbf{d} - h(\mathbf{m}))^T \mathbf{C}_v^{-1}(\mathbf{d} - h(\mathbf{m})) - \frac{1}{2}(\mathbf{m} - \mathbf{m}_0)^T \mathbf{C}_m^{-1}(\mathbf{m} - \mathbf{m}_0) \right\}, \quad (2.8)$$

where $h(\mathbf{m})$ is the forward model operator, \mathbf{C}_ν is the covariance matrix of the measurement noise, and \mathbf{C}_m is the covariance matrix of the model parameters. By maximizing the likelihood function 2.7 and the a posteriori likelihood 2.8, the expression of the estimates of \mathbf{m}_{MAP} or \mathbf{m}_{ML} can be obtained as follows

$$\mathbf{m}_{ML} = \operatorname{argmin} \frac{1}{2}(\mathbf{d} - h(\mathbf{m}))^T \mathbf{C}_\nu^{-1}(\mathbf{d} - h(\mathbf{m})), \quad (2.9)$$

$$\mathbf{m}_{MAP} = \operatorname{argmin} \frac{1}{2}[(\mathbf{d} - h(\mathbf{m}))^T \mathbf{C}_\nu^{-1}(\mathbf{d} - h(\mathbf{m})) + (\mathbf{m} - \mathbf{m}_0)^T \mathbf{C}_m^{-1}(\mathbf{m} - \mathbf{m}_0)]. \quad (2.10)$$

2.1.2 Deterministic inversion

The deterministic approach, unlike the statistical approach, seeks the distribution of the parameters of the model \mathbf{m} only by mapping the experimental data \mathbf{d} using the forward model $h(\mathbf{m})$, and hence $h(\mathbf{m}) - \mathbf{d} = 0$. Such a straightforward approach leads to no solution due to modeling inaccuracies or measurement errors. The inverse problem is ill-defined according to Hadamard's evaluation criteria, and thus

- a solution may not exist,
- a solution may be ambiguous,
- perturbations in the measurement can cause significant changes in the solution.

Note The singular decomposition (SVD) of the linearized forward operator $h(\mathbf{m})$, or eigenvalue analysis (conditionality), is often used to measure how badly the inverse problem is determined. The worse the inverse problem is determined, the sooner the eigenvalues of the forward operator drop. In addition to determinacy analysis, it is also possible to use SVD as a tool to perform regularized inversion by using a truncated decomposition (TSVD), see for example [28]. This is further exploited with the NOSER prior (2.1.4).

Deterministic approaches are often special cases of more general statistical cases. For example, the maximum likelihood-based ML estimator (2.9) is equivalent to the ordinary least squares-based inverse 2.11 in the case where all distributions have a Gaussian distribution with the same variance $\mathbf{C}_\nu^{-1} \sim \mathbf{I}$.

$$\mathbf{m}_{LS} = \operatorname{argmin} \|h(\mathbf{m}) - \mathbf{d}\|^2 \quad (2.11)$$

Whether the inverse problem is viewed statistically or deterministically, some a priori information is always introduced into the inverse solution as part of the regularization being performed, either implicitly or explicitly. There are a number of ways to introduce a priori information. For example, the clustering method (GCM, see [29]), where a certain conductivity is assumed for previously known regions, and conductivity is sought only in a limited region. If this region with the searched conductivity has sufficient sensitivity, the inverse problem can be formulated using LS estimation without regularization. A significant drawback of this solution is the tendency of most solutions to fall back on assumptions, which, if inaccurate with respect to reality, may lead to a degradation of the result. This problem is eliminated by the method of basis constraints (BCM, see [30]), which is related to the GCM method. Here the assumption is formulated using basis functions (or eigenvectors) so that a larger number of specific estimates can be bent, which allows overcoming the problems of strict assignment of a single assumption. Similarly, it is possible to introduce a priori information in the framework of Tikhonov's regularization of [31] (see the section below). Moreover, it is possible here to control the "credibility" of an assumption by a regularization parameter.

In the following sections, all the methods of inversion (or regularization and its method of introducing a priori information into the inversion) used in this study will be discussed. These are exclusively basic "smoothing" regularizations.

2.1.3 Tikhonov regularization

A widely used inversion that ranks among deterministic inversion methods is Tikhonov regularization (TIK)

$$\mathbf{m}_{\alpha,L} = \operatorname{argmin} \|\mathbf{J}\mathbf{m} - \mathbf{d}\|^2 + \alpha \mathbf{F}(\mathbf{m}), \quad (2.12)$$

where \mathbf{J} is the linearized forward operator of the nonlinear operator $h(\mathbf{m})$ (the so-called Jacobian, see Chapter 2.1.8), $\mathbf{F}(\mathbf{m}) \geq 0$ is the regularization functional and $\alpha \geq 0$ is the regularization parameter (Tikhonov factor). The Tikhonov regularization is based on an estimate of the maximum a posteriori MAP

probability (2.10) under the same assumptions as the least squares method mentioned above, implicitly incorporating a priori information about the model, again with a Gaussian distribution $\mathbf{L}^T \mathbf{L} \sim \mathbf{C}_m^{-1}$, where \mathbf{L} is the regularization matrix within the regularization functional, which in this case is often chosen as

$$\mathbf{F}(\mathbf{m}) = \|\mathbf{L}(\mathbf{m} - \mathbf{m}_0)\|, \quad (2.13)$$

where \mathbf{m}_0 is an a priori estimate of the search parameters of the model \mathbf{m} . The functional is then obtained as 2.14 or the regularized solution 2.15.

$$\mathbf{m}_{\alpha, \mathbf{L}} = \operatorname{argmin} \|\mathbf{J}\mathbf{m} - \mathbf{d}\|^2 + \alpha \|\mathbf{L}(\mathbf{m} - \mathbf{m}_0)\|, \quad (2.14)$$

$$\mathbf{m}_{\alpha, \mathbf{L}} = (\mathbf{J}^T \mathbf{J} + \alpha \mathbf{L}^T \mathbf{L})^{-1} (\mathbf{J}^T \mathbf{d} + \alpha \mathbf{L}^T \mathbf{L} \mathbf{m}_0). \quad (2.15)$$

After introducing simplifying assumptions given by the zero initial value of the search parameters of the model $\mathbf{m}_0 = 0$ and the regularization matrix $\mathbf{L} = \mathbf{I}$, it is possible to obtain one of the simplest forms of Tikhonov regularization, the so-called standard

$$\mathbf{m}_{\alpha, \mathbf{I}} = (\mathbf{J}^T \mathbf{J} + \alpha \mathbf{I})^{-1} \mathbf{J}^T \mathbf{d}. \quad (2.16)$$

The cases when the regularization matrix \mathbf{L} is sparse are considered as generalized Tikhonov regularization. The diagonal elements of the regularization matrix correspond to the variance of each image element, while the off-diagonal elements express the degree of correlation between the image elements. Therefore, these matrices are often chosen to perform the function of an image filter using a first or second differential operator. Thus, from the point of view of eigenvalue analysis, higher singularities are penalized, thus smoothing the solution. Therefore, these operators are called smoothing operators.

2.1.4 NOSER

Prior NOSER (Newton's One-Step Error Reconstructor [32]) is based on Newton's method of least squares estimation 2.11. A closer look at the derivative in the framework of Newton's method shows that the elements of the derivative matrix i and j that are close to each other are dominant and have a similar impact on the inversion result, while elements far apart affect the result much less. Thus, the elements on the diagonal and close to them have the main impact on the inversion result. Based on these facts, the NOSER prior was designed as follows

$$\mathbf{L} = \sqrt{\operatorname{diag}(\mathbf{J}^T \mathbf{J})}. \quad (2.17)$$

2.1.5 Laplace's second-order high pass filter

The most common choice is the second-order differential operator, the Laplace operator, or its discrete approximation to a piecewise continuous function. Each image element is then the sum of adjacent image elements. For the square inverse model network, the priors matrix is then obtained by convolution with the kernel

$$\begin{bmatrix} -1 & -1 & -1 \\ -1 & 8 & -1 \\ -1 & -1 & -1 \end{bmatrix}, \text{ or } \begin{bmatrix} 0 & -1 & 0 \\ -1 & 4 & -1 \\ 0 & -1 & 0 \end{bmatrix}. \quad (2.18)$$

On an irregular finite element mesh, the operator is then defined by -1 for adjacent elements and a value of 3 on a 2D element or 4 on a 3D element.

2.1.6 Gaussian isotropic high-pass filter

The isotropic Gaussian high-pass filter [33] comes directly from the definition of the MAP estimator (see 2.10). Here, the a priori information is carried in the covariance matrix \mathbf{C}_ν . The diagonal elements correspond to the assumed variance and the off-diagonal elements reflect the correlation r between the image elements $\mathbf{C}_{\sigma_{ij}} = r \sqrt{\mathbf{C}_{\sigma_{ii}} \mathbf{C}_{\sigma_{jj}}}$. Based on the assumptions about the structure and distribution of the conductivity, a regularization matrix $\mathbf{L}^T \mathbf{L} \sim \mathbf{C}_m^{-1}$ can be constructed. However, the inversion of the covariance matrix constructed in this way is ill-determined and thus highly unstable. Since the regularization performed in this way exhibits the behavior of a low-pass filter, the covariance matrix can be

viewed as a low-pass filter before its inversion or as a high-pass filter after its inversion. If we consider the two-dimensional case, the frequency response of the filter is as follows

$$G(\tau, \nu) = 1 - \exp(-\omega_0(\tau^2 + \nu^2)), \quad (2.19)$$

where ω_0 is the spatial frequency. The convolution kernel in the case of a Gaussian filter is as follows

$$g(x, y) = \delta(x, y) - \frac{\pi}{\omega_0^2} \exp(-\frac{\pi^2}{\omega_0^2}(x^2 + y^2)). \quad (2.20)$$

To find the regularization matrix of the Gaussian high-pass filter, it is necessary to express the filtered values of the conductivity distribution $\hat{\sigma}$, which are considered as constant values at the centers of the elements x_i, y_i of the search image

$$\hat{\sigma}(x_i, y_i) = g(x, y) * \sigma(x, y)|_{x=x_i, y=y_i}. \quad (2.21)$$

The convolution can then be further expanded as follows

$$\hat{\sigma}_i = \int g(x_i - x, y_i - y) \sigma(x, y) dx dy. \quad (2.22)$$

Because a constant conductivity value is considered on each element, the convolution can be modified to

$$\hat{\sigma}_i = \sum_j \sigma_j \int_{E_j} g(x_i - x, y_i - y) dx dy, \quad (2.23)$$

from where the shape of the regularization matrix for the filtered conductivity $\hat{\sigma} = L\sigma$

$$L_{ij} = \int_{E_j} g(x_i - x, y_i - y) dx dy. \quad (2.24)$$

2.1.7 Total variation regularization

The total variation functional (TV) captures all oscillations of the function under study on its domain. When used for regularization, it suppresses these oscillations. An important feature, however, is that it is not restricted to continuous functions, and thus can be used to smooth non-smooth transitions in the image. For continuous functions, the TV functional [34] is of the following form

$$TV(f) = \int_{\Omega} |\nabla f|, \quad (2.25)$$

while for non-differentiable functions [35] the functional is of the form

$$TV(f) = \sup_{v \in \nu} \int_{\Omega} f \operatorname{div} \mathbf{v}, \quad (2.26)$$

where ν is the space of continuously differentiable vector functions passing to zero on the boundary of the domain and for which $\|\mathbf{V}\|_{\Omega} \leq 1$. The deployment of the TV functional in the inversion is prevented by the fact that the functional is non-differentiable. This problem can be well overcome by deploying the Monte Carlo Markov Chain (MCMC) method [36].

2.1.8 Sensitivity matrix calculation

By sensitivity matrix is meant the Jacobian and thus the matrix of partial derivatives of the vector function, also mentioned above as the linearized forward operator. Thus, the sensitivity matrix converts the change in conductivity to a change in voltage across the electrodes for a particular set of current excitations.

$$J = \begin{pmatrix} \partial V(I_1^d)/\partial \gamma_1 & \cdots & \partial V(I_1^d)/\partial \gamma_i \\ \vdots & \ddots & \vdots \\ \partial V(I_j^d)/\partial \gamma_1 & \cdots & \partial V(I_j^d)/\partial \gamma_i \end{pmatrix}, \quad (2.27)$$

where $\partial V(I_n^d)/\partial \gamma_i$ is the sensitivity of the boundary voltage j dependent on the particular excitation current pattern d to the change in conductivity i . Thus, the dimension of the matrix i corresponds to the number

of conductivity elements, and the dimension of j corresponds to the number of measured voltages. The individual rows show the contributions of the voltage changes at a particular electrode from each conductivity element. A straightforward way of calculating the Jacobian is thus possible by repeatedly solving the forward problem with a perturbation on each conductivity element for each current excitation and then superposing these contributions. However, this solution is very computationally demanding.

In this study, the adjoint method [37] is used, which is based on the law of conservation of energy. The elements of the Jacobian are as follows

$$\frac{\partial V_i^{d,m}}{\partial \gamma_i} = - \int_{\Omega_i} \nabla u(\mathbf{I}^d) \nabla u(\mathbf{I}^m) dV, \quad (2.28)$$

where $u(\mathbf{I}^d)$ is the voltage due to the d -th excitation current pattern, $u(\mathbf{I}^m)$ is the voltage due to the conductivity perturbation, and Ω_i is the conductivity element in the domain under consideration. The main advantage of the method is that it does not need to calculate the forward problem for each conductivity element and for each excitation separately. It is sufficient to compute only the corresponding gradients for each node of the network and for each excitation pattern.

2.2 Forward problem

2.2.1 Forward problem formulation

The derivation of the forward problem, including electrode modeling (boundary conditions), is well described, e.g., in the [38] edition. From Maxwell's equations, the potential in the following derivation of the Laplace equation is approximated quasi-statically, which is justified typically up to frequencies of 50 kHz. The starting point is Kirchhoff's first law, the law of current, which is based on the conservative nature of the electric field

$$\nabla \cdot \mathbf{J} = 0 \text{ for area } \Omega, \quad (2.29)$$

where \mathbf{J} is the current density vector. This, therefore, establishes the assumption that there is no spontaneously occurring charge. Then, from Ohm's law, the relation between the electric field strength vector \mathbf{E} and the current density \mathbf{J}

$$\mathbf{J} = \sigma \mathbf{E}, \quad (2.30)$$

where σ is the electrical conductivity. Thanks to the quasi-static approximation of the electric potential, it is then possible to express the electric field strength \mathbf{E} as its gradient

$$\mathbf{E} = -\nabla V, \quad (2.31)$$

where V is the electric field potential. By successive substitution of the relations 2.29, 2.30 and 2.31 we obtain the well-known Laplace equation

$$\nabla \cdot \sigma \nabla V = 0 \text{ for area } \Omega, \quad (2.32)$$

where Ω is the area to be investigated. The boundary conditions for solving this equation depend on the method (configuration) of the EIT system used. The essential general boundary condition is again based on the conservative nature of the field, which implies that there is only a tangential component of the current at the edges of the $\partial\Omega$ investigated region, and thus the normal component is zero. Hence the consistency condition

$$\int_{\partial\Omega} \mathbf{j} = 0, \text{ kde } \mathbf{j} = -\mathbf{J} \cdot \hat{\mathbf{n}} = \sigma \nabla V \cdot \hat{\mathbf{n}} = \sigma \frac{\partial V}{\partial \hat{\mathbf{n}}} \text{ for area } \partial\Omega. \quad (2.33)$$

As was suggested in introduction, the common practice in tomographic measurement is to apply a current of known magnitude to the electrodes according to the stimulation pattern and then measure the voltage according to the measurement pattern. Based on the knowledge of the magnitude of the injected current, a Neumann boundary condition can then be added. Based on the electrode model used, a Dirichlet boundary condition can then be added by specifying the applied voltage. In the following, only the basic variant with the Neumann boundary condition will be considered. Other boundary conditions are included through the electrode model. The most commonly used model is the „Complete Electrode Model” (CEM), which provides for the boundary conditions the impedance of the electrodes, their short-circuit effect and the voltage-currents at the edges of the measured body.

$$U_l = \phi + z_l \sigma \frac{\partial \Phi}{\partial \mathbf{n}} \quad (2.34)$$

$$I_l = \int_{E_l} \sigma \frac{\partial \Phi}{\partial \mathbf{n}} d\mathbf{S} \quad (2.35)$$

$$\sigma \frac{\partial \Phi}{\partial \mathbf{n}} = 0 \quad (2.36)$$

$$\sum_{i=1}^L U_i = \sum_{i=1}^L I_i = 0 \quad (2.37)$$

Here U_l is the voltage at the l -th electrode, Φ is the scalar potential at the edges of the body, z_l is the contact impedance of the l -th electrode, and σ is the conductivity distribution of the body. Furthermore, I_l is the current through the l -th electrode. The relation 2.36 holds outside the electrode region and says that the current density outside the electrodes is zero. The relation 2.37 then respects the law of conservation of charge.

2.2.2 Formulation of the solution using the finite element method

The finite element method (FEM) is used to solve general cases of partial differential equations where the geometry of the problem does not allow the use of analytical solutions. The FEM is used in ERT problems due to its ability to model almost any geometry and also to apply various boundary conditions. The geometry is divided into a finite number of elements that form a finite element mesh. In the one-dimensional problem, an element is a line segment or curve; in the two-dimensional problem, it is a triangle or linear parabolic triangle; and in the three-dimensional problem, it is generally polyhedrons. Thus, the geometry is made up of non-overlapping elements that are connected by nodes. The geometry is followed by the modeling of the partial differential equation (PDE). The potential of the Laplace equation is approximated at the nodes of the network where the shape functions of the elements meet. Thus, the interpolation function is given by the sum of the shape functions at each node and is zero outside the node. The simplest shape function is one that is unitary at the node under investigation and zero outside it. An example of a shape function for the two-dimensional case is as follows

$$N_1^{(e)} = \frac{1}{2S_\Delta} [(x_2y_3 - x_3y_2) + (y_2 - y_3)x + (x_3 - x_2)y], \quad (2.38)$$

where S_Δ is the area of the triangular element. The remaining shape functions can be obtained by cyclically swapping the indices 1-2-3-1. From these shape functions of the nodes of the element, the approximation function of the node

$$N_j = \sum_{P_j} N_j^{(e)}, \quad (2.39)$$

where P_j is the number of elements with common node j . Such an approximation function then forms a unit height cone with a vertex at node j and edges connecting nodes adjacent to node j . The total approximation function 2.40 is then given by the sum of the approximation functions of the individual nodes.

$$\Phi_a = \sum_{j=1}^{NU} \Phi_j N_j(x, y) \quad (2.40)$$

Firstly, the approximation functions are not differentiable, and also the potential is only approximated, which creates some errors. Therefore, the equality of the Laplace equation 2.32 cannot be satisfied directly. This problem can be solved in several ways. In tomography, the most common method is the weighted residue method, or the Galerkin method, which introduces a so-called weak formulation of the equation

$$\int_{\Omega} v \nabla \cdot (\sigma \nabla \phi) dV = 0 \text{ pro oblast } \Omega, \quad (2.41)$$

where v is the test function, and in the case of the Galerkin method, it is the same as the approximation function. By using the vector identity $\nabla \cdot v \sigma \nabla \phi = \sigma \nabla \phi \cdot \nabla v + v \nabla \cdot \sigma \nabla \phi$, the equation 2.41 can be rewritten in the following form

$$\int_{\Omega} \nabla \cdot v \sigma \nabla \phi dV - \int_{\Omega} \sigma \nabla \phi \cdot \nabla v dV = 0. \quad (2.42)$$

Further, with the help of the Gauss-Ostrogradsky theorem (divergence theorem), the following relation can be obtained

$$\int_{\Omega} \nabla \cdot v \sigma \nabla \phi dV = \int_{\Omega} v \sigma \nabla \phi \cdot \mathbf{n} dS. \quad (2.43)$$

Substituting the relation 2.43 into 2.42 we obtain the following equation, which can be further restricted to the unified set of electrodes $\Gamma = \cup_l E_l$, where E_l is the l -th electrode. This is due to the zero current density outside the electrodes.

$$\int_{\Omega} \sigma \nabla \phi \cdot \nabla v dV = \int_{\partial\Omega} \sigma \nabla \phi \cdot \mathbf{n} v dS = \int_{\Gamma} \sigma \nabla \phi \cdot \mathbf{n} v dS \quad (2.44)$$

The relation 2.44 is, therefore, for a given set of test functions that are identical to the approximation functions, a weaker formulation of the equation 2.32 for the case of the boundary condition where we know the current density at the electrodes. In order to include the contact impedance of the electrodes, the boundary condition 2.34 is modified as follows under the assumption

$$\sigma \nabla \phi \cdot \mathbf{n} = \frac{1}{z_l} (U_l - \phi). \quad (2.45)$$

The weaker formulation 2.44 can then be rewritten as follows

$$\int_{\Omega} \sigma \nabla \phi \cdot \nabla v dV = \sum_{l=1}^L \int_{E_l} \frac{1}{z_l} (U_l - \phi) v dS. \quad (2.46)$$

Before substituting the approximated potential into the equation 2.46, let us recall again that the test function is the same as the overall approximation function. Therefore, $v = \sum_{i=0}^N v_i w$ holds. Subsequently, by substituting the approximated potential and the test function, we obtain for each i

$$\sum_{j=1}^N \left\{ \int_{\Omega} \sigma \nabla w_i \cdot \nabla w_j dV \right\} \phi_j + \sum_{l=1}^L \left\{ \int_{E_l} \frac{1}{z_l} w_i w_j dS \right\} \phi_j - \sum_{l=1}^L \left\{ \int_{E_l} \frac{1}{z_l} w_i dS \right\} V_l = 0. \quad (2.47)$$

The overall current is constant in this type of problem and can be rewritten as follows, assuming constant electrode contact impedance

$$I_l = \int_{E_l} \frac{1}{z_l} (V_l - \phi) dS = \int_{E_l} \frac{1}{z_l} V_l - \sum_i^N \left\{ \int_{E_l} \frac{1}{z_l} w_i dS \right\} \phi_i = \frac{1}{z_l} |E_l| V_l - \frac{1}{z_l} \sum_i^N \left\{ \int_{E_l} \frac{1}{z_l} w_i dS \right\} \phi_i, \quad (2.48)$$

where $|E_l|$ is the area (or length in the two-dimensional case) of the l -th electrode.

The equations described above can be rewritten in matrix form into a finite element system of equations, which looks as follows

$$\begin{bmatrix} \mathbf{A}_M + \mathbf{A}_Z & \mathbf{A}_W \\ \mathbf{A}_W^T & \mathbf{A}_D \end{bmatrix} \begin{bmatrix} \phi \\ \mathbf{V} \end{bmatrix} = \begin{bmatrix} 0 \\ \mathbf{I} \end{bmatrix}, \quad (2.49)$$

where \mathbf{A}_M is an $N \times N$ symmetric matrix (where N is the number of mesh nodes and K is the number of domain elements). This is the simplest case of approximation, where there is a piecewise constant (PWC) value of the approximated function on each element. It is also the matrix form corresponding to the solution of the 2.32 equation without the mentioned boundary conditions.

$$\mathbf{A}_{M,ij} = \int_{\Omega} \sigma \nabla w_i \cdot \nabla w_j dV = \sum_{k=1}^K \sigma_k \int_{\Omega} \nabla w_i \cdot \nabla w_j dV \quad (2.50)$$

The matrices \mathbf{A}_Z , \mathbf{A}_W and \mathbf{A}_D already include the boundary conditions of the CEM model and look as follows

$$\mathbf{A}_{Z,ij} = \sum_{l=1}^L \int_{E_l} \frac{1}{z_l} w_i w_j dS, \quad (2.51)$$

$$\mathbf{A}_{W,ij} = \frac{-1}{z_l} \int_{E_i} w_i dS, \quad (2.52)$$

$$\mathbf{A}_D = \mathbf{diag} \left(\frac{|E_l|}{z_l} \right), \quad (2.53)$$

$$\mathbf{U} = \mathbf{A}_W \mathbf{V}. \quad (2.54)$$

As is clear from the equation 2.50, the conductivity here is simply multiplied by the system of equations. Thus, the matrix of the system of equations depends only on the geometry of the mesh, not on the conductivity distribution. For this reason, it is advantageous to prepare the system matrix in advance when generating the mesh. By solving the system of equations 2.49, we obtain the values of the potentials ϕ at the nodes inside the domain and the values of the potentials \mathbf{V} at the nodes at the edge of the domain. The voltages at the individual electrodes can then be calculated simply by the relation 2.54.

Chapter 3

The aim of the work

The objectives of this work are based on the aforementioned motivation to investigate more rigorously the detection capability of ERT in the case of carbon CFRP composites for the common and most critical defect of BVID impact and crack. The next objective is also to propose procedures for possible improvement of the detectability of ERT based on the gained experience. In the following, the three main objectives are briefly and clearly stated, preceded by a necessary objective, which was to build suitable instrumentation and to learn the necessary procedures to prepare experimental coupons.

3.1 Development of instrumentation and realization of experimental coupons

An essential goal is the preparation of suitable instrumentation enabling automatic data acquisition according to a preset excitation and measurement pattern. It is also necessary to ensure the production of experimental coupons with sufficiently reliable and robust electrodes.

3.2 An evaluation of the detection capabilities of the ERT in the area of the BVID impact

The main goal of this study is to perform a detailed experimental study of the detectability of ERT in the case of BVID impact using commonly used smoothing priors. Thus, the problem is to find a threshold for the size of the impact from which the impact can be reliably detected.

3.3 Improvement of the detection capabilities of the ERT in case of crack damage

Another aim of this study is to compare the crack detection capabilities of CFRP in the case of a smoothing prior and in the case of a Gaussian anisotropic filter. The aim is to show the benefits of anisotropic smoothing and to suggest how to apply them in practice.

3.4 Optimization of electrode position and shape towards a BVID impact detection

The final objective of the study is to optimize the position and shape of the electrodes in the design phase of the ERT system. The goal is to find a way to design the layout of the electrodes qualitatively and to show the effects on the quality of BVID position detection.

Chapter 4

Hardware implementation of ERT in the field of CFRP composites

As discussed in the introduction and further elaborated in the theoretical part, electrical resistivity tomography is based on the measurement of the boundary voltages during the stimulation of an electric current. To successfully solve the inverse problem, it is necessary to perform a certain number of suitably combined boundary voltage measurements concerning current stimulation, domain geometry, measurement parameters, etc. These combinations are described by the stimulation and measurement pattern. The most common patterns with a single current source, either measuring or stimulation, are adjacent, opposite, or a combination of these.

4.1 Stimulation and measurement pattern

As can be seen from the names of the patterns, the opposite pattern considers combinations of opposite pairs of electrodes, while the adjacent pattern considers pairs of adjacent electrodes. When choosing a measurement pattern, it is important to pay attention to an essential detail of the measurement pattern, which is the measurement at the stimulating electrodes. For reconstruction, it is generally not recommended to measure the stimulating electrodes since the possible disturbance of the contact resistance of the electrodes, which is not known in advance, will significantly disturb the consistency between the numerical model and reality. For this reason, it is advisable to choose the measurement pattern to include measurements at the electrodes for the purpose of estimating the electrode contact resistance while excluding these measurements from the dataset for reconstruction purposes.

The choice of the type of stimulation/measurement pattern depends on the specific application. For example, the stimulation pattern should be chosen to penetrate as much of the monitored domain as possible. However, if the electrical conductivity distribution in a particular region is insufficiently conductive, the choice of this pattern could naturally be a disadvantage. Another criterion for the choice of a pattern, whether measuring or excitation, is the distribution of electrical conductivity compared to the capabilities of the excitation current source or the resolution of the voltmeter used. The choice of excitation/measurement pattern can then be used to optimize [39] e.g., the data acquisition time in combination with the reconstruction quality, which can be essential in the case of on-line monitoring. In the case of choosing opposite patterns in a symmetric domain, one should beware of undesirable mirroring effects [40].

As an example of a stimulation and measurement pattern, Figure 4.1 shows a combination of an opposite stimulation pattern with an adjacent measurement pattern, which is further used in the key experimental section.

The choice of the number of electrodes is one of the most critical parameters of the whole design. It is closely related to the choice of the number of mesh elements of the numerical model used for image reconstruction (see the solution of the inverse problem 2.1). Thus, the number of electrodes and the number of mesh elements strongly influence the resulting determination of the inverse problem, and both parameters should be chosen with the highest care. The number of mesh elements N must not exceed the number of independent measurements. Otherwise, the inverse problem will be underdetermined. Since the image reconstruction matrix can be shown to be Hermitian [41], its number of degrees of freedom is equal to $L(L - 1)/2$, where L is the number of electrodes. The relationship between the number of mesh elements

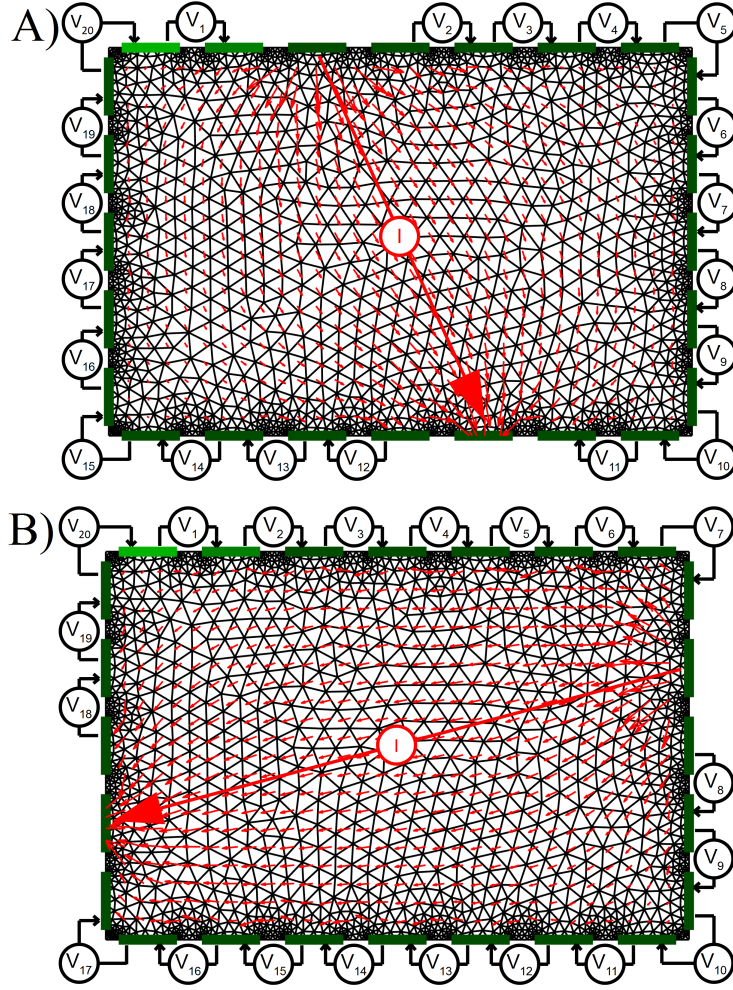


Figure 4.1: Example of the opposite stimulation pattern and the adjacent measurement pattern without measurements at the excitation electrodes, which was used in the experiments in this work for tomographic measurements: A) demonstration of stimulation at electrodes 3 and 15 and B) stimulation at electrodes 9 and 21.

N and the number of electrodes L is then as follows

$$N \leq \frac{L(L-1)}{2}. \quad (4.1)$$

4.2 Hardware implementation of current stimulation and boundary voltage measurement

The measurement and stimulation requirements described above can be implemented in several ways. An obvious description can be found in the book [42]. The fundamental division of systems can be made in terms of the number of current sources for stimulation of the monitored object, i.e., single source and multi-source; see the block diagram in Figure 4.2.

A single-source tomography system (see Figure 4.2 A) excites the observed object with a single dual current source, which typically has a harmonic waveform. The advantage of a dual current source is half the value of the harmonic voltage when measuring the boundary voltages with a differential amplifier or twice the stimulation current while maintaining the value of the harmonic voltage. The multiplexer can then be used to deliver a stimulation current to any two electrodes according to the stimulation pattern. Active shielding of the conductors is also an essential part of the circuits, especially if the capacitive component of the impedance is also monitored. Active shielding avoids parasitic capacitances that otherwise occur between conductors and drift significantly due to the handling of the conductors. The essential part of

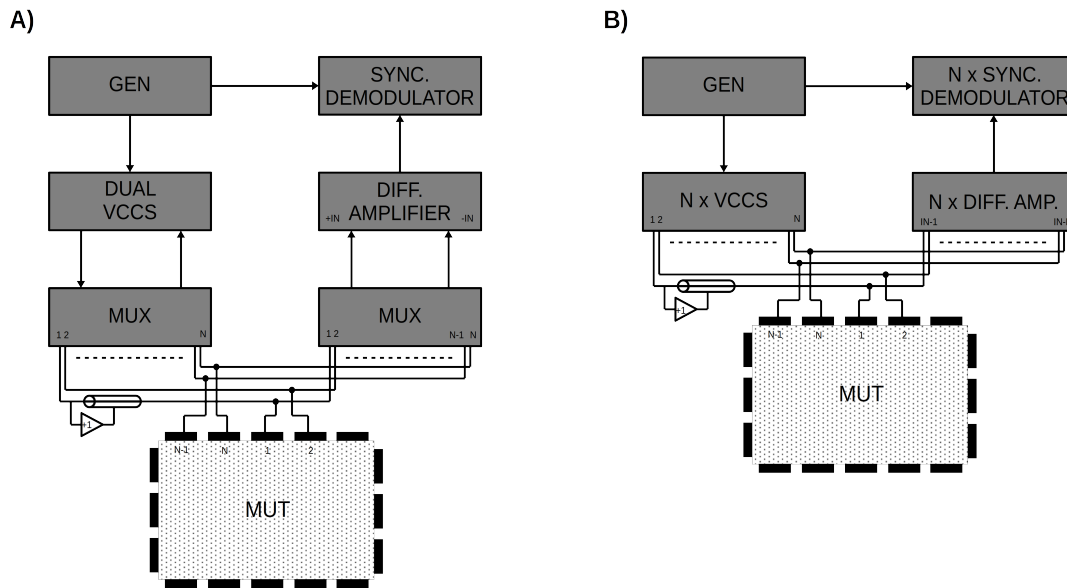


Figure 4.2: Block diagram of ERT system with single current source (A) compared to multi-current variant (B). The current source here is a voltage-to-current converter with a dual current source (VCCS).

the system is the differential amplifier, which reduces the need for an extensive dynamic range compared to other options referenced to a common ground. The last essential part of the measurement chain is the synchronous demodulator (vector voltmeter) [43]. This is both essential for decomposing the measured voltage into real and imaginary components in the case of EIT, but also advantageous in this case due to its ability to extract a useful harmonic signal with an amplitude several orders of magnitude lower than the ambient noise. In the case of ERT, where only the real component is measured, it is convenient to use synchronous demodulation to shift the useful signal to the least cluttered part of the spectrum, thus avoiding any parasitic effects arising, especially in the electrode region.

The multi-source tomography system (see Figure 4.2 B) contains one current source for one pair of electrodes. The excitation pattern is then defined by the current patterns of all electrode pairs, with the resulting current of all sources being zero. The disadvantage is the necessity to always measure at the excitation electrodes, which complicates the possible elimination of degraded data due to a possibly damaged electrode with increased contact resistance. Naturally, the advantage is speed since it is not necessary to sequentially measure a large number of combinations given by the stimulation and measurement pattern of a single source system.

4.2.1 Experimental facilities

This dissertation was initially based on a modular ERT system assembled from parts of commercially available stand-alone devices combined with elements that were developed in-house. At a later stage of the dissertation, the background was enriched with a professional PXI system, which by its configuration merged all the elements of the ERT system into a single desktop instrument.

Modular ERT system

The modular ERT system was further used for the experimental part of the issues in Chapter 5 and 6. For the purpose of ERT experiments, the measurement chain (see diagram in Figure 4.3) was designed to meet the basic requirements of ERT with respect to the available resources at the initial stage of the research.

The most critical element of the chain was the multiplexer, which in a configuration suitable for ERT is less readily available among conventional instruments, as it is usually part of an even larger unit. For this reason, a custom solution was developed. The essential feature of the multiplexer for ERT with a single current source is the need to switch four channels to any electrode of the N electrodes. Since, in the initial phase, it is necessary to work exclusively with coupons of simpler geometries, it was decided that a total

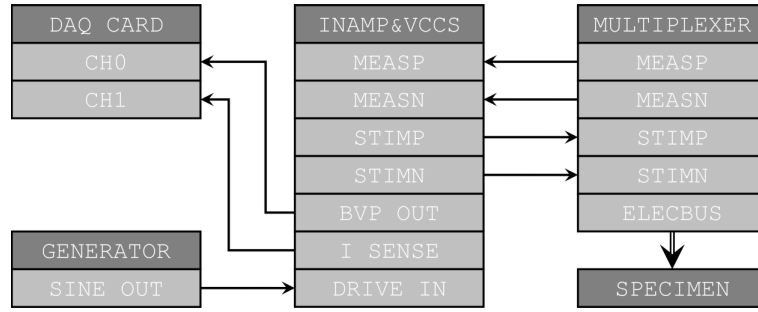


Figure 4.3: Block diagram of modular ERT system. The harmonic voltage (SINE OUT) is converted to stimulation current (STIMP, STIMN) by a voltage-to-current converter with a dual current source (VCCS) and then connected to any electrode by a multiplexer. The resulting boundary voltage (MEASP, MEASN) is amplified and converted to a non-differential signal (BVP OUT) by an instrumented amplifier (INAMP). The progress of the stimulation current is monitored by a voltage output (I SENSE). The boundary voltage and stimulation current are digitized (DAQ CARD) and then processed by synchronous demodulation.

of 32 channels should cover most of the needs. Thus, a 4:32 multiplexer was developed. The measurement channels were also equipped with active shielding.

Considering the above requirements, a 16-channel ADG1406 monolithic iCMOS multiplexer was chosen as the primary element. The block diagram of the multiplexer is shown in Figure 4.4 (a), where multiplexer blocks (2) and (3) are for current stimulation, blocks (4) and (5) are for measurement, blocks (6) and (7) are for active shielding and block (8) is the ground switch. The requirement for active shielding capability has complicated the design somewhat. In addition to the eight ADG1406 multiplexers to provide 4x32 channel connectivity, an additional four multiplexers had to be connected to meet the active shielding requirement. In addition, two additional 16-channel ADG1438 switching matrices were needed to shield unused channels. The multiplexers and switches are controlled by a PIC18F45K22 microcontroller (1), which also provides serial communication and a logic output for channel indication. All functionality is handled via serial communication except active/passive shielding, which is controlled by hardware jumpers. The analog circuits are powered by an LT3032 ± 15 V low-noise voltage regulator. The number of components used resulted in a complex and spacious PCB.

However, it was necessary to minimize the length of the channel paths to minimize the stray capacitance. The final design resulted in a parallel PCB connection, as shown in 4.4 (b), where on the top are the screw terminals for connecting the electrodes, and on the left are the BNC connectors for the measurement circuits and the current source connection. On the right are the connectors for the power supply and communication. Verification of the primary parameters was an essential part of the development. Frequency bandwidth, isolation capability, and crosstalk between channels were measured over a frequency range of up to 200 kHz. The unit gain error ($U_{IN}/U_{OUT} - 1$) was approximately -6%. As far as the isolation capability of the measurement channels is concerned, it was more or less unaffected (compared to the parameters specified by the manufacturer) by the circuit design. In the case of the stimulation channels, however, there was a 20 dB drop. The crosstalk between the measurement channels ranged from 110 dB at low frequencies to 50 dB at 100 kHz. More can be found in the publication [44].

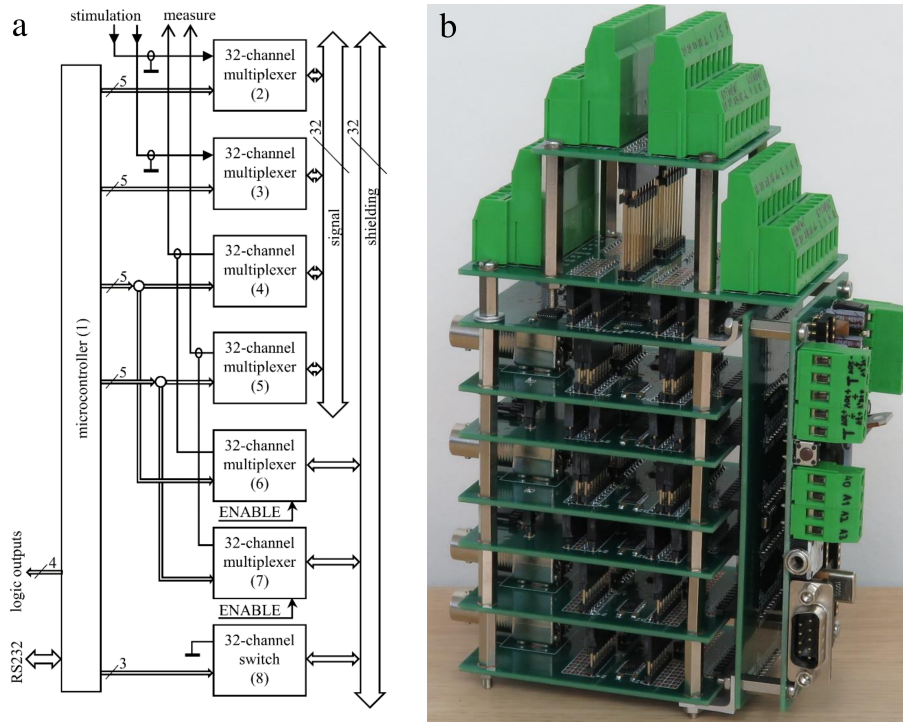


Figure 4.4: Block diagram of the 4x32 multiplexer with active/passive shieldings (a); Photo of the developed 4x32 multiplexer (b).

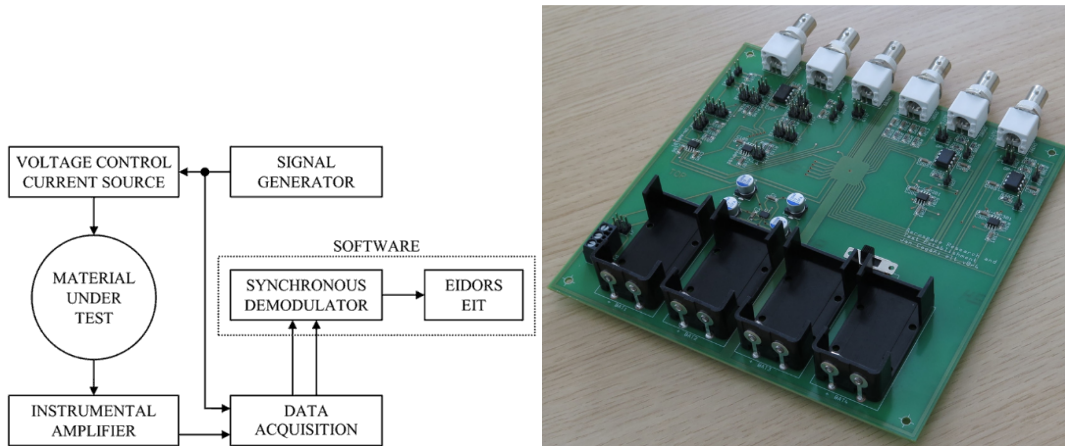


Figure 4.5: Block diagram of stimulation, measurement, and post-processing circuitry (left). Implementation of circuits for excitation and boundary voltage amplification (right).

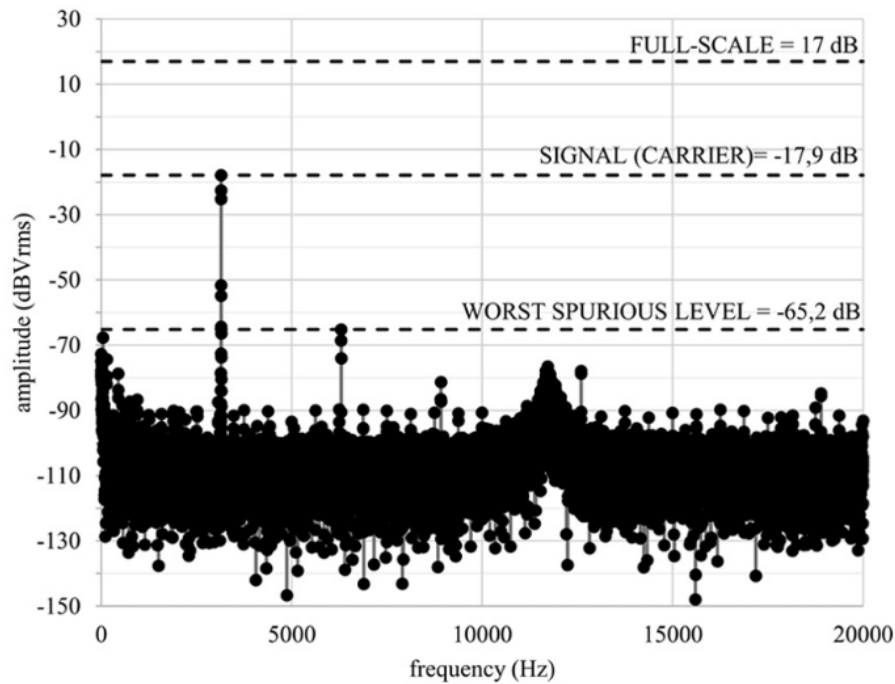


Figure 4.6: Frequency spectrum of the measured signal on an intact specimen.

Another essential part of the modular ERT system was the differential amplifier represented by the instrumentation amplifier. The choice of the AD8421B instrumentation amplifier was made mainly with respect to the input impedance, which was sought to be maximized with respect to the boundary condition 2.37. At the same time, a circuit was chosen that allows for excitation and active shielding of each input separately in accordance with the multiplexer proposed above. The differential amplifier module also included a voltage-controlled precision current source. A typical AD620 instrumentation amplifier circuit was chosen as the current source. The current converter was excited by a harmonic signal from a stand-alone generator. The excitation current was sensed in this circuit and, together with the output of the differential amplifier, was then simultaneously digitized and processed by synchronous demodulation. In addition to the input impedance of the measuring amplifier, attention was also paid to the dynamic range or the useful signal-to-noise ratio in combination with the used DAQ card (DAQ Orion, manufacturer Dewetron). From the exemplary measurements on the composite coupon, the spectrum was evaluated (see Figure 4.6), which showed that in the worst case the dynamic range was 47 dBc. Despite these reasonably good noise characteristics, synchronous demodulation was used. Synchronous demodulation was used in this case mainly to ensure sufficient signal-to-noise separation. The block diagram is included in Figure 4.5 on the left, while the implementation is on the right. More details on the configuration of this part can be found in the author's paper [45].

ERT system based on PXI

Furthermore, the PXI-based ERT system was mainly used in the electrode optimization problem in Chapter 7. For the purpose of the ERT system (see photography in Figure 4.7), a combination of PXI multimeter modules, switch matrix, and the current source was used:

- PXIe-4081: 7½-Digit, ±1,000 V, Onboard 1.8 MS/s Isolated Digitizer, PXI Digital Multimeter,
- PXIe-2529: 128-Crosspoint Relay Matrix,
- PXIe-4322: 16-Bit, 8-Channel, 250 kS/s Ch-Ch Isolated PXI Analog Output Module.

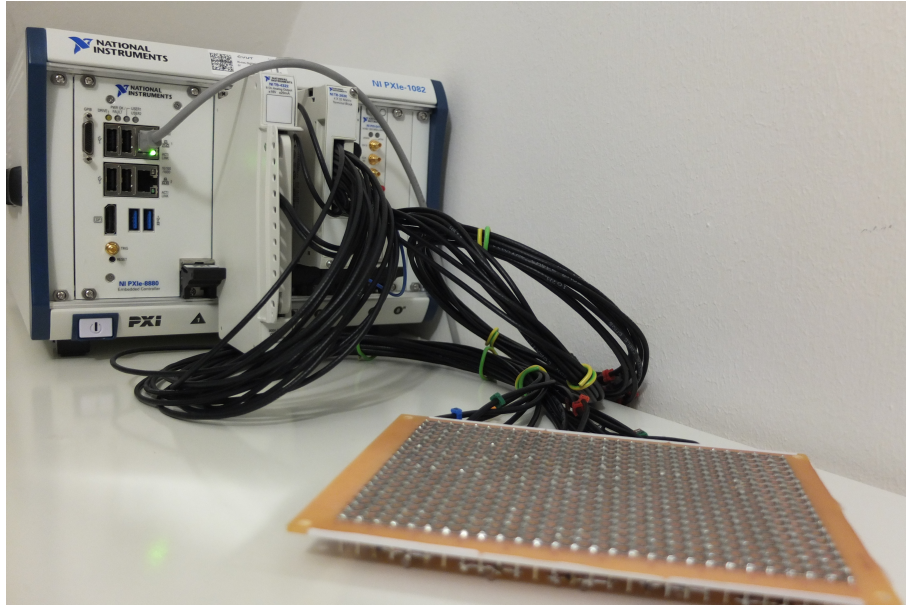


Figure 4.7: PXI measurement system in wiring to ERT measurement together with resistor network coupon.

The essential parameters in the case of boundary voltage measurements for tomography purposes are the parameters of the digital multimeter, namely the noise, the ability to suppress the common mode voltage, and the bias current given by the input impedance of the multimeter. The accuracy of the PXIe-4081 multimeter can be demonstrated by comparing these three basic parameters in Table 4.1 with the modular system described above in Chapter 4.2.1. Furthermore, in the case of the PXI system, one can generally rely on industry standards for professional system performance. Due to the high accuracy and reliability of the PXIe-4081 digital multimeter, no additional post-processing, such as synchronous demodulation, was implemented in the case of the modular system. The proposed instrumentation is therefore based on DC stimulation and boundary voltage measurements.

Table 4.1: Comparison of key parameters of the PXI system and the modular system.

Parameter	PXI system	Modular system
NOISE	0.1 mVrms	0.55 mVrms
CMRR	140 dB	126 dB
BIAS	30pA	2nA

Part of the preparation of the software part of the PXI system was the creation of a data acquisition program. The program was developed in the LabView graphical development environment, which is the standard in this field alongside other National Instruments tools. The basic requirements for a tomographic data acquisition program are:

- possibility to set any excitation and measurement pattern for 32 channels (either by import from text file or preset most used variants),
- possibility to set arbitrary measurement and excitation parameters,
- continuous monitoring of measured boundary voltages (graph and table),
- possibility to store the measured data and all measurement parameters in JSON and CSV files.

The implementation of the program is based on a combination of a simple state machine and a number of callback functions linked to graphical program controls. The main program window consists of two parts.

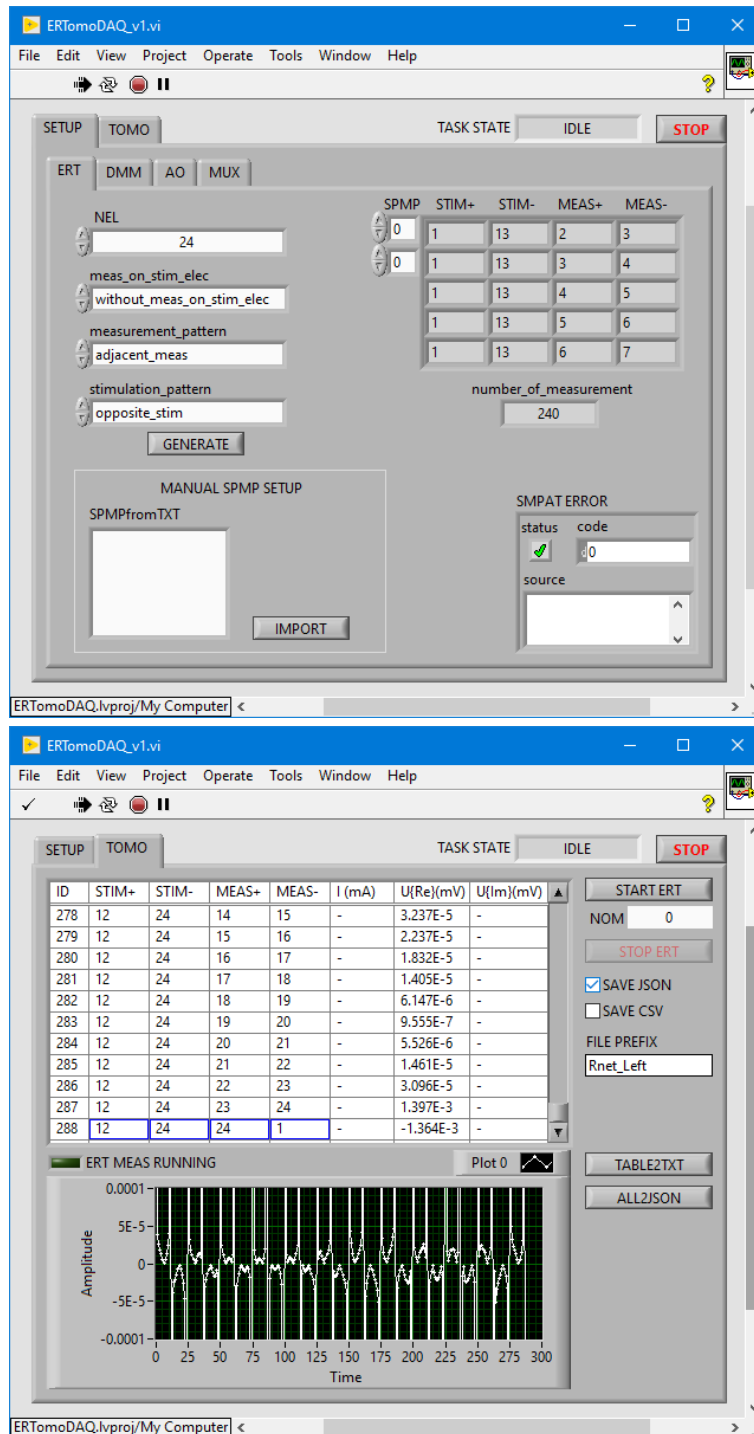


Figure 4.8: Example of a program for a PXI system for measuring/exciting boundary voltages. The *SETUP* section with hardware settings (top) and the *TOMO* section for boundary voltage measurement (bottom).

The *SETUP* section combines all the hardware settings for measuring boundary voltages and current excitation (see Figure 4.8 above). In addition to setting parameters for the digital multimeter (subsection *DMM*), analog output (subsection *AO*) with current source and multiplexer (subsection *MUX*), any measurement and excitation pattern can be set in subsection *ERT*. The measurement and stimulation pattern can be generated based on the requirement to measure or not to measure at the stimulating electrodes, the number of electrodes, and the adjacent or opposite pattern.

The *TOMO* section, see Figure 4.8 below, then allows to start the measurement of edge voltages based on the selected measurement and stimulation pattern and other measurement parameters selected above. Once the measurement starts, individual measurements are taken according to the measurement and stimulation

pattern. The table, together with the graph, is successively updated with the measured data. After the measurements are completed, the measured data, together with all settings, are saved in the corresponding files.

4.2.2 Electrode Implementation

Although the implementation of electrodes may seem like an obvious and simple step, in the case of CFRP composite, it is one of the most crucial steps in the installation of the entire ERT setup.

The basic requirements for each electrode are:

- compliance with the assumed geometry and position,
- minimal contact resistance,
- uniform distribution of contact resistance in the electrode area.

In order to achieve the above steps (especially the last two), it is necessary to ensure a sufficiently conductive connection between the conductor and all the carbon fibers in the electrode area. The main obstacles are the non-conductive matrix of the composite and the surface treatment of the fibers, which is always present for the purpose of better cohesion between the carbon fiber core and the matrix. Conductive bonding can be achieved in several ways. For example, Tsung-Chin Hou and collective [46], as well as Loyola and collective [21], have used silver conductive paste and copper tape to create a conductive bond with carbon nanoparticle composite. A similar approach, enriched by sandblasting the composite, has been carried out by Baltopoulos and collective [23] as well as Wang and Chung, [47]. Another approach, more or less suitable for laboratory purposes, is the use of a conducting polymer in combination again with a silver conductive paste, also carried out by Baltopoulos et al. [14]. The most robust seems to be the realization of electrodes by electroplating [48, 49, 46], where the matrix and the outer part of the fibers are removed using sulfuric acid applied to the sandblasted surface, followed by the electrodeposition of copper electrodes. The same procedure was successfully replicated in the work of Haingartner and colleagues in [50]. One of the more recent works in this area was carried out by Almuhammadi and colleagues, who used laser radiation to clean the carbon fibers in [51], achieving five times lower contact resistance compared to sandblasting alone. In addition, considerable repeatability of production was achieved with this method. In this work, the electrode preparation method of Todoroki [49] was used and verified.

NOTE: With respect to the stacking sequence of the composite, it is necessary (both in design and fabrication) to consider the size of the fabric strands so that the intended electrode size covers a sufficient number of strands to account for the overall anisotropic properties of the electrical conductivity, especially when trying to neglect them.

The specific steps taken in the manufacture of electrodes in this work are as follows:

- Sanding of the laminate surface using sandpaper, grit 200;
- Uncovering the fibres (sizing and a thin layer of polymer matrix removing) with the use of a solution (12 g of 96% H₂SO₄ + 3 g of 30% H₂O₂/80 °C) for a period of 1 min;
- Rinsing with water and cleaning by brush;
- Rinsing with distilled water;
- Washing with acetone;
- Drying on the filter paper;
- Masking of the areas outside the electrodes with 'M-coat A';
- multiple coatings with conductive painting with silver pieces, including "coating" of electrode conductors.

The principle diagram of the electrode cross-section is shown in Figure 4.9 together with a photograph of the cleaned and uncleaned fibers. In the early development of this work, increased attention was paid to the electrodes, particularly as a result of initial failures in image reconstruction, where it was apparent that it was not possible to reconstruct the electrical conductivity with satisfactory quality on a large proportion of the experimental coupons without having to omit some measurements that contained a defective electrode.

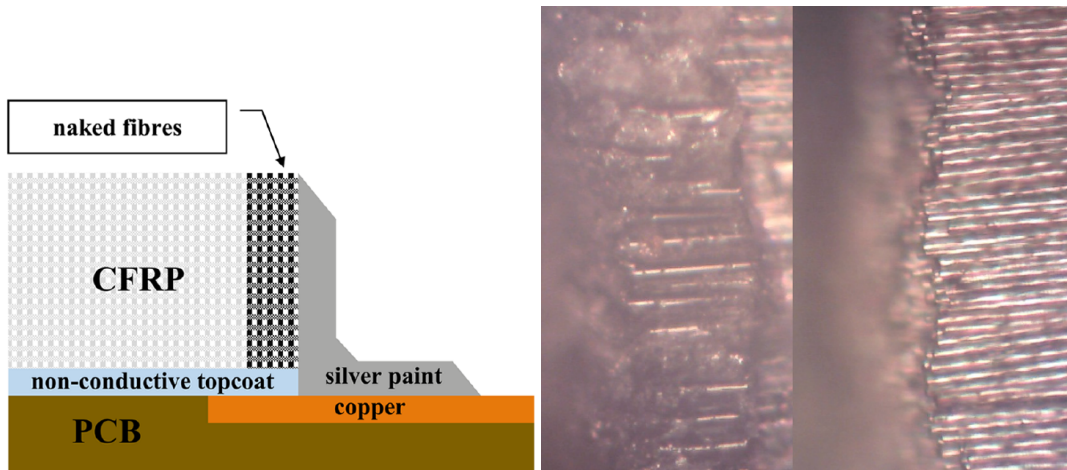


Figure 4.9: Principal diagram of the cut between CFRP and conductor (left). Photo of the edge of CFRP coupon without cleaning (left part) and after chemical cleaning (right part), magnified 400x.

In order to verify the electrode manufacturing process, the variations of the contact resistances of the electrode pairs for excitation with opposite excitation pattern were monitored on the coupon without and with chemical cleaning. The verification was performed on a circular composite coupon 4.10 (left) with a diameter of 100 mm and nineteen electrodes with a length of 12.52 mm, where the electrical resistance was measured and the deviations of 4.10 (right) were calculated as the difference of the lowest resistance value measured. As can be seen in the graph, chemical cleaning of the electrodes is a crucial step in their fabrication.

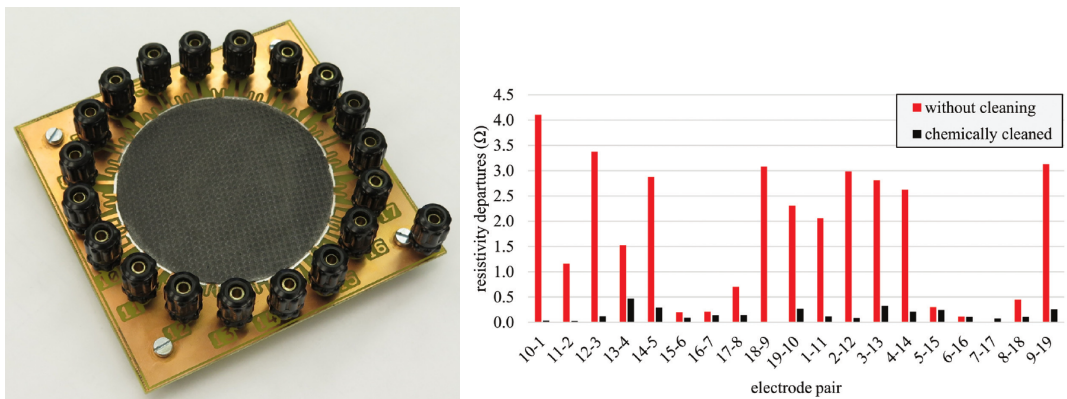


Figure 4.10: Circular composite coupon (left) for verification of electrode manufacturing together with measured contact resistance variations (right).

Chapter 5

Detection capability of ERT in case of BVID

5.1 Barely visible impacts

As hinted in the introduction, considerable attention has been paid to the detection of barely visible impact. Barely visible impacts in normal operation are the result of inadvertently dropping a tool during servicing, hitting an ice hail, or colliding with birds. Such impacts cause delamination along with a combination of other defects such as fiber disruption or matrix cracking, which are hidden under the surface and thus very difficult to see [52]. Many papers have already addressed the BVID issue. For example, the work of [52, 53] has focused on detailed (layer-by-layer) finite element mechanical analysis. Since the standard NDI method for BVID detection and quantification is ultrasonic inspection, a number of papers have focused on the detection capabilities of this method. Interestingly, non-contact methods such as laser shearography [54] or thermography [55] are also part of the NDT methods.

Although ERT has a low spatial resolution, it is pretty sensitive to small changes in conductivity, making it a suitable method for detecting point inhomogeneities. Since BVID has the character of point inhomogeneity, the investigation of the ability of ERT to detect BVID is the mainstay of the entire work. Thus, the key question is whether ERT has sufficient sensitivity to detect BVID and what is the nature of this sensitivity. To this end, an experimental evaluation of the ERT ability to detect barely visible impacts has been performed using probabilistic detection curves (POD) that demonstrate the amplitude response of the method along with its repeatability. At the same time, considerable attention was paid to the position error, which also allowed to evaluate the ability of the ERT to locate BVIDs. The experimental evaluation of the BVID detection capability described below was published in the paper [56].

5.1.1 BVID structure

Impact damage is a result of the contact force effect evoked by an impactor, which leads to material deformation. The primary consequence is multiple delaminations resulting from interlaminar shear failures. The extent and location of the delaminations are functions of the material properties of the laminate and impact energy. Another consequence is the tensile failure of fibers. In most cases of BVID, the delamination dominates in comparison with the failure of fibers. The matrix's ability to stabilize the fibers in compression degrades significantly in the presence of delamination. Because compression is one of the most critical loading modes, BVID is one of the most insidious damage types.

Most of the impact damages presented in this work were evaluated as barely visible due to poor visibility of flaws which was quantitatively proven by measuring the dents depths in Table 5.1 below. The measured relationship between the impact energy through the different laminate stacking sequences is shown for illustrative purposes.

5.2 ERT setting for BVID detection

The main feature of the setup described below is the assumption that it is possible to neglect the anisotropy of electrical conductivity, which is typical for CFRP composites, especially in the case of simple point inhomogeneity reconstruction. This assumption can be supported by the findings of Schueler [57], who

Table 5.1: The dent depths in relation to impact energy and stacking sequence.

E(J)	QUASI-ISOTROPIC(mm)	ORTHOTROPIC(mm)	ASYMMETRIC(mm)
4.8	0.06±0.02	0.13±0.01	0.12±0.01
6.5	0.10±0.02	0.32±0.05	0.21±0.01
8.0	0.17±0.04	0.40±0.08	0.28±0.03

estimates that the ERT is usable to up to an anisotropy degree of 100 (ratio of resistance ρ_{90}/ρ_0). Moreover, the detailed analysis of conductivity image reconstruction with anisotropic finite elements performed by Lionheart and Paridis [58, 59] proved a lack of improvement in the uniqueness of the image reconstruction, namely in the Jacobian conditioning. Because of these assumptions, it was possible to use the Matlab toolkit EIDORS [37] as is.

5.2.1 Forward and inverse model

The used forward model is based on the finite element method (FEM), where a piecewise linear approximation of the potential is used, and the conductivity is assumed to be isotropic based on the above assumptions. Thus, the anisotropy due to the stacking sequence of the composite is neglected. The electrodes are modeled by a complete electrode model (CEM) within the numerical model.

The geometry of the considered coupon was modeled by a triangular mesh in the two-dimensional model (3458 elements and 1920 nodes) and tetrahedrons in the case of the three-dimensional model (16801 elements and 5508 nodes).

The first step of the whole activity was the verification of the model. The absolute values of the boundary voltages simulated by the 3D model were fit by varying the homogeneous conductivity to the measured boundary voltages of a selected sample with a quasi-isotropic stacking sequence that minimally violates the assumption for neglecting conductivity anisotropy. The conductivity found was 8600 S/m. To verify the function of the 2D model, its boundary voltages simulated based on this conductivity were also compared. The comparison also included the measured boundary voltages of the other stacking sequences of the selected coupons. An example of this comparison is shown in Figure 5.1.

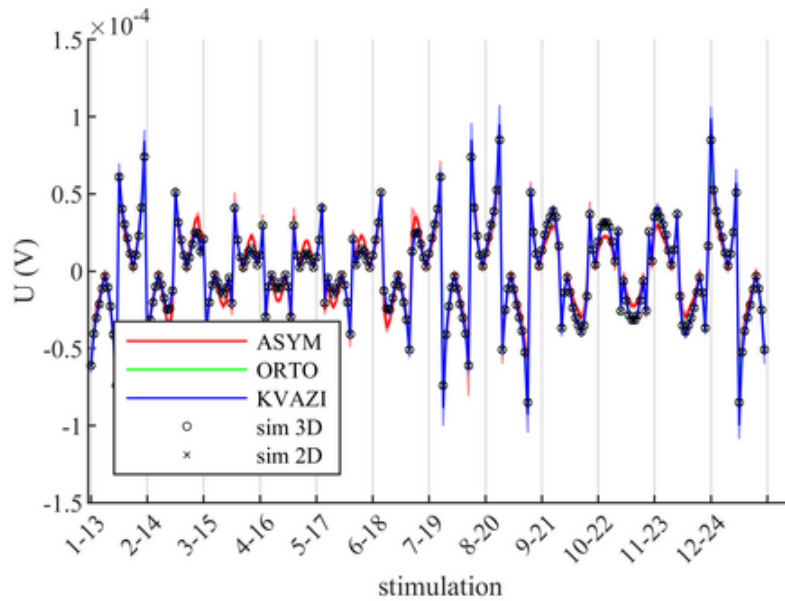


Figure 5.1: Measured boundary voltage potentials of typical specimens of the asymmetric (ASYM), orthotropic (ORTO), and quasi-isotropic (KVAZI) stacking sequence. Absolute values of potentials are averaged from 4 measurements during current stimulation of the 4 mA. Measured values are compared with simulations on the 2D model (sim 2D) and 3D model (sim 3D).

Differential image reconstruction was performed with the MAP algorithm with several priors in order to assess the possible influence on the resulting reconstruction.

The following damage-detection capability assessment is performed with the following priors:

- Total variation (TV) (see Chapter 2.1.7),
- Tikhonov (TIK) (see Chapter 2.1.3),
- Newton’s one-step error reconstructor (NOSER) (see Chapter 2.1.4),
- Laplace 2nd-order high-pass filter (LHP) (see Chapter 2.1.5),
- Gaussian high-pass filter (GHP) (see Chapter 2.1.6).

Image reconstruction is performed as a differential reconstruction. Each image reconstruction is related to the baseline measurement, which is, in this work, the measurement of the specimens without damage (e.g., in Figure 5.1). The reason for difference imaging is the higher stability of the inverse problem in the presence of electrode position errors and shape inaccuracy [60], or in the case of unknown contact impedance of the electrodes [61]. An example of the differential (non-normalized) boundary voltages is in Figure 5.2 (A), which corresponds to the response on the impact of different values of the impact energy for the specimen with a quasi-isotropic laminate stacking sequence. This example is explanatory, among other things, because of relations between the responses of the differential amplitudes on the impact in the barely visible range and the measurement noise, whose standard deviations are depicted by the shaded areas (Figure 5.2 (B), the first stimulation pattern).

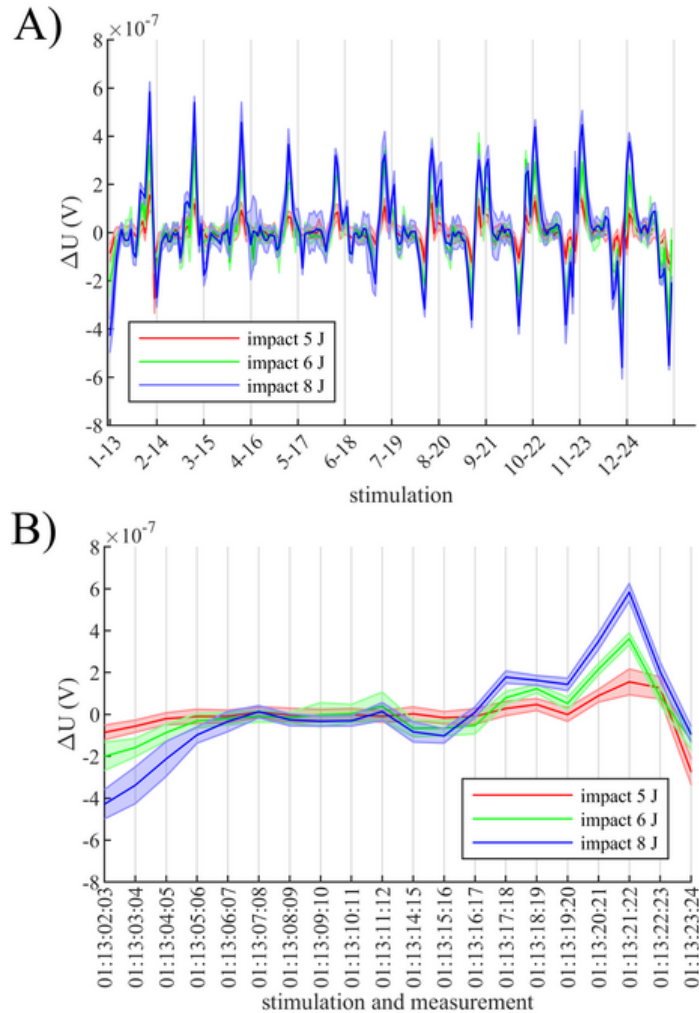


Figure 5.2: Average differential (non-normalized) boundary voltages with standard deviations of specimens with quasi-isotropic stacking sequence damaged by BVID: A) the whole dataset; B) example of stimulation on electrodes 1 and 13.

5.3 Implementation of the experiment

The specimens were produced by the vacuum infusion manufacturing technique (light resin transfer molding). The specimens were cured for 18 h under a vacuum of -80 kPa at room temperature. Post-curing without vacuum at 85°C lasted 18 h. Rectangular specimens with sizes of 100×150 mm were cut from a panel with a size of 650×500 mm. Epoxy resin ARALDIT LY5052 (with ARADUR 5052 hardener) and carbon fabric for aerospace applications ECC style 450-5 (plain weave, 200 g/m²) [62] were used to prepare a composite panel. The dimension corresponds to the requirements of ASTM D7136 for measuring the damage resistance of a fiber-reinforced polymer matrix composite to a drop-weight impact event. The three most common laminate stacking sequences were selected for the experiment: quasi-isotropic (QUASI), orthotropic (ORTHO), and asymmetric (ASYM). The thickness of each panel was 3 mm, and the laminate stacking sequence was 12 warp/weft layers. In the quasi-isotropic case, the orientation was $[0/90^\circ, \pm 45^\circ]_6$. In the orthotropic case, the orientation was $[0/90^\circ]_{12}$, whereas in the asymmetric case, the orientation was $[0/90^\circ]_{12}$ with fiber ratio of 25/75% (75% along the longitudinal direction of the specimen).

Electrodes were implemented by silver paste according to previously published procedure [45]. The electrode dimensions of 15×3 mm were selected according to the best practice, especially given that the CFRP fabric was woven from 2-mm-wide strands. The electrodes were oriented perpendicularly with respect to the fibers' orientation. Dozens of specimens were produced, whereas four specimens from each laminate stacking sequence were used for each impact energy measurement (3 stacking sequences × 3 impact energies × 4 repeated measurements = 36 specimens in total) and six specimens for thru-hole measurements (3 stacking sequences × 6 repeated measurements = 18 specimens in total). A portion of the set of CFRP specimens can be seen in Figure 5.3.

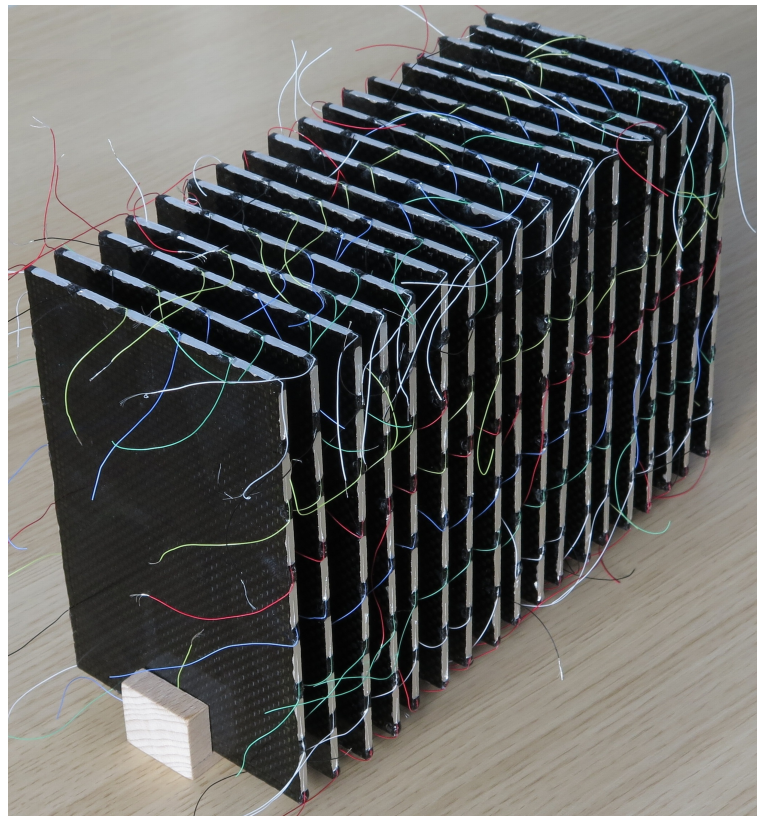


Figure 5.3: A portion of the set of CFRP specimens of dimensions 150×100 mm with 24 electrodes.

BVID was implemented by a hand-operated spring impactor for the implementation of artificial impacts. The impactor had a hemisphere striker tip with a diameter of 12.7 mm. An impact energy range, which causes BVID in the case of the laminate-stacking sequences used, was up to 10 J. Due to the possibilities of the spring impactor, the following energy values were selected: 4.8 J, 6.5 J, and 8 J. The mean values with standard deviations of the dent depths in relation to impact energy are listed in Table 5.1.

Impacts were applied to the specimen, which was connected to the above-mentioned measurement system. The specimen was placed on an impact support fixture, which was also equipped by soldering

terminals for the electrode connections. With regard to the overall conditions and dimensions, the position error of the applied impact was ± 2 mm. This is why the specimens with thru-hole defects, whose position error of application is significantly smaller, were measured. An example of the specimen with BVID impact in Figure 5.4.

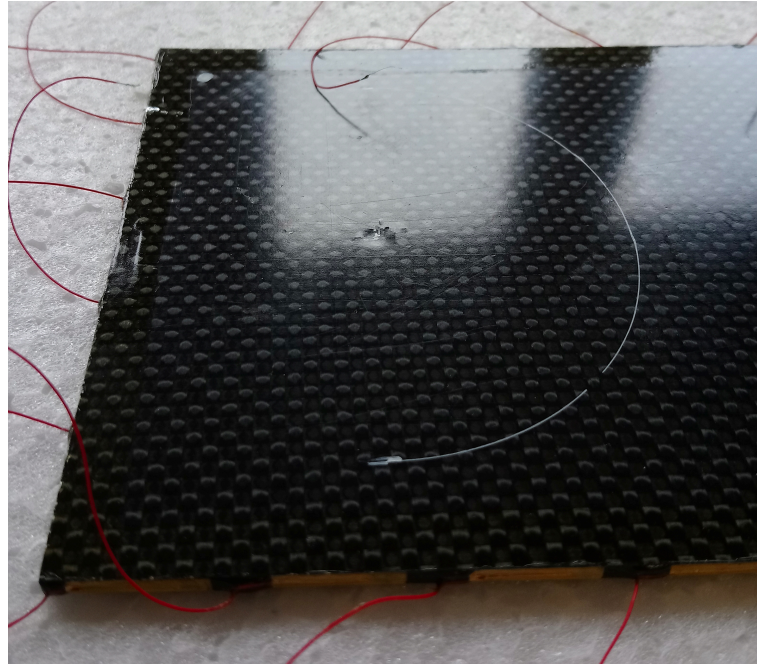


Figure 5.4: An example of BVID positioned at coordinates X: -37.5 mm, Y: 0 mm with respect to specimen center.

Ultrasonic inspection of all test specimens was performed in the immersion tank using the 20-MHz PA probe and UT flaw detector Omiscan MX2. Amplitude C-scans were realized, and the delamination area was determined based on the amplitude decrease of the back-wall echo. A standard method of 6 dB back-wall echo drop [63] was utilized stating the threshold of impact border at half of its base height. Each pixel below the threshold was counted into the impacted area, which was considered as an area of delamination.

5.4 BVID detection capability assessment

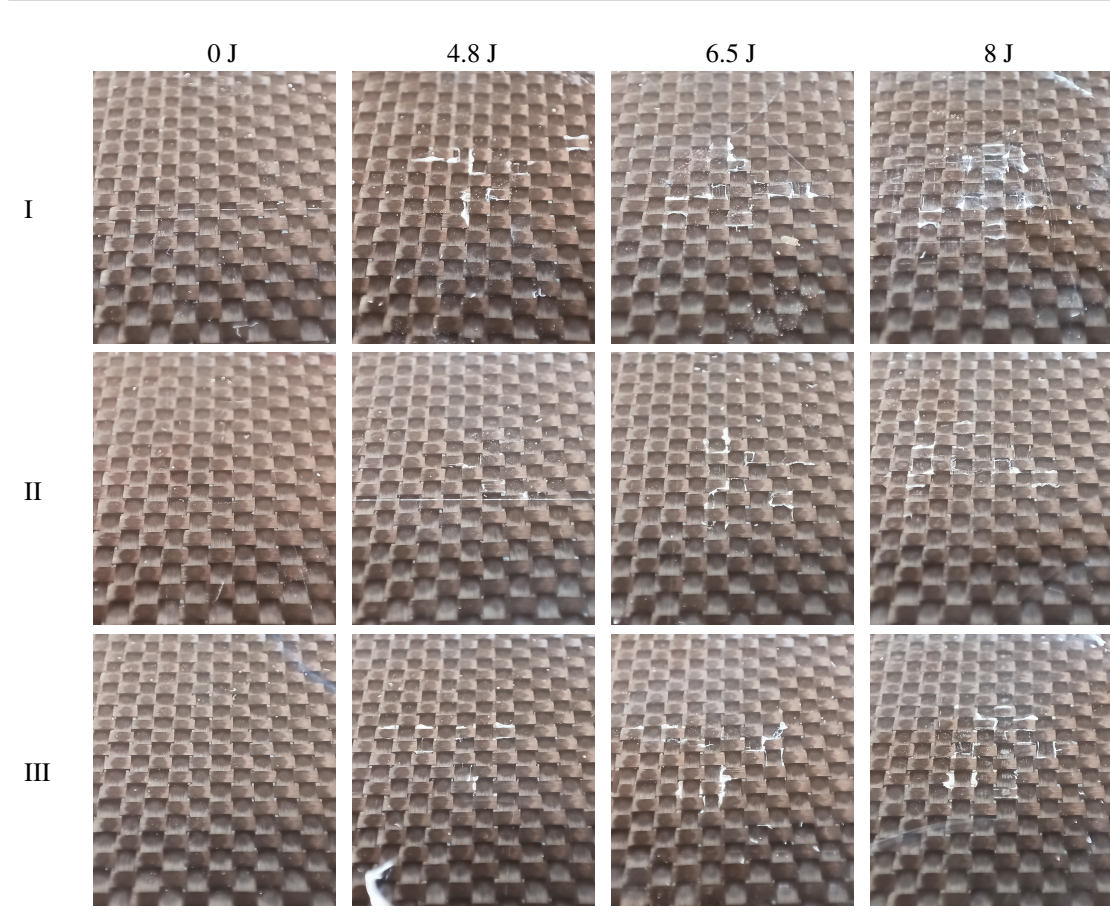
An elementary task of the SHM system is detecting the location and size of the damage. For this reason, the position error and amplitude response of the image COG is subjected to a more detailed assessment. The low resolution of the ERT is accepted as a fundamental feature of this method and attention is focused only on the amplitude response and position error, without noticing other figures of merit related to a resolution or generally an image quality.

5.4.1 Position error

The position error was only studied on specimens with drilled thru-holes. This is because there is negligible nominal position error of applied drilling compared to that of applied BVID impacts. To justify this simplification, Table 5.3 provides a comparison of the amplitude responses of drilled thru-holes and BVID. The overlapping of the amplitude responses of both damage types shows their similarity. The position error was determined as the distance from the nominal position of applied drilling to the COG (amplitude extreme in an ideal case). The COG was evaluated from a truncated image, where 10 mm was removed from each side of the conductivity image. Such image truncation leads to improvement of the COG evaluation due to the ablation of conductivity departures in the electrode's vicinity. Truncation was also performed in the case of amplitude assessment in the following section.

The position errors are presented by histograms in Figure 5.5, where values are sorted from stacking sequence or image prior point of view. The most populated intervals are from 1 to 3 mm in both cases of the division, which represents an error up to 2% of the longer dimension of the specimen. In the case of

Table 5.2: BVID photos in detail at three observed energies (columns) compared to the flaw-free state (0 J) in three different cases (rows).



comparison by the stacking sequences, the worst results exhibit the asymmetric stacking sequence due to its scatter. In the case of the asymmetric stacking sequence, the conductivity image was more deformed along the longitudinal direction due to the greatest deviation of specimen conductivity from the isotropic assumption. In the case of comparison by the image priors, the worst results exhibit the total variation and TIK priors. Values of the reconstructed amplitudes of the drilled thru-holes were also used to determine the noise analysis in the following utilization of the probability of detection (POD), where a noise distribution function helped to define a_{dec} .

5.4.2 Amplitude response

The damage size was observed by a quantitative signal represented by the conductivity change (image amplitude response) in the COG. The relationship between the amplitude changes and the area of delamination was assessed statistically by the POD. The POD curve provides a quantitative and graphical assessment of the probability of detection and target size. Software mh1823 POD[64] was used for the statistical assessment. The software offers tools for statistical modeling of physical dimensions of a target a (area of delamination in this study) and a measured response to the target size \hat{a} (conductivity change in the COG of the ERT image in this study). The relationship between the amplitude changes and area delamination was modeled by a *loglog* link function because $\log \hat{a}$ versus $\log a$ exhibited the best linear dependence. The regression model used has the form $\hat{y} = \hat{\beta}_0 + \hat{\beta}_1 x$, where \hat{y} is an estimated response, $\hat{\beta}_0$ is an estimated offset, and $\hat{\beta}_1$ is an estimated slope. A useful outcome of the following comparison via this regression method is the estimated standard deviation $\hat{\tau}$. According to the best practice, for reasonable precision in the estimates of the POD, the minimum number of measurements is 40 in the case of the quantitative response. Nevertheless, with respect to the available sources allocated for this study, only 11 measurements per stacking sequence were evaluated. For this reason, the resulting POD curves should be interpreted with caution. Nevertheless, for the purpose of comparison between individual stacking sequences and priors, this

Table 5.3: Comparison of amplitude responses of drilled THRU-HOLES and BVID. Amplitudes are sorted in ascending order. Damage extent is in mm in the case of drilled THRU-HOLES or mm² in the case of BVID.

DAMAGE TYPE	DAMAGE EXTENT	AMPLITUDE RESPONSE ($\times 10^{-3}$)
THRU-HOLE	0, 6	0, 10
THRU-HOLE	1, 0	0, 18
BVID	104	0, 24
THRU-HOLE	1, 4	0, 27
THRU-HOLE	1, 8	0, 40
BVID	141	0, 43
BVID	140	0, 50
THRU-HOLE	2, 2	0, 53
BVID	154	0, 56
THRU-HOLE	2, 5	0, 63
BVID	198	0, 77
THRU-HOLE	3, 0	0, 78
THRU-HOLE	3, 5	0, 91
BVID	186	1, 03
BVID	220	1, 04
BVID	178	1, 13
BVID	228	1, 17
BVID	218	1, 24
BVID	249	1, 39

number of measurements is sufficient. A part of the following overall comparison is the parameter $a_{90/95}$ specifying the target size, which can be detected with probability 90% with 95% confidence bound. For the purpose of POD evaluation, it was necessary to specify the decision threshold a_{dec} , which determines the amplitude level above which the amplitude is interpreted as damage. This threshold is normally specified by the requirements of the performed inspection. Nevertheless, for the purposes of this study, where the damage-detection capability is assessed, the decision threshold is set to the lowest possible value. In the cases where the noise was below the minimum value of the amplitude, the threshold was set to the same value as the minimum. In other cases, where the noise was above the minimum value, the decision threshold was set such that the false calls were up to 5%. The noise was described by the Gaussian probability density. The noise amplitude was obtained from measurements of specimens damaged by a thru-hole of diameter 2.5 mm, insofar as they exhibited the best match with the amplitude levels of the specimens damaged by BVID. The whole noise distribution was biased tightly above the zero value. There was some effort to use amplitudes from those reconstructed from measurements without damage. Nevertheless, these amplitudes were disproportionately higher than those reconstructed from measurements with damage, which is probably because the inverse problem was ill-posed.

The overall comparisons of specimens damaged by BVID for quasi-isotropic and orthotropic stacking sequences are stated in Table 5.4 and Table 5.5, respectively. The comparison specimens with asymmetric stacking sequences were not compared because they lacked evident linear dependence of $\log \hat{a}$ versus $\log a$.

Table 5.4: Estimates of regression parameters and the POD for the quasi-isotropic laminate stacking sequence damaged by the BVID.

PRIOR	$\hat{\beta}_0$	$\hat{\beta}_1$	$\hat{\tau}$	a_{dec}	$a_{90/95}$
TV (Total variation)	-20.49	2.32	0.23	-8.80	185.8
NOS (Newton's one-step error reconstructor)	-18.38	2.18	0.17	-7.96	143.0
LHP (Laplace 2nd-order high-pass filter)	-18.57	2.23	0.18	-7.96	141.7
GHP (Gaussian high-pass filter)	-18.65	2.21	0.18	-8.11	141.1
TIK (Tikhonov)	-18.96	2.19	0.17	-8.52	142.6

The first evident conclusion regarding the amplitude response in the estimated slope $\hat{\beta}_1$, indicates that the conductivity amplitude is more responsive in the quasi-isotropic case than in the orthotropic case. It can be seen that the used prior does not affect the slope. Differences in the response between stacking sequences

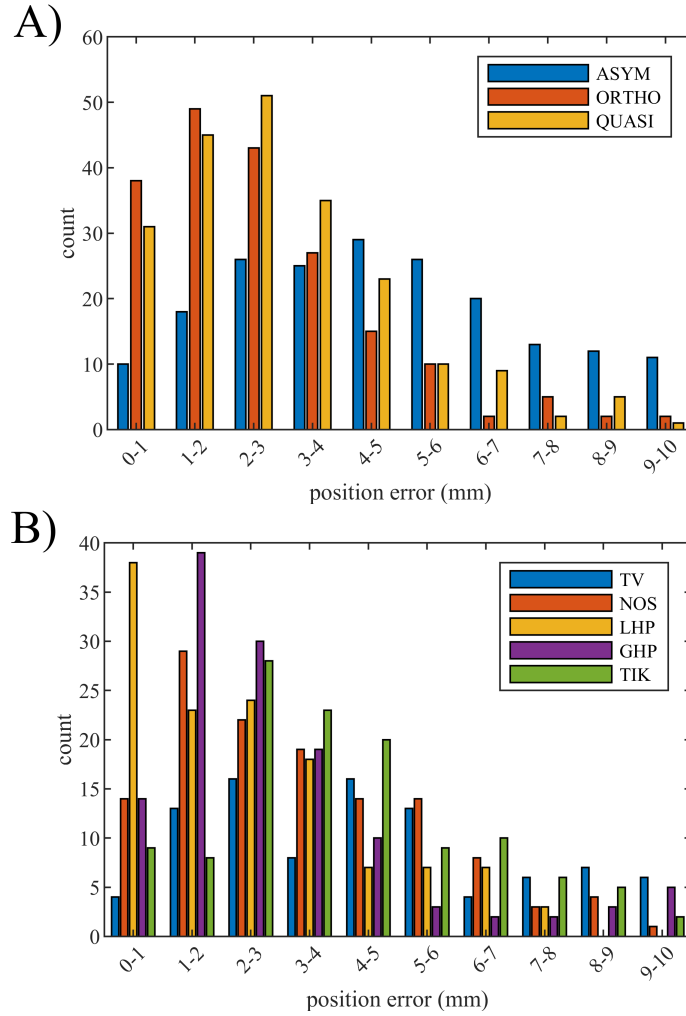


Figure 5.5: Histograms of the position errors of the specimens with drilled thru-holes categorized by A) the stacking sequence or B) the image priors.

are caused by neglect of anisotropy in the case of the orthotropic stacking sequence, which can be intuitively explained by the missing conductive paths in the diagonal direction, resulting in missing contributions to the useful signal. Neglect of anisotropy is also the reason for the higher standard deviation $\hat{\tau}$ together with higher target area $a_{90/95}$, which can be detected. Estimates of the regression parameters can also be compared with the case of drilled thru-holes, which are summarized in Table 5.6. In the case of drilled thru-holes, the target size $a_{90/95}$ was the diameter of the thru-hole in mm. The slope comparison, in that case, did not exhibit higher responsiveness for quasi-isotropic stacking sequence as in the case of impacted specimens. This may indicate that delamination, which dominates in the case of impacted specimens, causes higher responsiveness, specifically in terms of the slope, than missing fibers in the case of drilled thru-holes. On the other hand, missing fibers cause a significant increase in the offset $\hat{\beta}_1$. It is worth noting that the TV prior exhibited worse repeatability and stability than other priors. Even in the case of thru-holes, the number of successful reconstructions with TV prior was reduced dramatically, so regressions were not performed correctly. Other smoothing priors yielded stable, repetitive, and similar results.

Table 5.5: Estimates of regression parameters and the POD for the orthotropic laminate stacking sequence damaged by the BVID.

PRIOR	$\hat{\beta}_0$	$\hat{\beta}_1$	$\hat{\tau}$	a_{dec}	$a_{90/95}$
TV (Total variation)	-16.07	1.56	0.31	-7.83	300.5
NOS (Newton's one-step error reconstructor)	-15.10	1.60	0.24	-7.53	152.6
LHP (Laplace 2nd-order high-pass filter)	-15.13	1.61	0.23	-7.52	156.7
GHP (Gaussian high-pass filter)	-15.22	1.61	0.24	-7.65	157.2
TIK (Tikhonov)	-15.21	1.52	0.26	-8.07	161.5

Table 5.6: Estimates of regression parameters and the POD for the quasi-isotropic and orthotropic laminate stacking sequences damaged by the drilled thru-hole.

PRIOR	QUASI-ISOTROPIC					ORTHOTROPIC				
	$\hat{\beta}_0$	$\hat{\beta}_1$	$\hat{\tau}$	a_{dec}	$a_{90/95}$	$\hat{\beta}_0$	$\hat{\beta}_1$	$\hat{\tau}$	a_{dec}	$a_{90/95}$
NOS	-8.54	1.34	0.16	-8.11	1.69	-8.90	1.46	0.12	-9.21	1.25
LHP	-8.49	1.35	0.17	-8.11	1.63	-8.84	1.47	0.13	-8.52	1.46
GHP	-8.62	1.32	0.17	-8.11	1.83	-8.97	1.44	0.12	-8.80	1.30
TIK	-9.10	1.31	0.16	-8.52	1.92	-9.47	1.46	0.12	-9.20	1.40

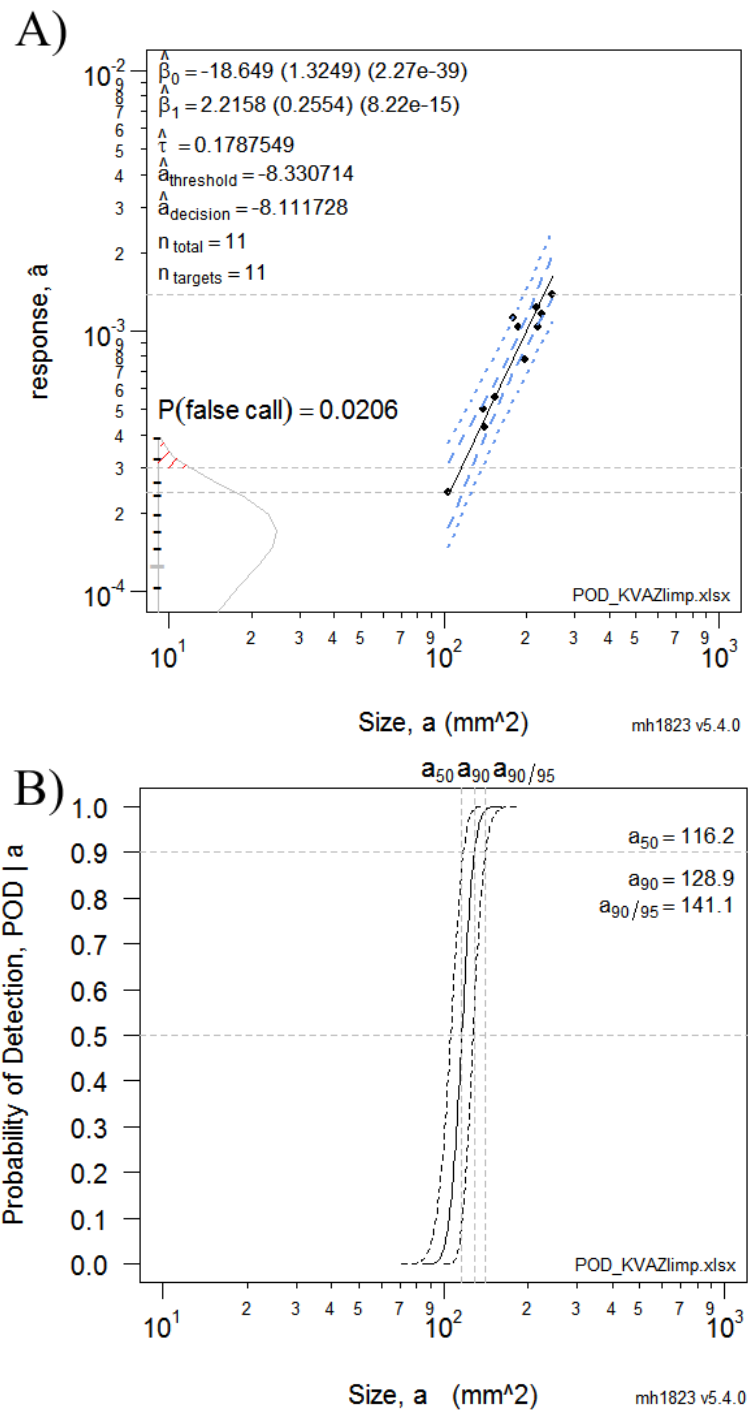


Figure 5.6: An example of the (A) statistical model and (B) relevant POD curve for quasi-isotropic laminate stacking sequence reconstructed with GHP prior.

Table 5.7: Overview of some typical image reconstructions across individual stacking sequences (QUASI-ISOTROPIC, ORTHOTROPIC, ASYMMETRIC) and image priors (TV - Total Variation, NOS - Newton's One-Step Error Reconstructor, LHP - Laplace 2nd order High Pass filter, GHP - Gaussian High Pass filter, TIK - Tikhonov) related to C-scan images and areas of delamination. Reconstructed images contain marks for the center of gravity (red circle) and the nominal position of the BVID (green cross).

	E(J) s(mm ²)	CSCAN	TV	NOS	LHP	GHP	TIK
QUASI-ISOTROPIC	4.8 141						
	6.5 196						
	8 218						
ORTHOTROPIC	4.8 136						
	6.5 235						
	8 307						
ASYMMETRIC	4.8 177						
	6.5 191						
	8 275						

Chapter 6

Crack detection capability of ERT

In the previous chapter, an examination of the detection capability of ERT in the case of BVID impact was performed. Barely visible impact damage results in most failure modes, which subsequently propagate as a result of the interaction of initiating damage as additional stresses are applied. One case of subsequent propagation can be crack propagation under certain circumstances. The real damage of the composite is not highly localized and depends on the stress type [65]. For tension, the damage starts with microcracking of the matrix in the majority of the material volume, and splitting of the fibers within a lamina occurs in the most stressed areas [66]. Then, the delaminations begin to grow when the microcracks merge together and develop toward the lamina interface [67]. Finally, fiber cracking occurs in the areas most weakened by the previous damage. Based on the stacking sequence, these three types of failure can occur in various ratios. For example, the delaminations can be prevalent or even non-existent before the fiber fracture occurs. Impact damage usually creates all three types of failure at once, with microcracking and delamination prevalence [68]. Therefore, in this part of the work, the focus will be on the reconstruction of the crack conductivity image, which will be crudely simulated by a cut in the CFRP specimen. The impact of the use of an anisotropic filter on the reconstruction of the cut as a simulated crack will be shown for the three most commonly used CFRP laminate compositions, as was the case in the investigation of the BVID impact detection capabilities in the previous chapter. In this case, the regularization matrix is always constructed on a case-by-case basis. For this purpose, a simple user interface was created in Matlab, allowing the input of the predicted crack direction. The investigation of the detection capabilities described below was published in *Structural Health Monitoring* [69].

6.1 Anisotropic Gaussian smoothing filter

The anisotropic Gaussian filter is an extension of the isotropic Gaussian filter (see section 2.1.6). The filter is applied in the context of image reconstruction using the MAP approach. Thanks to the introduced anisotropy, the degree of smoothing can be controlled in a certain desired direction and thus not perform "unwanted" blurring. The derivation of the regularization matrix was performed by Borsic [70] in his paper. The filter is also considered for the two-dimensional reconstruction case with spatial frequencies ω_u and ω_v . The surrogate regularization matrix \mathbf{L} that approximates the filter can be found by expressing the filtered conductance $\hat{\sigma}$ as a continuous function $\sigma(u, v)$ at the points (u_i, v_i) by the convolution $\hat{\sigma} = \sigma * g$, which leads to the equation

$$\hat{\sigma}(u_i, v_i) = \int_{-\infty}^{\infty} \sigma(u, v) g(u - u_i, v - v_i) dudv, \quad (6.1)$$

where $g(u - u_i, v - v_i)$ is the anisotropic Gaussian kernel given by

$$g(u - u_i, v - v_i) = \delta(u - u_i, v - v_i) + \frac{-\pi}{\omega_u \omega_v} \exp \left\{ -\pi^2 \left[\frac{(u - u_i)^2}{\omega_u^2} + \frac{(v - v_i)^2}{\omega_v^2} \right] \right\}. \quad (6.2)$$

Here the convolution kernel equation corresponds to an isotropic filter in the case $\omega = \omega_u = \omega_v$. In the case of a triangular network, where a particular element is denoted by L_j and its center u_j, v_j , the integral equation (6.1) for that element is as follows

$$I_{ij} = \int_{L_j} \sigma(u, v) g(u - u_i, v - v_i) dudv, \quad (6.3)$$

where $j = 1, \dots, n_x, i = 1, \dots, n_x$, and

$$\int_{L_j} \sigma(u, v) \delta(u_i, v_i) du dv = \begin{cases} \sigma(u_i, v_i), & i = j \\ 0, & j \neq i. \end{cases}$$

The values of I_{ij} from equation (6.3) are elements of the search matrix \mathbf{L} and are used to construct the covariance matrix $\mathbf{R} = (\mathbf{L} + \mathbf{L}^T)/2$ or $\mathbf{R} = \mathbf{L}^T \mathbf{L}$. The covariance matrix \mathbf{R} is symmetric and positively definite while converging to the unit matrix in the case $\omega_u \rightarrow +\infty, \omega_v \rightarrow +\infty$.

The practical implementation of the covariance matrix calculation needs to be done with a coordinate transformation. If a general anisotropic filter on each element of L_i will be considered

$$\tilde{g}(\tilde{u} - \tilde{u}_i, \tilde{v} - \tilde{v}_i) = \frac{-\pi}{\omega_{\tilde{u}} \omega_{\tilde{v}}} \exp \left\{ -\pi^2 \left[\frac{(\tilde{u} - \tilde{u}_i)^2}{\omega_{\tilde{u}}^2} + \frac{(\tilde{v} - \tilde{v}_i)^2}{\omega_{\tilde{v}}^2} \right] \right\}, \quad (6.4)$$

where \tilde{u} and \tilde{v} are the coordinates related to base \mathbf{t}, \mathbf{n} (see Figure 6.1 on the top). Components u, v are related to original base $\mathbf{e}_1, \mathbf{e}_2$. Base \mathbf{t}, \mathbf{n} has components $\mathbf{t} = (t_1, t_2), \mathbf{n} = (n_1, n_2)$. The valid transformation is

$$\begin{pmatrix} u \\ v \end{pmatrix} = \begin{pmatrix} t_1 & n_1 \\ t_2 & n_2 \end{pmatrix} \begin{pmatrix} \tilde{u} \\ \tilde{v} \end{pmatrix}.$$

Using such a transformation, the function (6.4) is transformed into coordinates u, v . We choose unit vector at each center u_i, v_i of cell $L_i, i = 1, \dots, n_x$. Normal vector $\mathbf{n} = (n_1, n_2)$ is a unit vector and perpendicular to vector \mathbf{t} . It is valid when $n_1 = -t_2, n_2 = t_1$. The resulting transformation can be written as

$$\begin{aligned} \tilde{u} - \tilde{u}_i &= t_1(u - u_i) + t_2(v - v_i) \\ \tilde{v} - \tilde{v}_i &= -t_2(u - u_i) + t_1(v - v_i). \end{aligned}$$

6.1.1 Experimental verification of crack detection filter

The anisotropic Gaussian filter described above has been subjected to experimental verification in this work. For the purpose of verifying the behavior of the filter on a real object, the same composite coupon as in Chapter 5 were used (see configuration 5.3). Furthermore, the applied flaw simulating the crack was made by milling a groove of 35 mm in length and 1 mm in width. Two grooves were successively placed in the middle of the diameter of the longer side of the specimen.

By choosing local parameters ω_u and ω_v and unit vector \mathbf{t} according to the a priori information about the searched cut, we can adjust the directivity of smoothing the filter at different places in the image, thereby improving the focus. In the below-described eligibility demonstration of the Gaussian anisotropic regularization for cut detection, parameters ω_u, ω_v , and \mathbf{t} were chosen by the user based on a known nominal position of the cut. The nominal position was convenient for demonstration purposes because it minimally violated the assumptions about the cut location.

The nominal position was convenient for demonstration purposes because it minimally violated the assumptions about the cut location. In Figure 6.1, the mesh of the used geometry with the depicted image reconstruction obtained by the Gaussian isotropic smoothing filter [33] is shown in the top figure. The nominal position of the cut is depicted by a red line. The bottom figure shows the area of the anisotropy selected by the user, for which the parameters are selected according to Table 6.1. It should be noted that the implementation of the aforementioned Gaussian anisotropic smoothing is based on the proportional changes of parameters ω_u and ω_v relative to an initial state.

Table 6.1: Values of the parameters of the Gaussian anisotropic smoothing filter.

parameter	anisotropic	isotropic
ω_u	0.9	1
ω_v	0.1	1
\mathbf{t}	$(\cos(\pi/4), \sin(\pi/4))$	(1,0)

The initial reconstruction was performed with parameters $\omega_u = 1, \omega_v = 1$, which corresponds to the isotropic Gaussian filter described by Adler [33] with a spatial break frequency of 10% of the diameter.

In order to verify the repeatability of the experiment, three coupons were made from each stacking sequence. Thus, the total number of coupons was nine. An example of the sample set is shown in Figure 6.2,

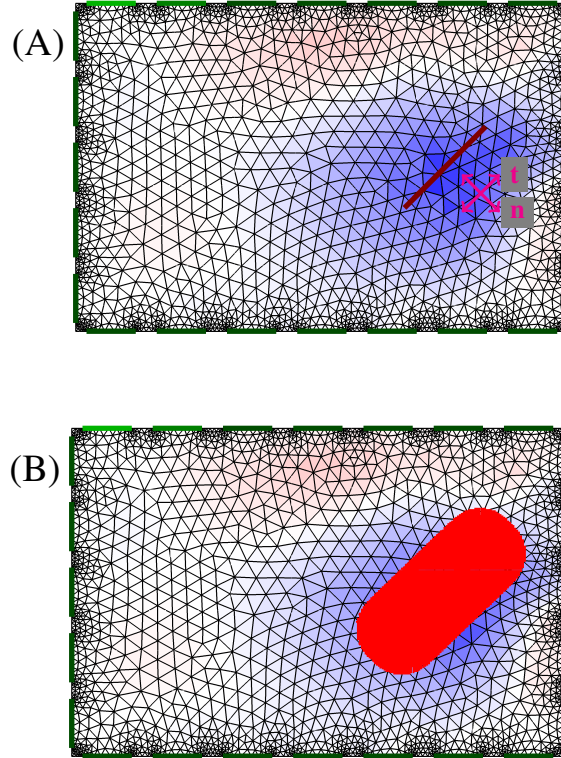


Figure 6.1: Filter setup according to the nominal position of the first defect in a reconstructed image via (A) isotropic Gaussian smoothing filter and (B) selected area of the anisotropy with a width of 26.3 mm.

together with a detail of the performed cuts. The experiment was performed in two phases. First, the cut was applied to the right half of the sample (hereafter referred to by the index R) and then to the right half (hereafter referred to by the index LR).

The measurements for this experiment were performed using the measurement chain described in Chapter 4.2.1. The choice of an adjacent measurement pattern to avoid the mirroring effect and an opposite stimulation pattern to improve the penetration of the sample by the electric current was necessary here. An illustration of the differential boundary voltage between a defect and a non-defect coupon is shown in Figure 6.3. The waveforms correspond to the average values through the dataset for each stacking sequence. The standard deviations also illustrate an idea of the signal-to-noise ratio. The standard deviations are intentionally doubled here to visualize them better.

6.1.2 Assessment of Gaussian anisotropic filter for crack detection

To more objectively assess the impact of the anisotropic filter on the reconstruction of the simulated crack, the image reconstructions were processed by 2D cross-correlation. The correlated image was the binary image obtained by thresholding the half amplitude (HA) with the binary image of the nominal slice position. The cross-correlation of HA regions was inspired by the values processed within GREIT[71] (Graz consensus Reconstruction algorithm for EIT), which characterizes the quality of image reconstruction using a metric based on a set of criteria for point inhomogeneity images. For an objective assessment of the anisotropic filter, it was preferable to use cross-correlation because of its independence from the reconstructed shape. The correlation coefficients of the images obtained with the isotropic filter are given in Table 6.2, while the coefficients for the anisotropic filter are shown in Table 6.3.

The cross-correlation coefficients indicate the improvement in the reconstructed images, which is also evident also from their visual comparison. The cross-correlation coefficients were increased by approximately twice by the Gaussian anisotropic filter. Except for the asymmetric composition, which slightly deviates from its values, the values are consistent.

Table 6.2: Cross-correlation coefficients between the images obtained with isotropic smoothing and the nominal image (red line in the images above) for quasi-isotropic (A), orthotropic (B), and asymmetric (C) stacking sequence.

stacking sequence	A_R/A_{LR}	B_R/B_{LR}	C_R/C_{LR}
quasi-isotropic	0.12/0.08	0.12/0.08	0.12/0.08
orthotropic	0.12/0.08	0.12/0.09	0.12/0.08
asymmetric	0.15/0.13	0.15/0.15	0.15/0.15

Table 6.3: Cross-correlation coefficients between the images obtained with anisotropic smoothing and the nominal image (red line in images above) for quasi-isotropic (A), orthotropic (B), and asymmetric (C) stacking sequence.

stacking sequence	A_R/A_{LR}	B_R/B_{LR}	C_R/C_{LR}
quasi-isotropic	0.21/0.22	0.22/0.21	0.21/0.21
orthotropic	0.21/0.22	0.22/0.21	0.21/0.21
asymmetric	0.26/0.23	0.20/0.23	0.24/0.24

Another observed parameter was the solution error (SE) defined as follows:

$$e = \|\mathbf{z} - h(\mathbf{s}_{rec})\|_2 / \|\mathbf{z}\|_2, \quad (6.5)$$

where $h(\mathbf{s}_{rec})$ is the solution of the forward problem with the setup described above and \mathbf{s}_{rec} is the reconstructed conductivity. The equation 6.5 of the SE defined as above describes how much the measured boundary voltages differ from the voltages simulated by the forward model. The percentage changes in the SE between images reconstructed by anisotropic and isotropic smoothing are summarized in Table 6.4. Absolute values of the SE are summarized in Table 6.5 for the damage on the right side and in Table 6.6 for damage on both sides. It shows that the SE is improved by the anisotropic Gaussian smoothing filter approximately in the range from 5 to 10 %.

Table 6.4: Percentage changes in the solution error of the image reconstructions with the damage on the right (R) and both (LR) sides after applying anisotropic smoothing for quasi-isotropic (A), orthotropic (B), and asymmetric (C) stacking sequence.

stacking sequence	A_R/A_{LR}	B_R/B_{LR}	C_R/C_{LR}
quasi-isotropic	94.1/94.7	94.1/94.7	94.1/94.7
orthotropic	93.5/93.5	93.0/93.1	93.3/93.4
asymmetric	90.6/90.7	91.3/91.3	90.9/91.5

An example of the image reconstructions is presented in Table 6.7. Although the damage detection capability of the Gaussian anisotropic filter is performed on nine specimens in total, only three are depicted. The reason is that the high repeatability led to practically identical images. For the purpose of filter functionality demonstration, all the measurements are also processed by isotropic Gaussian smoothing with a spatial cut-off frequency of 10% of the diameter. In both cases, the low resolution and diffuse nature of the ERT image are clearly seen. As is expected in the case of image focusing, the elements with an amplitude above the HA level (HA set) are colored by a semi-transparent green color for focus highlighting. A mere visual comparison of the images reconstructed by both the isotropic and anisotropic filters reveals improvement in the focusing.

It can be expected that better results will be yielded by the quasi-isotropic laminate stacking sequence because it is closest to the used isotropic numerical model. However, the HA set of the images obtained by the reconstruction with the isotropic filter together with the correlation coefficients indicates that better results are obtained by the asymmetric laminate stacking sequence. The reason is probably the higher sensitivity in the longitudinal direction owing to the higher electrical conductivity given by the larger number of carbon fibers. Asymmetric laminate stacking sequence apparently has a larger amplitude, so the HA set declines in the overall area. Nevertheless, from the visual comparison of all the images reconstructed by the anisotropic filter, it is evident that the asymmetric laminate stacking sequence leads to less contrast sharpness in the reconstructed image. Contrast sharpness between the beginning of the contrast given by the

Table 6.5: Absolute values of the solution error of the image reconstructions with the damage on the right side after applying isotropic (I) and anisotropic (A) smoothing for quasi-isotropic (A), orthotropic (B), and asymmetric (C) stacking sequence.

stacking sequence	A_A/A_I	B_A/B_I	C_A/C_I
quasi-isotropic	0.55/0.58	0.53/0.56	0.53/0.56
orthotropic	0.50/0.53	0.48/0.52	0.50/0.54
asymmetric	0.46/0.51	0.50/0.55	0.49/0.54

Table 6.6: Absolute values of the solution error of the image reconstructions with the damage on both sides after applying isotropic (I) and anisotropic (A) smoothing for quasi-isotropic (A), orthotropic (B), and asymmetric (C) stacking sequence.

stacking sequence	A_A/A_I	B_A/B_I	C_A/C_I
quasi-isotropic	0.50/0.53	0.50/0.53	0.50/0.53
orthotropic	0.47/0.50	0.46/0.50	0.48/0.51
asymmetric	0.44/0.48	0.45/0.50	0.46/0.50

blue color and the beginning of the HA set given by the green color is noticeable from a distance. Thus, the asymmetric composition yields a better correlation coefficient, but it is evident from the visual comparison that it exhibits a worse sharpness after applying the filter. Therefore, a methodology of image comparison via cross-correlation must be treated cautiously. The decrease in the posedness of the inverse problem in the case of laminate stacking sequence for both filters also confirms the presence of reconstruction error, which is discussed in the following chapter.

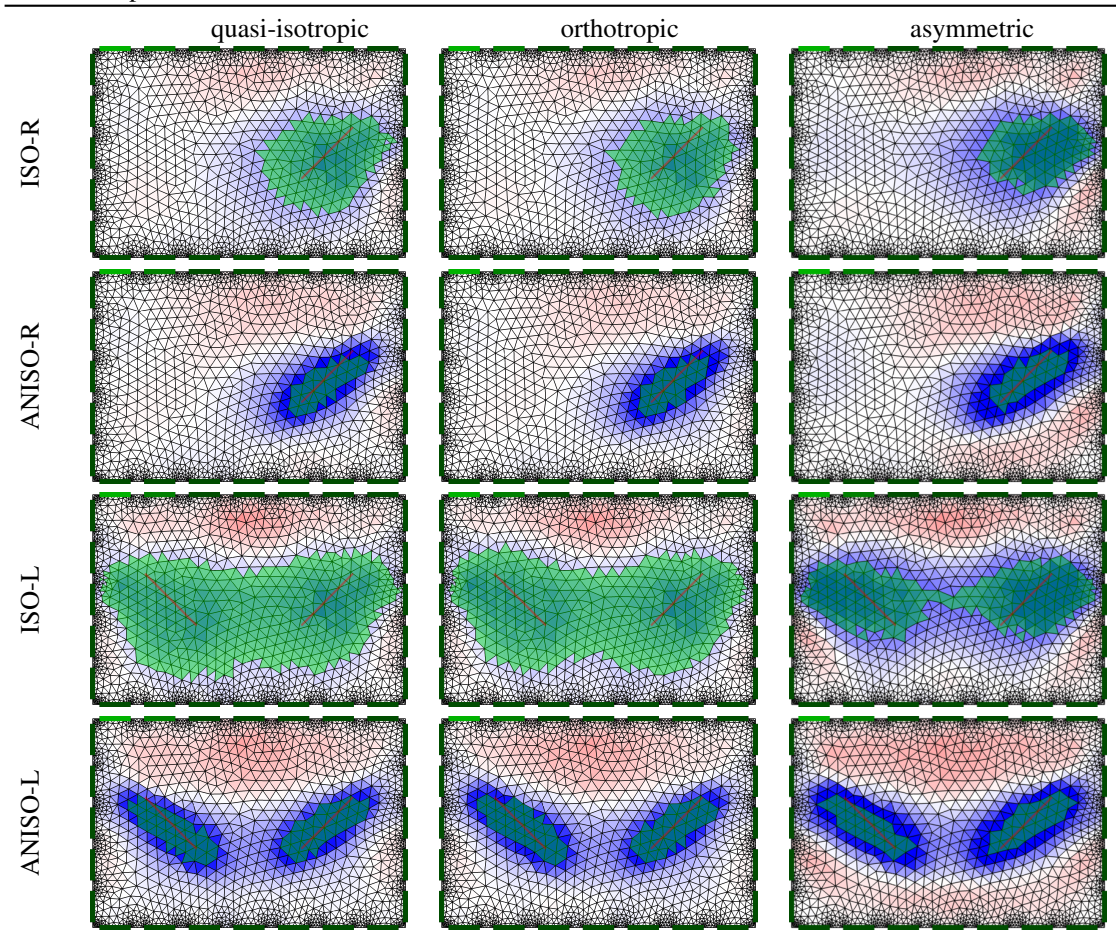
Automation of filter usage in SHM

In this study, the Gaussian anisotropic smoothing filter was used manually. The directions of the smoothing were entered by the user according to the nominal position of the damage. Nevertheless, for the practical use of such filters for the purposes of SHM, the filter should be used automatically. To this end, a detailed analysis of the aforementioned SE and cross-correlation was performed during the filter setup.

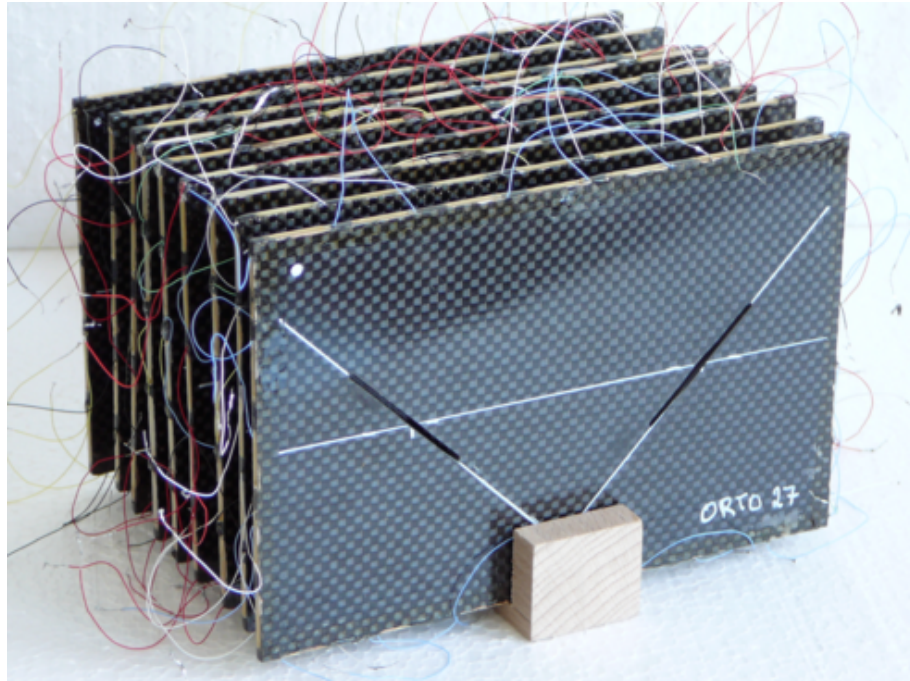
The filter design phase provided an opportunity to study the possible automation of the filter to find the position and direction of the crack. To this end, the SE values of the cross-correlation (XCs) were observed for several different assumptions of crack position and size around the nominal defect position. The SE and XCs values for several assumptions are shown in Table 6.1.2. The assumption in the table is progressively deteriorating from top to bottom. It is well seen from the SE and XCs values that the reconstruction error increases while the cross-correlation decreases. Both reconstructed image quality metrics show a worsening trend with deteriorating assumption accuracy. Other positions elsewhere in the image show a larger reconstruction error or a smaller cross-correlation value. In addition, beyond these observations, the effect of the width of the region with the predicted crack occurrence was examined, confirming the clear outlier of the observed metrics.

Based on the results in Table 6.1.2, it can be concluded that the Gaussian anisotropic filter can be used for automated crack search, e.g. by iterative search based on SE minimization or XC maximization. The found set of reconstruction matrices can be used to locate the position and direction of the searched crack.

Table 6.7: Examples of the image reconstructions obtained with the isotropic (ISO) and anisotropic (ANISO) Gaussian smoothing filters. Green elements indicate the HA set, whereas the red line indicates the nominal position of the crack.



(A)



(B)



Figure 6.2: Set of CFRP specimens (A). One specific specimen of dimensions 150×100 mm with defects (B) of the length of 35 mm positioned at coordinates $X: \pm 37.5$ mm; $Y: 0$ mm at an angle $\pm 45^\circ$ with a width of 1 mm.

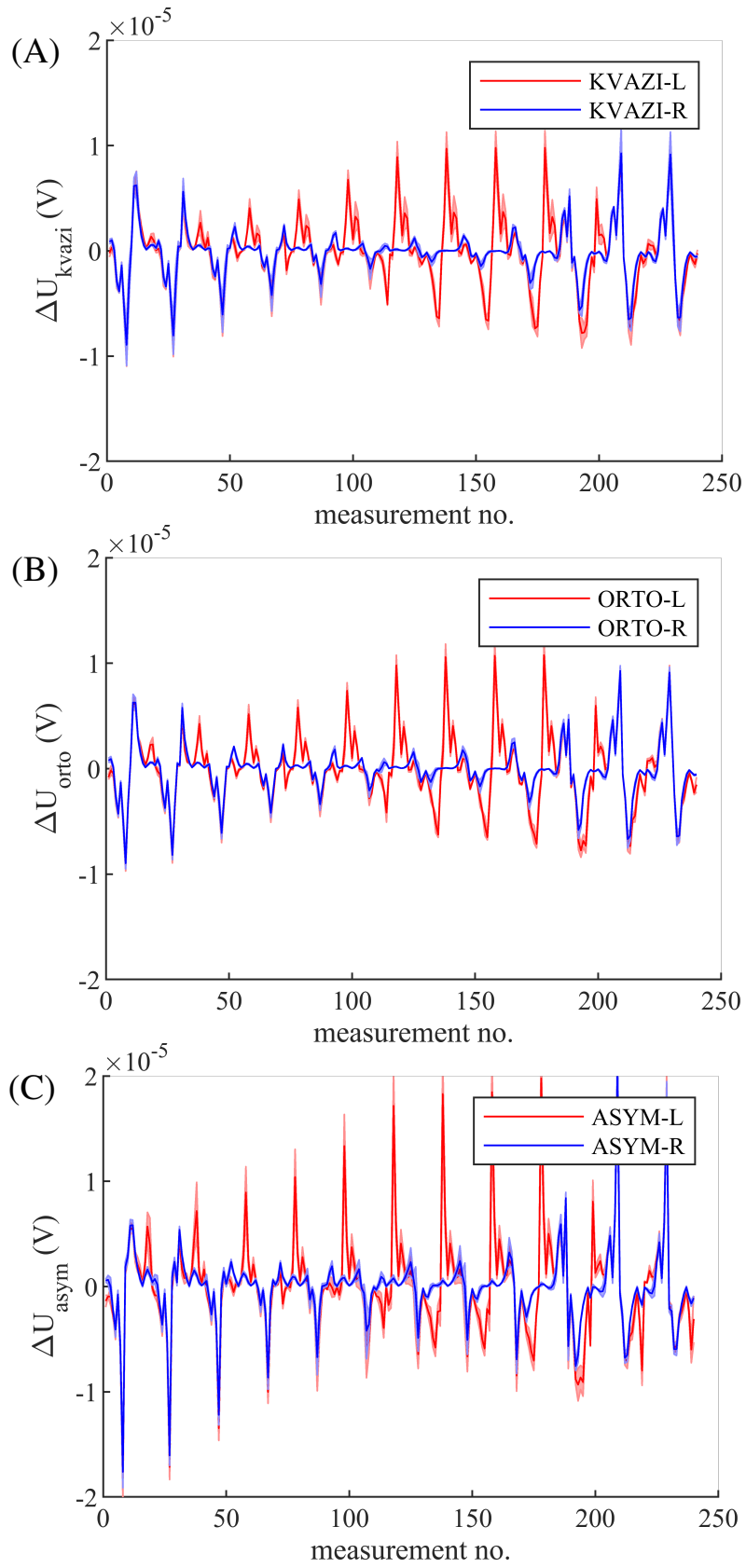
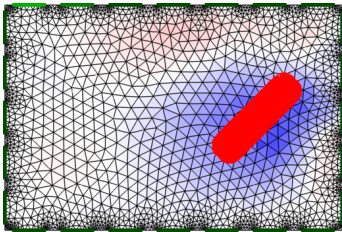
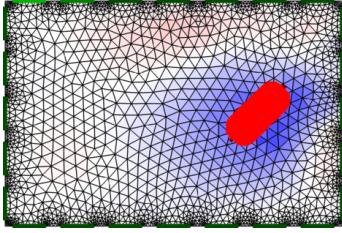
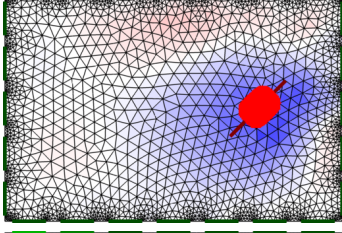
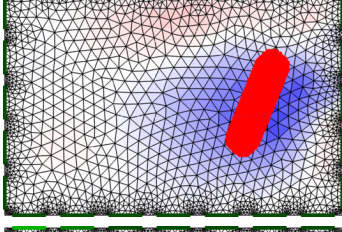
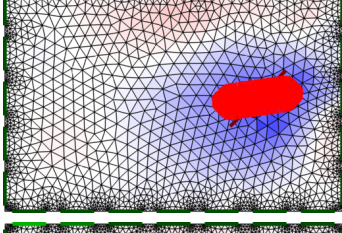
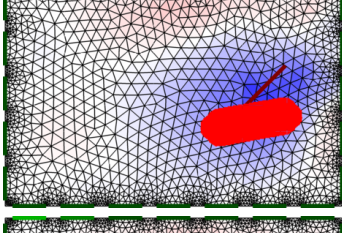
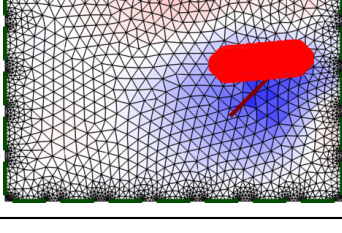


Figure 6.3: Average differential values with double standard deviations of the boundary voltage potentials for (A) quasi-isotropic, (B) orthotropic, and (C) asymmetric coupons with first damage on the right side (blue) and second on the left side (red).

Table 6.8: Error reconstruction (SE) with cross-correlation (XC) for several different assumptions about crack position and direction for a coupon with quasi-isotropic laminate composition.

position	SE	XC
	0.576	0.137
	0.578	0.133
	0.579	0.130
	0.579	0.130
	0.581	0.126
	0.586	0.107
	0.584	0.111

Chapter 7

Optimization of electrode position and shape

7.1 Motivation to optimize electrode position and shape

Key ERT parameters, such as the regularization parameter (hyperparameter), the choice of the measurement or excitation pattern, or the choice of the finite element mesh, are generally given considerable attention in ERT system design. However, there are a number of other parameters that are worthy of attention. One such parameter is the position and size of the electrodes, especially when the considered domain exhibits a more complex geometry. When designing the distribution of electrodes in a domain with more complex geometry, a common problem is to correctly decide which constellation of electrodes will be more advantageous with respect to the resulting image reconstruction and with respect to the constraints, which are mainly the limited number of electrodes (depending on the instrumentation used) and the structural constraints (resulting from the diversity of the design).

In Chapter 5 the issue of BVID detectability by ERT was studied. The motivation to optimize electrode parameters is also based on the BVID detection issue.

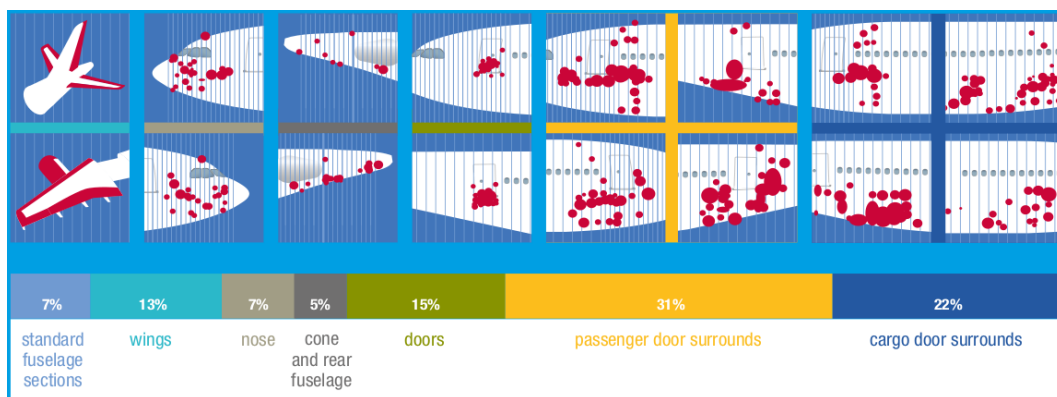


Figure 7.1: Distribution map of damage to the fuselage. Damaged areas are marked in red. Areas around the doors show a high concentration of damage due to ground handling. (taken from FAST, Airbus Technical Magazine, August 2014)

Based on the known statistics on the most frequent occurrence of BVID, e.g., the illustration on the Airbus design (see Figure 7.1), it is possible to identify locations as candidates for ERT application for permanent monitoring of the occurrence of these defects. Examples could be the area around the entrance door or the wing's leading edge. If any of these areas are to be considered as an area of interest for BVID monitoring, the location and size of the individual electrodes should be selected as part of the ERT system design. In such a case, it may not be possible to maintain a uniform distribution of electrodes, or it may be difficult to decide due to the finite number of channels of the instrumentation under consideration. In this case, it may be helpful to use a tool capable of making this decision. It is here, then, that the motivation for studying this issue lies.

One of the earliest works on this topic was done by Paulson et al. [72], who showed that the optimal electrode configuration is when the excitation electrodes are separated from the measurement electrodes, with the size of the excitation electrodes maximized as far as possible, while the size of the measurement electrode is minimized and its distance from the excitation electrode maximized. Another work dealing with electrode optimization is the work of Wang et al. [73], who found the optimal parameters and number of so-called compound electrodes. Other work in this area was done by Galvis et al. [74], who used the effective independence method to find the optimum in electrode selection, and this was in the case of delamination detection. However, the most general approach was shown by Hyvonen et al. [75], who derived optimality criteria based on a Bayesian approach that incorporated the available a priori information about the conductivity distribution.

7.2 Selection of tools and model parameters

For the purpose of solving the above-mentioned problem of optimizing the position and shape of the electrodes (or their length in the case of 2D geometry), genetic algorithms (GA) are used in the following investigation, as they allow the easy inclusion of arbitrary aspects in the optimization, without the need to use the often complex mathematical framework.

7.2.1 Optimization scheme

The essential prerequisite for the implementation of genetic algorithms is the choice of a suitable fitness function. The fitness function should be reasonably sensitive to the parameter to be optimized, and it would be beneficial if it also includes the evaluation of indirectly related aspects. Thus, in the case of optimizing electrode parameters for BVID detection in the region of interest, the conductivity image reconstruction needs to be performed as best as possible considering the occurrence of point inhomogeneity, which BVID is. The optimization should therefore ensure the circularity of the point inhomogeneity image and minimize noise or other artifacts elsewhere in the image. The above-outlined requirements for the fitness function are well satisfied by the image reconstruction error 6.5.

Since the calculation of the reconstruction error requires the reconstruction to be performed first, it is necessary to simulate the boundary voltages first. Thus, the evaluation of each candidate solution is generally a sequence of the following steps:

1. preparation of the candidate solution based on GA (position and size of electrodes),
2. preparation of the forward model and simulation of the forward problem (simulation of boundary voltages) both for the case of homogeneous conductivity distribution and for the case when inhomogeneity simulating the impact is placed in the region of interest (choice of the region of interest),
3. preparation of inverse model (with different finite element mesh) and calculation of inversion based on the expansion of the boundary voltages from the previous step,
4. calculation of reconstruction error and possibly other observed metrics.

The preparation of the candidate in the first step will be described below. Its implementation is strongly dependent on the data representation of the solution. In the second step, it is necessary to obtain simulated boundary voltages on the forward model, which is generally desirable to refine (higher mesh density, more realistic geometry without simplification,...). However, in the second step, it is not desirable to add measurement noise in an attempt to approximate real measurements, as this would unnecessarily degrade the optimization. At the same time, the second step implicitly hides the critical element of the whole optimization implementation, which is the selection of the region of interest for which the electrode configuration is optimized. Since this work is concerned exclusively with differential image reconstruction, this problem is also viewed in terms of differential reconstruction. Thus, by placing the inhomogeneity in the region of interest to simulate the boundary voltages for optimization, defacto "focusing" into this region by the electrode configuration occurs. In step three, a difference reconstruction is then performed on a simplified model with the chosen electrode configuration from step one, which will be used for reconstruction in the future after the ERT setup is designed. Finally, the calculation of the evaluation function and other metrics can then be performed. The fitness function expressing the quality of the solution is then included in the GA along with the solution, and the whole process is repeated for each additional candidate in the GA.

7.2.2 Data representation of solution

The first and fundamental step of the optimization implementation is the selection of a suitable data representation, the so-called genome. The essential requirement for the data representation is, in addition to an accurate description of the solution to the optimization problem, the ability to easily implement mutation and crossover operators over the chosen data type.

In the case of a 2D finite-element network, the electrode configuration can be represented by a vector of numbers whose values encode the electrode information for each edge at the boundary of the domain. An example might be a four-electrode system, where each electrode is two edges long, with a gap of one edge length between the electrodes. The genome, in this case, looks like this:

$\langle 1, 1, 0, 2, 2, 0, 3, 3, 0, 4, 4, 0 \rangle$.

7.2.3 Mutation operator

The mutation operator must provide subtle changes to the solution so that subtle improvements to the solution across generations can be achieved as part of the GA optimization. The proposed mutation operator randomly performs one of the following six operations on a randomly selected electrode: increasing/decreasing the length of the electrode in the forward or backward direction or moving the electrode forward or backward. If one of these operations is blocked by the adjacent electrode, an attempt is performed to move the adjacent electrode. The mutation is terminated without effect if the second electrode is also blocked. The mutation is described using the pseudocode in Algorithm 1.

Algorithm 1 Tweak

```

1: function TWEAK( $G, e$ )
2:    $i \leftarrow GetElectrodeFirstIndex(G, e)$ 
3:    $j \leftarrow GetElectrodeLastIndex(G, e)$ 
4:    $k \leftarrow$  random integer from 1 to 6
5:   if  $k = 1$  then                                     ▷ add element at the front
6:      $G_{i-1} \leftarrow e$ 
7:   else if  $a = 2$  then                                   ▷ add element at the end
8:      $G_{j+1} \leftarrow e$ 
9:   else if  $a = 3$  then                                   ▷ remove element at the front
10:     $G_i \leftarrow 0$ 
11:  else if  $a = 4$  then                                   ▷ remove element at the end
12:     $G_j \leftarrow 0$ 
13:  else if  $a = 5$  then
14:    if  $j + 2 \neq 0$  then                               ▷ push following el. forward
15:       $G \leftarrow PushElectrode(G, e + 1)$ 
16:       $G_{j+1} \leftarrow e$                                ▷ push electrode forward
17:       $G_i \leftarrow 0$ 
18:    else if  $a = 6$  then
19:      if  $i - 2 \neq 0$  then                               ▷ push following el. backward
20:         $G \leftarrow PushElectrode(G, e - 1)$ 
21:         $G_{i-1} \leftarrow e$                              ▷ push electrode backward
22:         $G_j \leftarrow 0$ 
23:  return  $G$ 

```

7.2.4 Crossover operator

The crossover operator must ensure that the best properties of any two candidates can be combined. The crossover can be made straightforward by averaging the lengths of the individual electrodes and the individual gaps between them, thanks to a suitably chosen genome. Once the averaging is done, the total length is aligned to the length of the number of edges by adding/removing a randomly selected element from the genome, thus introducing additional randomness into the process. More randomness prevents the solution from getting stuck due to its premature maturity. The operator is described by the pseudocode in Algorithm 2.

Algorithm 2 Crossover

Require: Length(P1) = Length(P2)
Require: Max(P1) = Max(P2)
Ensure: Length(P1) = Length(C)
Ensure: Max(P1) = Max(C)

```
1: function CROSSOVER(P1, P2, MinL)
2:   NumOfElec  $\leftarrow$  Max(P1)
3:   NumOfEdgs  $\leftarrow$  Length(P1)
4:   e  $\leftarrow$  GetElectrodesAverageLengths(P1, P2)
5:   g  $\leftarrow$  GetGapsAverageLengths(P1, P2)
6:   C  $\leftarrow$  {}
7:   for i from 1 to NumOfElec do
8:     elec  $\leftarrow$  vector of electrode i with a length of ei
9:     gap  $\leftarrow$  vector of zeros with a length of gi
10:    C  $\leftarrow$  C  $\cup$  {elec  $\cup$  gap}
11:  repeat
12:    p  $\leftarrow$  random integer from 1 to NumOfEdgs
13:    if Length(C) < NumOfEdgs then
14:      k  $\leftarrow$  Cp
15:      C  $\leftarrow$  insert k into C on the position p
16:    else
17:      L  $\leftarrow$  length of electrode/gap on the pos. p
18:      if L > MinL then
19:        C  $\leftarrow$  remove elem. of C on the pos. p
20:  until NumOfEdgs=Length(C)
21:  return C
```

7.2.5 Genetic algorithm

The classical genetic algorithm iterates through the population by evaluating the fitness function of each candidate, selecting parents and performing crossovers, and finally rearranging the population. More about GA can be found in the book [76].

Based on the first experimental experience in the problem of electrode parameter optimization, the GA with elitism was combined with the "steepest ascent hill-climbing algorithm." The "stochastic universal sampling" algorithm was chosen to select parents for crossover purposes, which ensures that at least one better candidate is always selected. The combination of this "hill-climbing" algorithm with the GA proved to be the most efficient, roughly in the proportion that most of the time, only mutation by the hill-climbing algorithm was performed, while crossover was performed with low probability. Thus, a certain number of candidates (population) were mutated by the climbing algorithm most of the time, and once in a while, crossover and population reassembly was performed. The optimization parameters used for the search in the following numerical experiments were as follows:

- optimization length: 500 iterations,
- population size: 16 candidates,
- number of elites: 4,
- crossover probability: 0.01 %.

In the proposed procedure, only the alignment of the mesh edges to the electrodes is changed, not the mesh itself. Only in this case, the chosen fitness function (reconstruction error) reflects well the changes in the quality of the image reconstruction associated with changes in the electrode geometry. This is because, in most observed cases, the effects of changes to the finite element network outweigh the impact of electrode optimization.

The geometry of the used model is a 2D 150x100 mm rectangle, which corresponds to the requirements of the ASTM D7136 standard. The geometry is meshed by Netgen with 3900 triangular elements (2051 nodes) for a forward model and 1300 triangular elements (751 nodes) for an inverse model. Concerning the implementation of the mutation and crossover operators, it is suitable for the boundary elements to be

the same size. The electrodes are, therefore, without mesh refinement. Concerning the measurement and stimulation patterns, for the total number of twenty-four electrodes, an opposite stimulation pattern and an adjacent measurement pattern is used. There are no measurements performed on the stimulation electrodes. The opposite stimulation pattern provides better penetration of the body by the electrical current, while the adjacent measurement pattern ensures avoidance of a mirroring effect. In relation to optimization, simulated boundary voltage potentials are without additive noise. The stimulation current is 5 mA. The homogeneous conductivity of the body is 1 S/m whereas circular inhomogeneity of the radius of 5 mm simulating an impact exhibits the conductivity 0.9 S/m.

7.3 Numerical experiments

The configuration of the first five experiments is unrestricted in electrode movement, and the electrodes are initially placed almost uniformly on the boundary (see Figure 7.2 left). The following five experiments are with motion restriction, where the initial position of the electrodes is in the permissible region (see Figure 7.2 right).

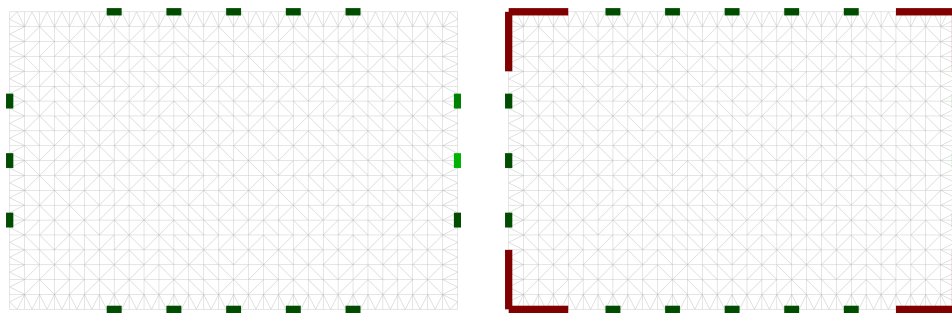


Figure 7.2: Initial electrode configuration for optimization without (left) and with (right) constraint. The constraints are indicated by red marks in the corners.

The positions of point inhomogeneities simulating barely visible impact are summarized in Table 7.1 for each experiment.

Table 7.1: Positions of point inhomogeneities (relative to the coupon center).

Position	X(mm)	Y(mm)
left	-37.5	0
top	0	25
right	37.5	0
bottom	0	-25
center	0	0

The positions were chosen to demonstrate the effect of the assumed position of the searched inhomogeneity on the optimal position of the electrodes. Areas where there is inhomogeneity could be called the focused area. Although the left and right or top and bottom positions are symmetric in axes, optimization has been performed for repeatability verification. Each experiment was conducted seven times, also for repeatability assessment.

The trends of fitness values for particular configurations can be seen in Figures 7.3 and 7.4. Graphs show average values with shaded transparent areas, which depict standard deviations. Both average and deviation were calculated from the entire population of the given configuration. The image reconstructions of the point inhomogeneities with the electrode configuration of the best candidates are depicted in Figure 7.5. The average values and standard deviations of the best fitness functions are depicted in Figure 7.6. Both average and deviation values were calculated from seven optimization runs of each experiment. The values are expressed as a percentage of initial candidate fitness. Figure 7.7 shows changes in position errors. The position error here represents the distance from the nominal inhomogeneity position and the founded position in the COG. As well the changes in amplitudes are depicted in Figure 7.8. Amplitude here is

normalized conductivity change in the COG. The blur radius is defined as $BR = r_z/r_0 = \sqrt{A_z/A_0}$ where r_0 and A_0 are the radius and area, respectively, of the entire 2D medium, while r_z and A_z are the radius and area of the reconstructed contrast containing half of the magnitude of the reconstructed image. The changes in the blur radius are depicted in Figure 7.9. Finally, the downward trend of fitness functions of the configuration top without restriction is demonstrated in Figure 7.10.

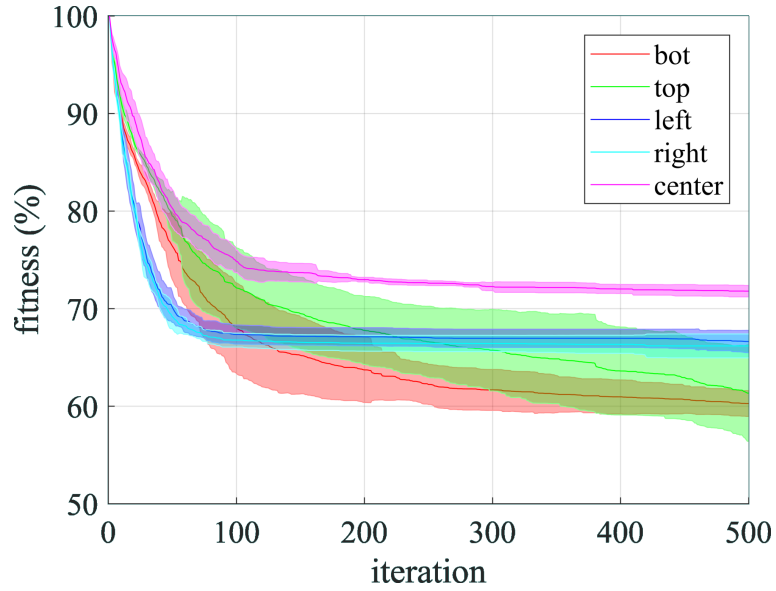


Figure 7.3: Fitness functions of the optimization without restriction (average values with standard deviations).

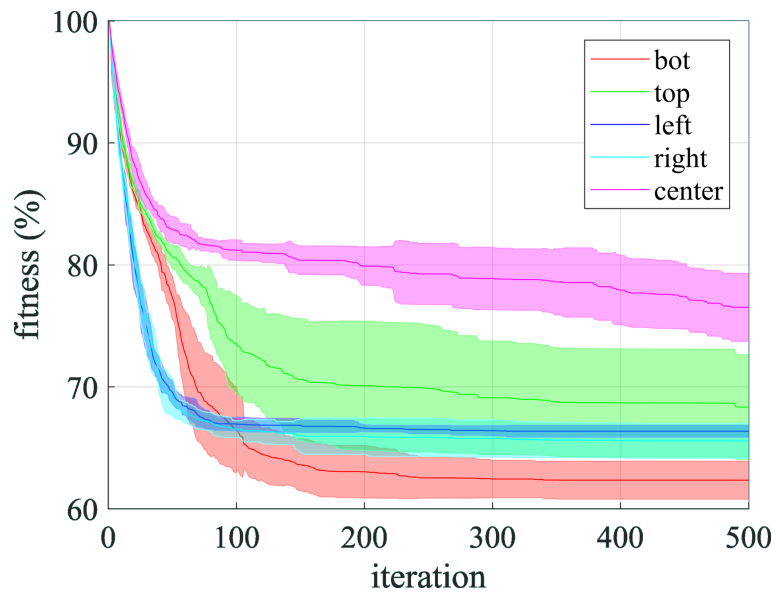


Figure 7.4: Fitness functions of the optimization with restriction (average values with standard deviations).

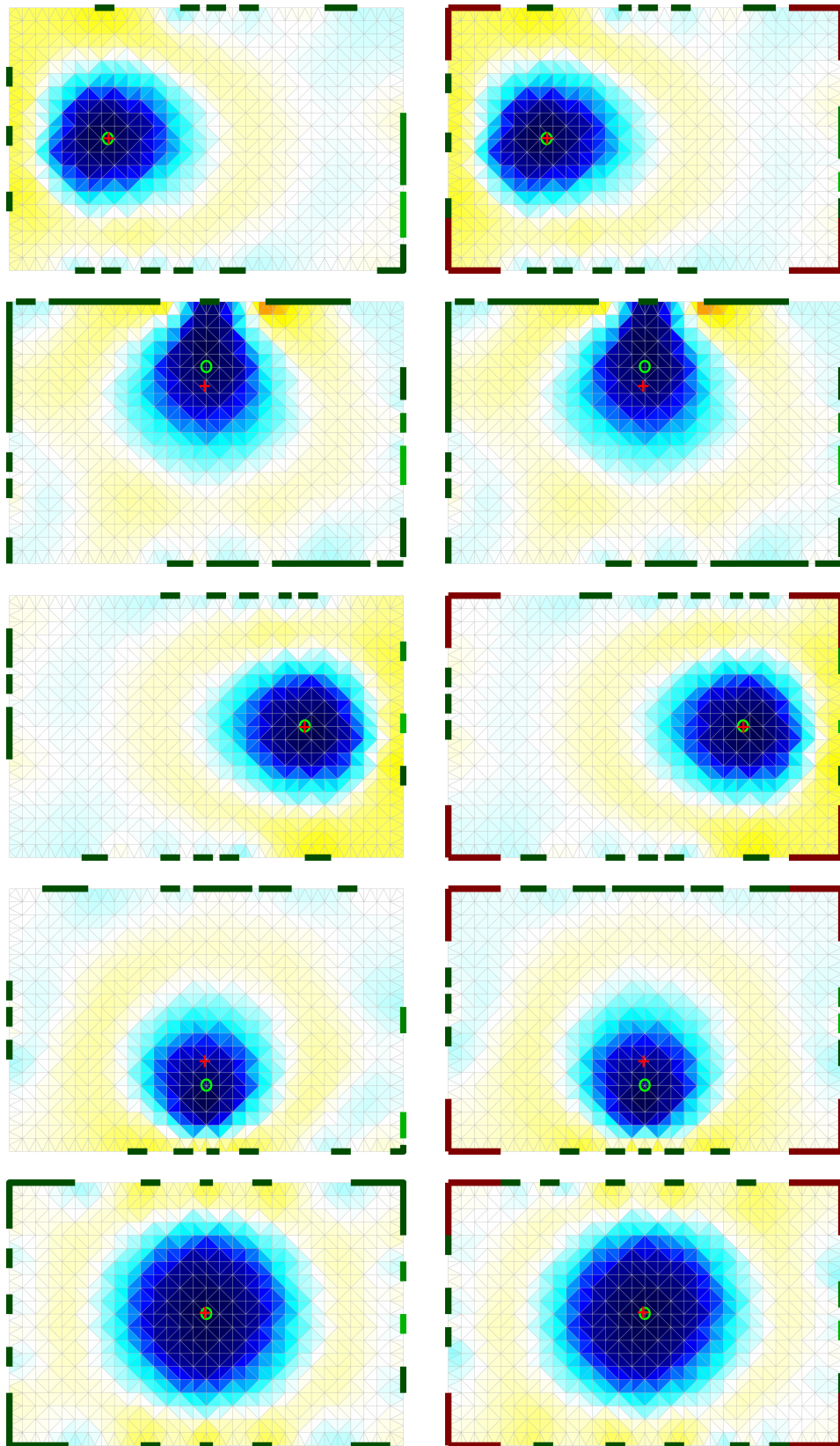


Figure 7.5: The image reconstructions of the point inhomogeneities with electrodes configuration of the best candidates (O - nominal position of the point inhomogeneity; X - a center of gravity).

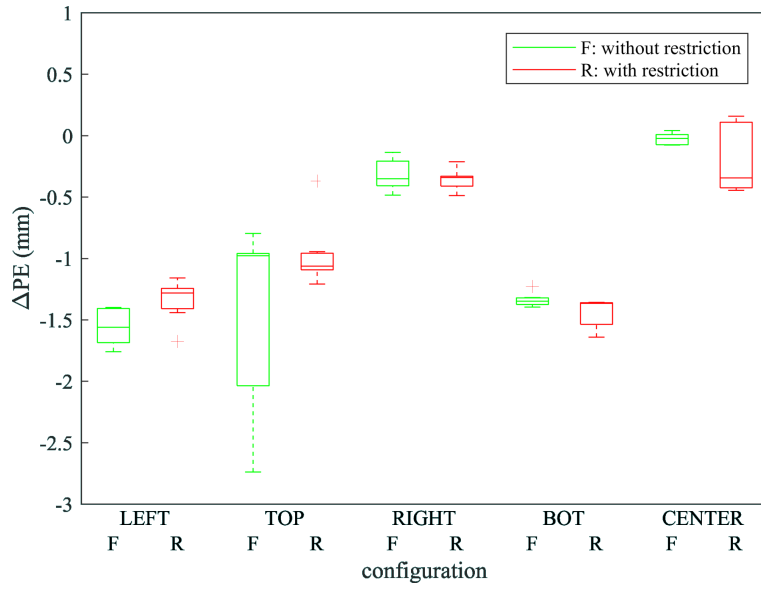


Figure 7.7: Changes in the values of the position errors.

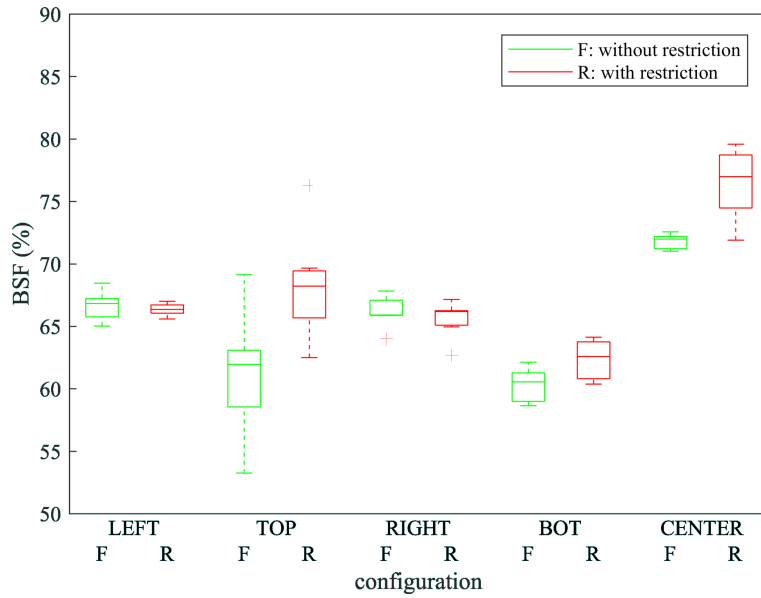


Figure 7.6: Fitness functions of the best candidates after 500 generations. Statistics were performed from 7 independent optimization runs.

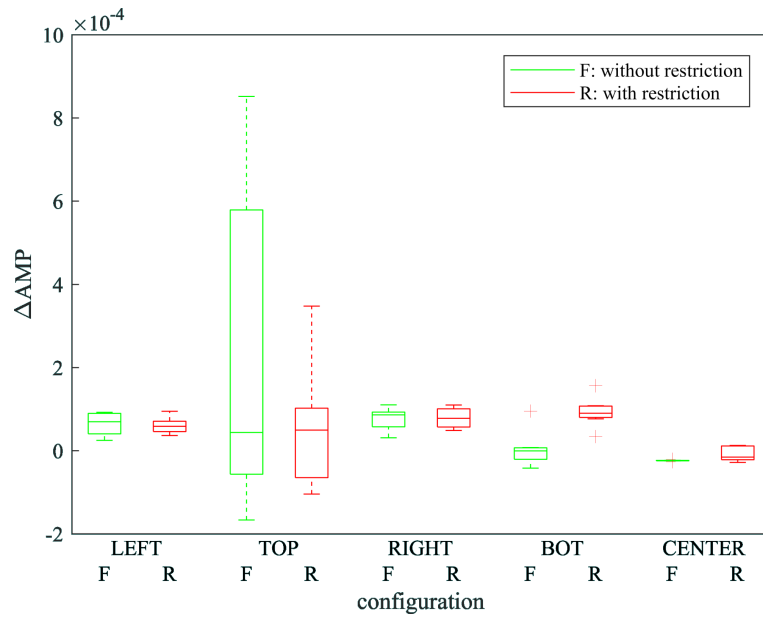


Figure 7.8: Changes in the normalized values of the electrical conductivity in COG.

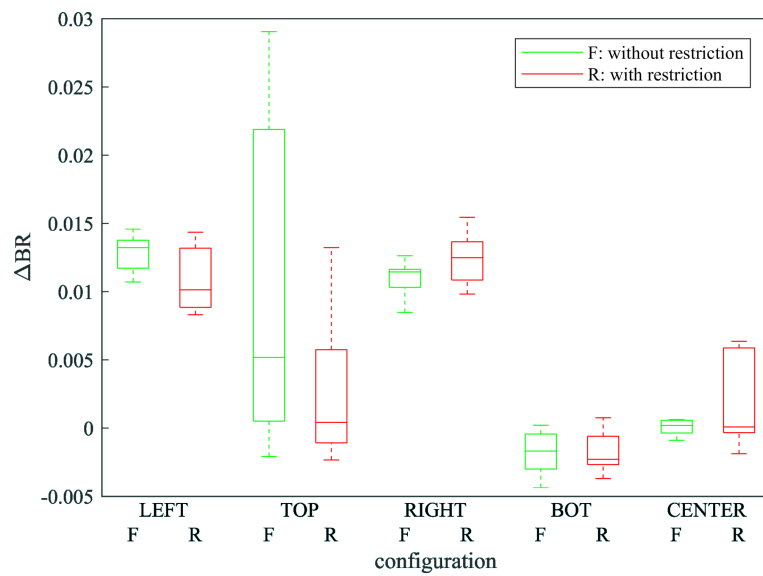


Figure 7.9: Changes in the blur radius.

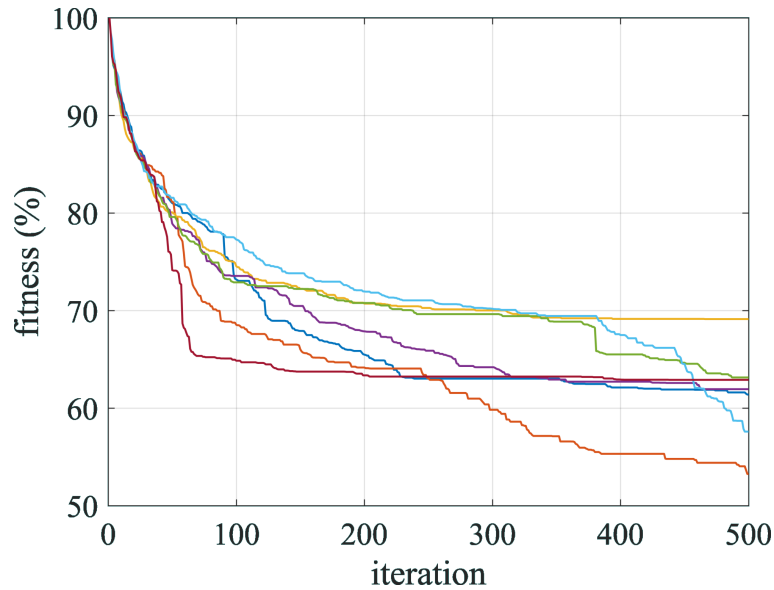


Figure 7.10: Fitness functions of the configuration with inhomogeneity at the top without restriction.

Numerical experiments show that the proposed optimization method is able to reduce the solution error (fitness function) by as much as 40%. As shown by the standard deviation of the fitness functions in the graphs in Figures 7.3 and 7.4, the configuration with the inhomogeneity at the top and bottom always showed worse repeatability due to frequent hanging in the local minimum. An example may be a configuration with inhomogeneity at the top without restriction, whose fitness functions are shown in Figure 7.10. Here, only two runs out of seven have left the local minimum. From the founded electrode configurations depicted in Figure 7.5, it is clear that the electrodes more distant from the point inhomogeneity are larger than the electrodes close to point inhomogeneity. This behavior is confirmed especially by the configuration with inhomogeneity at the bottom without restriction, along with configurations with inhomogeneity at the top and bottom with restrictions. Another example is the configuration with inhomogeneity at the center without restriction, where the largest electrodes have grown in the corners that are farthest from the center. The only exception is the configuration with inhomogeneity at the top without restriction, whose reconstruction error has looked towards the minimum since the start of the search (see fitness on Figure 7.10). This electrode configuration shows that in the other configurations with inhomogeneity at the top and bottom are only the local minima. More details from the optimization of the configurations described here are given in appendix A, where each BSF candidate from the seven runs is listed. It also lists all observed metrics for each founded solution.

The most practical indicator of the optimization benefit is the position error. As can be seen in the graph in Figure 7.7, in the extreme case, the position error was reduced by 2.5 mm. Other position errors were around 1 mm. Reducing the position error close to 1 mm seems to be inexpressive. However, in the case of the configuration with the inhomogeneity at the top without restriction, the improvement is noticeable. From the observed behavior of the fitness functions, it can be concluded that by increasing the number of optimization iterations, it would certainly reduce the positional error even in other configurations. Regarding the effect of optimization of the parameters of amplitude and blur radius, from the graphs in Figures 7.8 and 7.9, it can be stated that there have been no significant changes. Here, it is suitable to remind that the observed parameters exhibited changes related to the initial (almost even) distribution of the electrodes. All optimization was made for the ideal case without noise, which may be the reason for the relatively low impact of optimization on the observed parameters. The primary observed value of the reconstruction error, on which optimization was performed, decreased by up to 40 %.

Based on the numerical experiments performed, it was possible to formulate a hypothesis that claims that electrodes further away from the region of interest become larger while those closer to the region become smaller. These changes are accompanied by a noticeable improvement in the reconstruction error as well as an improvement in the position error of the barely visible impact. To test such a hypothesis, this thesis proceeded to an experimental verification described in the following section.

7.4 Experiments on a coupon with resistive network

In order to verify the observed behavior in the previous section, a set of experiments was suggested. Thus, the experimental validation will attempt to confirm that shortening the electrodes close to the region of interest and extending them further away from the region of interest will reduce the reconstruction error and, in particular, the position error of the found point inhomogeneity.

7.4.1 Experimental coupon

The implementation of the experimental coupon is done primarily with respect to the need to arbitrarily and repeatedly choose different electrode configurations. In addition, it must be possible to repeatedly apply point inhomogeneity to precisely defined locations in the model domain. For this purpose, an implementation using a resistor network composed of 19×27 square elements was chosen. For the implementation, an SMD resistor of size $1 \text{ k}\Omega$ was chosen, whose size fits well in the network of a universal prototype printed circuit board of $150 \times 100 \text{ mm}$ with a hole pitch of 2.54 mm . All nodes at the edge of the domain formed by such a resistor network were brought out to a hardware contact that was well accessible. By interconnecting any continuous group of these contacts, it was possible to create an arbitrarily long (within the limits of the sample geometry) and arbitrarily positioned electrode or set of electrodes. At the same time, the contacts of some adjacent nodes at selected positions were brought out, allowing the resistance to be connected in parallel, thus creating a point inhomogeneity simulating the change in conductivity due to BVID. The implementation of the coupon is shown in Figure 7.11.

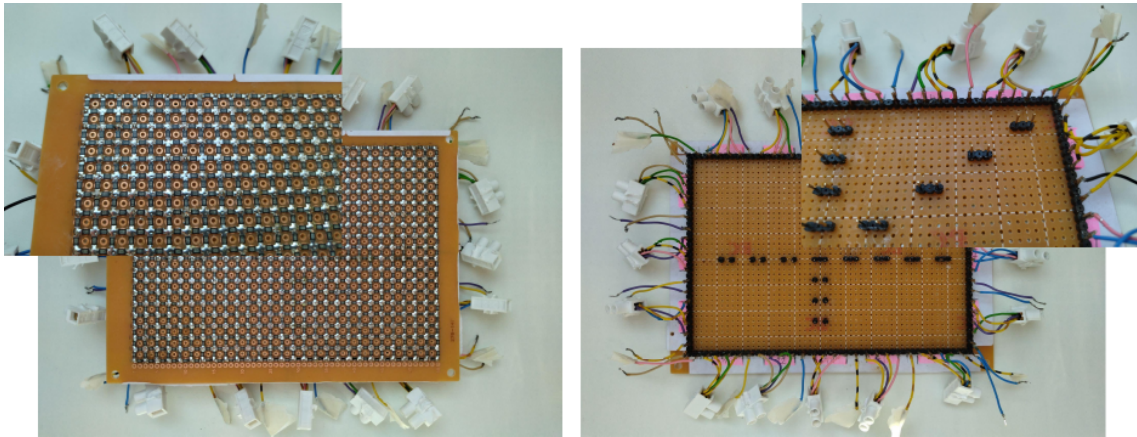


Figure 7.11: Experimental coupon based on the resistor network (19×27 square elements of $1 \text{ k}\Omega$ SMD resistors), with an unlimited choice of electrode configurations.

The simulation of point inhomogeneity was performed by connecting in parallel a resistor of size 100Ω at the positions listed in Table 7.2.

Regarding the electrode configurations of the experimental verification, the following configurations were used: CENTER, LEFT, RIGHT, TOP, and BOTTOM. For the names of the electrode configurations, the analogy of configurations focusing on a specific area is used.

7.4.2 Performed measurements and evaluations

The combinations of inhomogeneity locations at the positions in Table 7.2 for each electrode configuration listed in the Table 7.3 were examined using the experimental coupon outlined above. For the purpose of differential image reconstruction, the state without point inhomogeneity and then with inhomogeneity realized by parallel connection of the resistor to the corresponding location was always examined.

The reconstruction of the image was performed using a model of appropriate geometry reflecting the geometry of the sample. The correctness of the model used and its key parameters (geometry, excitation, measurement pattern, homogeneous conductivity, excitation current) was verified by comparing the boundary voltages obtained by measurement, simulation on the 2D model used, and, for comparison, on the 3D model. Hereafter, the 2D models used were composed of about 1200 elements, while the 3D model used for verification contained 24132 elements. The homogeneous conductivity was set to 2.7 S/m , while the

Table 7.2: Position of applied inhomogeneities in the further experimental verification of the impact of optimization.

ID	x(mm)	y(mm)
R1	10.16	-2.54
R2	25.4	-2.54
R3	40.64	-2.54
L1	-20.32	-2.54
L2	-35.56	-2.54
L3	-50.8	-2.54
T1	-5.08	7.62
T2	-5.08	17.78
T3	-5.08	27.94
B1	-5.08	-12.7
B2	-5.08	-22.86
B3	-5.08	-33.02
CC	-5.08	-2.54

conductivity of the 3D model was 2.4 S/m due to the considered thickness of 5 mm. An example of the boundary voltage comparison is shown in Figure 7.12.

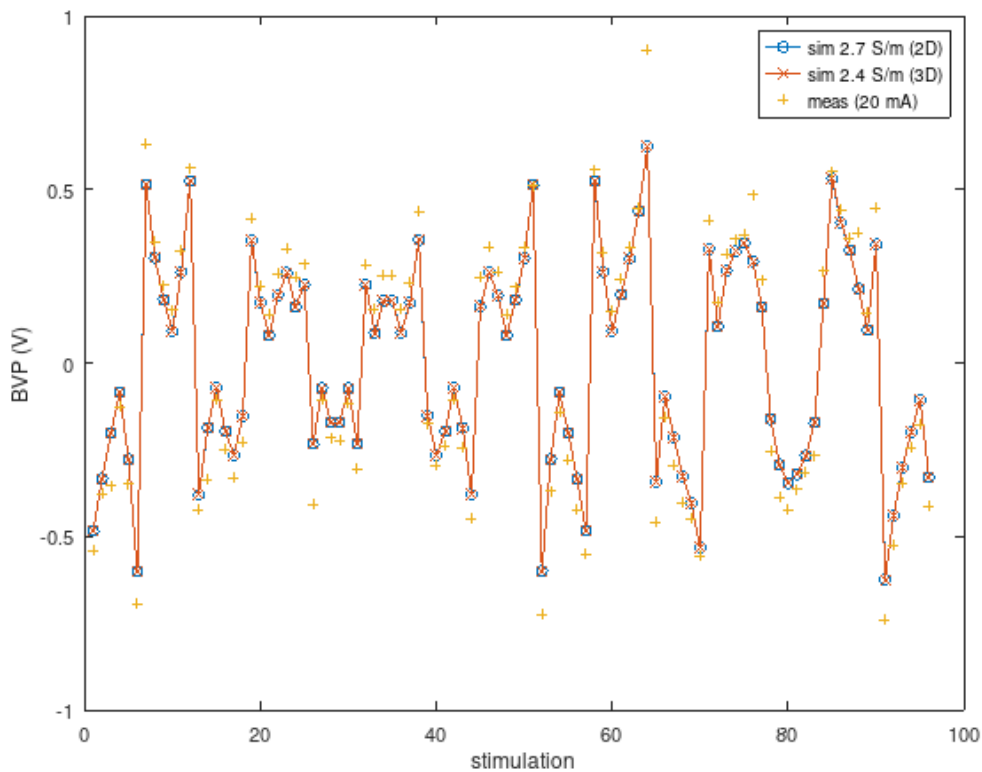


Figure 7.12: Verification of the model by comparing the boundary voltages measured and simulated by the 2D and 3D model.

The measurements were performed with the PXI measurement system (see 4.2.1). An example of one of the measurements is shown in Figure 7.13, where an example of the waveform of the boundary voltages of the homogeneous and inhomogeneous states with the electrodes configured to the right with the inhomogeneity at position R2. Six measurements were always taken and averaged for further processing. The difference signal for image reconstruction also shows the standard deviation calculated from the datasets of

homogeneous and inhomogeneous measurements for comparison.

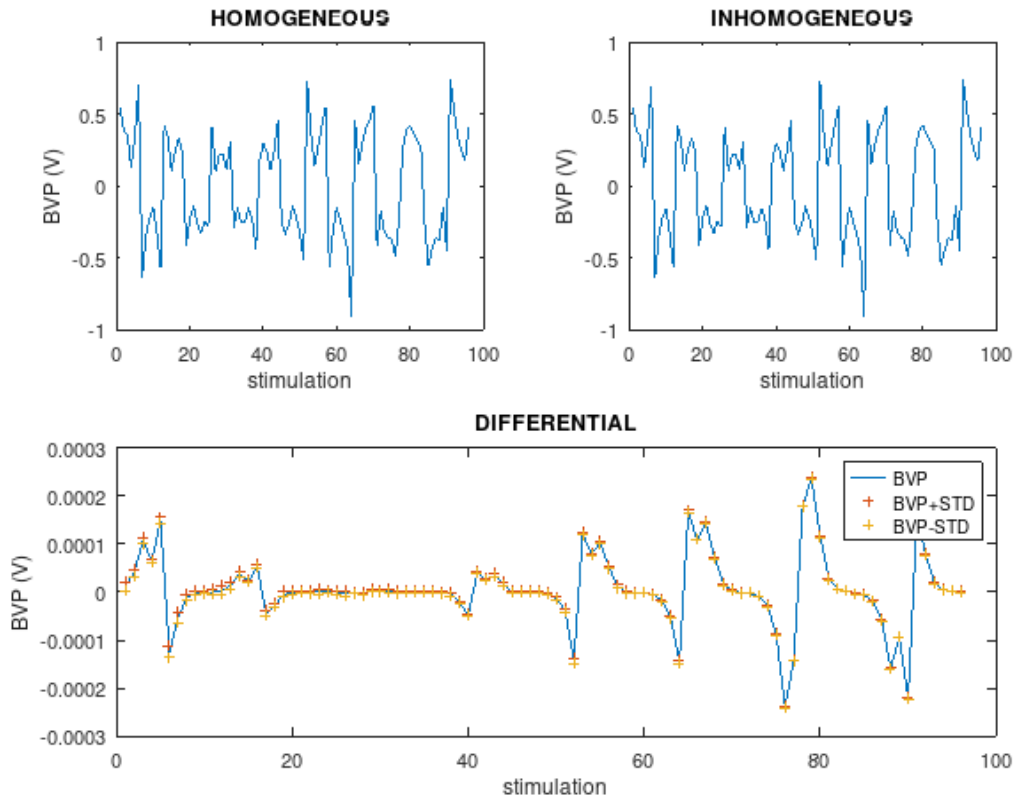


Figure 7.13: Example of measured boundary voltages before (homogeneous state) and after (inhomogeneous state) application of point inhomogeneity.

Each reconstructed image was further processed to find the coordinates of the position of the reconstructed point inhomogeneity or the error of this position relative to the known nominal position. Additionally, the reconstruction error (see relation 6.5) was evaluated along with the amplitude at the location of found inhomogeneity.

In order to verify the observed behavior given by the conclusions of the numerical experiments above, only the combinations on the x-axis and thus the positions of the inhomogeneities **R1**, **R2**, **R3**, **L1**, **L2**, **L3** in combination with the electrode configurations **RIGHT** and **LEFT** were selected from the set of measurements performed. Given the geometry of the coupon, these combinations can be expected to be the most representative when trying to confirm the hypothesis, either positively or negatively. Figure 7.14 shows an example of reconstructions performed with inhomogeneities at R2 and T2 positions with electrode configurations **RIGHT** and **TOP**.

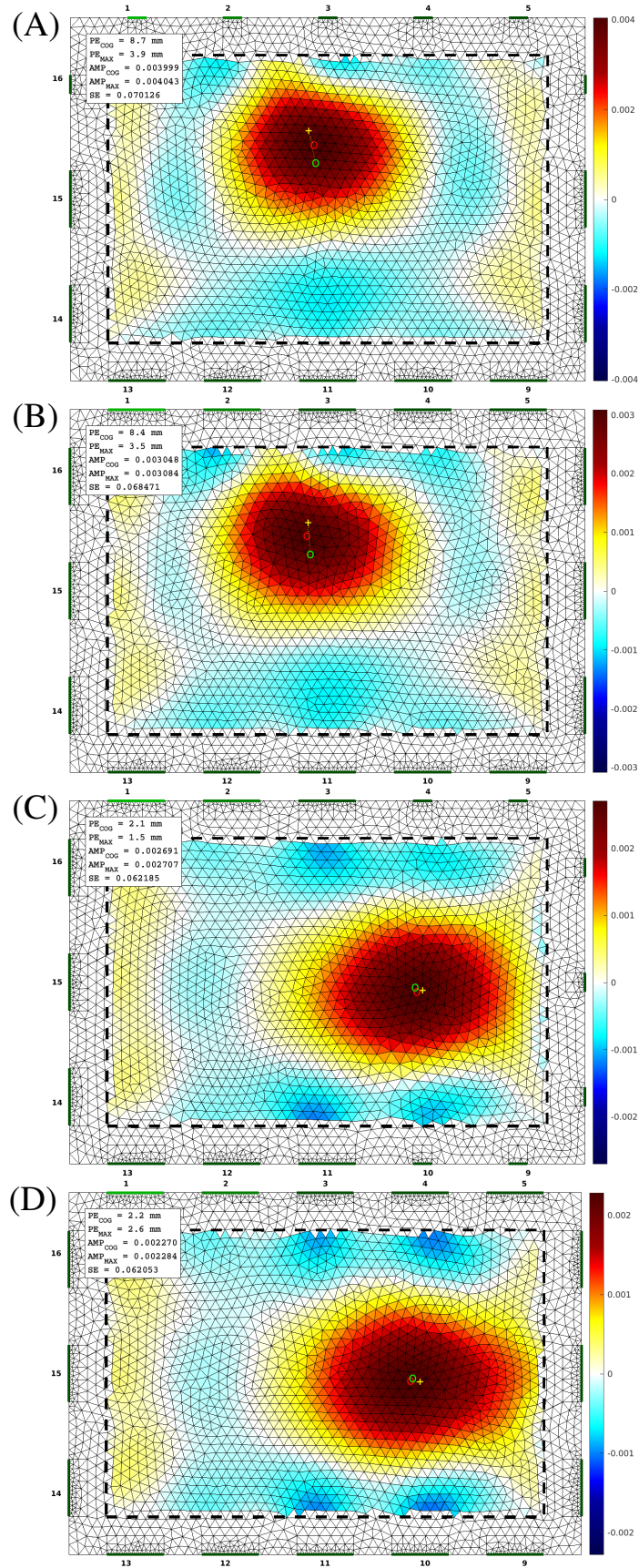


Figure 7.14: Example of reconstructions of point inhomogeneities from differential boundary voltages on an experimental coupon. Inhomogeneity is located at the top of the coupon (T2 position) where it is also “focused” by the electrode configuration (TOP) compared to the uniform electrode distribution (A+B). Next, an example of focusing on the right part of the coupon (inhomogeneity at position R2) compared to a uniform distribution (C+D).

The reconstruction errors or position errors of selected representative combinations of electrode configurations and inhomogeneity positions are summarized in Table 7.4 and 7.5, respectively. The cells with bolded results are the intersection of the inhomogeneity position and the “focused” region (electrode configuration), where the desired improvement can be expected as a result of electrode configuration optimization. The reconstruction error here can be expected to be minimal. For clarity, the percent change with respect to the configuration with uniformly distributed electrodes (commonly used configuration) is given here. Thus, ideally, the bolded portions of the table would contain only negative percentage changes, and conversely, the non-bolded portions would contain positive percentage changes.

Table 7.4: Reconstruction error for homogeneity at left and right positions in combination with appropriate focus.

SOLUTION ERROR	ELEC. FOCUSED AT		
	RIGHT	LEFT	UNFOCUSED
R1	0,056 (+14 %)	0,041 (-17 %)	0,050
R2	0,060 (+17 %)	0,055 (+7 %)	0,050
R3	0,049 (-13 %)	0,058 (+4 %)	0,056
L1	0,056 (+11 %)	0,047 (-8 %)	0,051
L2	0,058 (-1 %)	0,040 (-24 %)	0,058
L3	0,047 (+1 %)	0,039 (-16 %)	0,047

Table 7.5: Position errors (mm) for homogeneity at the left and right positions in combination with the appropriate focus.

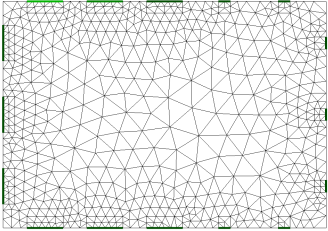
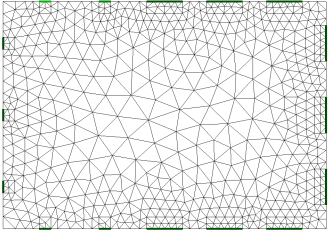
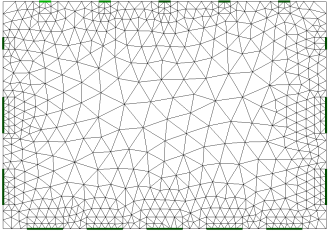
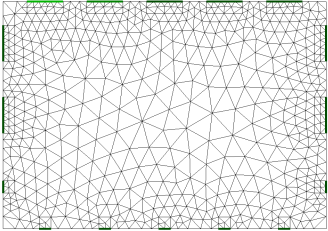
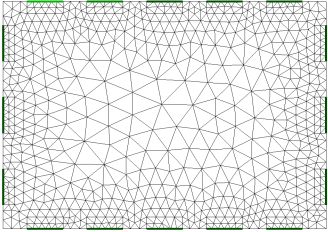
POSITION ERROR	ELEC. FOCUSED AT		
	RIGHT	LEFT	UNFOCUSED
R1	0,51 (-43 %)	1,24 (+38 %)	0,90
R2	2,42 (-41 %)	4,31 (+6 %)	4,08
R3	1,14 (-22 %)	1,42 (-3 %)	1,46
L1	3,76 (+26 %)	3,47 (+16 %)	2,98
L2	0,68 (-23 %)	0,75 (-14 %)	0,87
L3	1,78 (-1 %)	1,76 (-2 %)	1,80

7.4.3 Optimization usefulness evaluation

As can be seen from the percentage values in Tables 7.4 and 7.5, the expected improvement did not occur or occurred only in some cases, and the opposite trend was shown in other cases. If the evaluation was performed only by confirming with positive cases (for both parameters under study), the expected improvement occurred in 8 cases (position error: R1, R2, R3 @ RIGHT, L2, L3 @ LEFT; reconstruction error: R3 @ RIGHT, L1, L3 @ LEFT), while in the remaining 4 cases the trend was even reversed. Of these 8 affirming cases, if the negative cases are further evaluated (the non-fluent parts of the table where a positive value of percentage improvement is expected to confirm the hypothesis), then the other 3 measurements are disqualified (position error: R3 @ RIGHT, L2, L3 @ LEFT). With the inclusion of the disqualification of the affirmation by the opposite cases, there are thus strictly speaking only 5 affirming measurements out of 12.

From the above assessment of the measured data, it cannot be stated clearly that the effects of the optimization have been confirmed by the measurements. The measurements show that the desired effect is lost in the noise. The optimization itself indicated that its impact was not significant, although it was noticeable (a few percent of the position error).

Table 7.3: Position of applied inhomogeneities in further experimental verification of the impact of optimization.

ELECTRODE CONFIGURATION	FINITE-ELEMENT MESH
RIGHT	
LEFT	
TOP	
BOT	
EVEN	

Chapter 8

Discussion and further steps

This dissertation was aimed at the study of the applicability of electrical resistance tomography for the purpose of health monitoring of carbon composite structures in the field of aerospace. As it is one of the first studies in this field, the study focused exclusively on the lowest level elements in terms of the *building block approach*. In the initial phase, the focus was mainly on implementation and instrumentation issues.

8.1 Implementation and instrumentation of ERT

The deployment of ERT in the case of the carbon composite introduced problems, especially in the implementation of the electrodes. The main problem was the robustness, quality, repeatability, and, finally, the cost of electrode production. After mastering the methods of stripping the carbon fibers and then tuning the cleaning of the fibers chemically on the cured coupon, sufficient contact quality (conductive contact over the entire expected area) and repeatability of its production were ensured. By wrapping the thin conductor layer by layer with a conductive paint with pieces of silver in combination with a surface coating with a hard coating, sufficient robustness was ensured. However, the cost of such hand fabrication was considerable and prohibitive for the continuation of the study or even possible deployment in practice. This issue would therefore merit further attention in the future. In particular, it would be advisable to move this step into the manufacturing of the part under consideration itself and thus fully integrate the electrodes into the design during its manufacture.

Attention was also focused on instrumentation. The main obstacle was the unavailability of sufficiently accurate measurement of electrical voltages of a large number of channels with the possibility of automation in combination with current excitation. All this led to the development of a custom multiplexer for this purpose, which allowed to start the necessary experiments. Later this obstacle was removed entirely by the availability of a professional PXI system.

8.2 Barely visible impact detection

Verifying the ability of ERT to detect barely visible impacts was the main objective of the work from the beginning, as this is the most critical damage to the carbon composite. This is because another severe damage propagates from the BVID due to the subsequent life of the structure. The conclusions from Chapter 5.4 show considerable sensitivity and repeatability from low-impact energies, which leads to optimistic recommendations for further study of this issue on higher level elements in terms of the *building block approach*.

8.3 Crack detection

Although classical crack per se is a less common defect in carbon composites, attention has also been paid to this defect. A significant obstacle in the case of crack detection is the commonly used priors used to regularise the inverse problem. These blur the crack so much that it is not possible to decide whether it is a crack or what direction it has. This problem was overcome by deploying an anisotropic Gaussian filter, which allowed control of the size of the blurring based on the reconstruction assumption using commonly used priors. Based on the chosen quality metrics of the reconstructed image, it was shown that it is possible to automate the whole process. Future work could therefore be directed in this direction.

8.4 Optimization of electrode parameters

Trying to optimize the position and size of the electrodes was found to be an essential topic with regard to the next steps of the possible deployment of ERT in the SHM area. Here, the primary motivation was that in the case of geometrically complex structures, it may not always be clear how to position the electrodes and what size to choose. Although the application is aimed at more complex geometries, the work was carried out on the lowest level coupon by default. The optimization runs led to the development of a hypothesis, which was subsequently verified experimentally. Although the optimization suggested a noticeable improvement in PE position error (and possibly SE reconstruction error), the measurements did not fully demonstrate this improvement. The issue was closed with the implications of the optimization being lost in the measurement noise.

Recommendations for further work in this direction may be supported by (unpublished in this paper) efforts to optimize for more complex geometries. While the numerical experiments performed did not show that the effect on more complex geometry was more significant, the models with more complex geometry were not verified in any way for time-related reasons, and their reliability was questionable. Therefore, further work in this direction should include more accurate modeling of more complex geometries in addition to optimization itself.

Chapter 9

Conclusion

This work dealt with the experimental evaluation of the detection capabilities of electrical resistivity tomography in the field of carbon fiber composites with polymer matrix, especially in cases of barely visible impact and crack.

The barely visible impact is one of the most observed defects in this area of the material as it is a source of delamination from interlaminar shear failures and also tensile damage to the fibers. The main danger of delamination is that the laminate matrix loses its ability to stabilize the fibres when they are compressed. In addition to the detectability of barely visible impact, attention was also paid to the detectability of cracking. Crack propagation can start under certain circumstances as a result of barely visible impact. An integral part of the work was the preparation of the instrumentation, where, in addition to the preparation of the measurement chain itself, problems related to the implementation of the electrodes had to be solved. Here, the main obstacle was to acquire the know-how to produce electrodes repeatably, reliably, and with sufficient accuracy. The electrodes were also given attention and specifically the appropriate choice of position and shape (or size, as the investigation was carried out in the 2D domain) of the electrodes in the case of barely visible impact detection. Here, the primary motivation was based on the steps taken in the design of the tomographic system for a possibly more complex geometry of the domain under investigation, where it would be challenging to select the appropriate position and size of the electrodes based on intuition alone, especially in the case where the number of channels for stimulation and measurement is limited by a specific measurement chain.

Electrical resistance tomography was considered in this study as a method for health monitoring of carbon composites and, therefore, as an early warning tool of the occurrence and extent of a failure that already poses a risk. The main feature of electrical resistance tomography, which is the low spatial resolution caused by ill-conditioned inversion, was adopted with the understanding that the detection capabilities of the underlying defects would be studied. The inverse problem (conductivity image reconstruction) was configured with commonly used smoothing priors for detection purposes. In the following, the main conclusions of each objective, presented in Chapter 3, will be briefly summarized, which contribute in a fundamental way to investigate the applicability of electrical resistivity tomography for health monitoring of carbon fiber composites.

9.1 Instrumentation and experimental coupons

For the purpose of electrode fabrication, a chemical cleaning process was designed to chemically clean the composite to expose the fibers to ensure a reliable and repeatable conductive connection between the carbon composite fibers and the electrode, consisting of a conductive coating with silver pieces, which was applied layer by layer, with the conductor being "immersed" into the electrode. Sufficient robustness was achieved by a covering coating with adequate abrasion resistance. In this way, inter-electrode differences in contact resistance of up to 0.5Ω were achieved.

In the initial phase, instrumentation based on proprietary components in combination with stand-alone instruments was designed. The proposed system was based on one dual current source and one instrumentation amplifier. The heart of the system was a multiplexer. The multiplexer had a unit gain error of no more than 6 % for the measurement channels, while crosstalk ranged from 110 dB to 50 dB (0 - 100 kHz). The isolation capabilities of the measurement channels were 100 dB, while those of the excitation channels were 80 dB. The multiplexer implementation allowed active shielding of the measurement channels. The selected instrumentation amplifier, together with other components, exhibited a worst-case dynamic range

of 47 dBc.

In the next phase, the instrumentation was implemented by the PXI modular high-performance platform, where an application for fully automated data acquisition was created with the possibility of configuring any measurement and stimulation pattern.

9.2 Detectability of BVID impact

The experimental evaluation of the BVID detection capability described in Chapter 5 showed that electrical resistance tomography was able to detect the occurrence of barely visible impact (impactions with a dent depth of up to 0.5 mm) with a positional error in the range of 1 to 3 mm (2% of the long side of the specimen). In addition, it has been shown that the influence of the stacking sequence of the composite or of the used prior is minimal.

In the case of investigations on coupons with real impact, reproducible sensitivity to the area of BVID impact was shown. In the case of the quasi-isotropic stacking sequence, the average sensitivity through the used priors was $2.2 \hat{a}/mm^2$, while in the case of the orthotropic stacking sequence, the sensitivity was $1.6 \hat{a}/mm^2$. In the case of the asymmetric stacking sequence, it was found that it did not show a reliable linear dependence of the considered statistical model for assessing the probability of detection.

9.3 Crack detectability

In the case of investigating the ability of electrical resistance tomography to detect cracks in Chapter 6, considerable image sharpening was shown using a Gaussian anisotropic filter. The focusing resulted in approximately a twofold increase in the correlation coefficient compared to the image reconstructed without the filter.

At the same time, the trend of reconstruction error and cross-correlation as a function of the direction and position of the crack assumption, which is the input of the Gaussian anisotropic filter, was investigated. The reconstruction error increased reliably, and the cross-correlation decreased. The reliable trend allows for easy automation of the eventual filter deployment.

9.4 Selection of electrode position and size in case of BVID impact

A data representation, a mutation operator, and a crossover operator were proposed in Chapter 7 to find the optimal position and size of electrodes in a two-dimensional domain for optimization by a genetic algorithm. The mutation method within the genetic algorithm was improved by the climbing algorithm, thus achieving higher explorability while maintaining the basic features of the candidate solution. Using the proposed optimization algorithm, a reduction of the selected fitness function by 40% was achieved, which corresponded to an improvement of 2.5 mm in the best case of the position error, with an average improvement of 1 mm. The solutions found by optimization showed a common feature, based on which it was possible to perform measurements to confirm the observed properties.

Using the measurements, an attempt was made to show that the observed behavior of the electrodes within the optimization shows an improvement in position error. Specifically, it was investigated whether longer electrodes further away from the region of interest and shorter electrodes closer to the region of interest lead to focusing and, therefore, a reduction in position error. Focusing on the right and left parts of the rectangular domain was monitored on a selected dataset compared to the out-of-focus configuration. Only 5 measurements out of 12 confirmed the tested behavior, if we count combinations that should disprove the behavior. The measurements showed that the effects of the optimization or the observed behavior are minimal and rather random, probably due to the influence of measurement noise.

Bibliography - author's impacted articles

- [45] Jan Cagáň. “Hardware implementation of electrical resistance tomography for damage detection of carbon fibre–reinforced polymer composites”. In: *Structural Health Monitoring* 16.2 (Mar. 1, 2017), pp. 129–141.
- [56] Jan Cagáň and Lenka Michalcová. “Impact Damage Detection in CFRP Composite via Electrical Resistance Tomography by Means of Statistical Processing”. In: *Journal of Nondestructive Evaluation* 39.2 (Apr. 22, 2020), p. 38.
- [69] Jan Cagáň et al. “Damage detection in carbon fiber–reinforced polymer composite via electrical resistance tomography with Gaussian anisotropic regularization”. en. In: *Structural Health Monitoring* (Dec. 2018), p. 1475921718820013.

Bibliography - author's other articles

- [44] Jan Cagáň and Jakub Rosler. “Design of Multiplexer for Electrical Impedance Tomography”. In: DANUBIA Adria Symposium on Advances in Experimental Mechanics. Vol. 33. Portorož: Narodna in univerzitetna knjižnica, Ljubljana, Sept. 22, 2016.

Bibliography - other

- [1] Randolph Hanke, Theobald Fuchs, and Norman Uhlmann. “X-ray based methods for non-destructive testing and material characterization”. In: *Nuclear Instruments and Methods in Physics Research A* 591 (June 2008), pp. 14–18.
- [2] P. Bloem et al. “NMR for Non-Destructive Testing of Materials”. In: vol. 1997. Apr. 1997, pp. 135–138.
- [3] Dale L. Bailey et al. “Positron emission tomography. Basic sciences”. French. In: *Journal of Neuro-radiology* 33.4 (2006), pp. 265–265.
- [4] O. Mudanyali et al. “A Microwave Tomographic Approach for Nondestructive Testing of Dielectric Coated Metallic Surfaces”. In: *IEEE Geoscience and Remote Sensing Letters* 5.2 (Apr. 2008), pp. 180–184.
- [5] D. A. Boas et al. “Imaging the body with diffuse optical tomography”. English. In: *IEEE Signal Processing Magazine* 18.6 (2001), pp. 57–75.
- [6] M. Soleimani et al. “A three-dimensional inverse finite-element method applied to experimental eddy-current imaging data”. English. In: *IEEE Transactions on Magnetics* 42.5 (2006), pp. 1560–1567.
- [7] Nanping Zhang. “Electrical impedance tomography based on current density imaging”. English. PhD thesis. 1992.
- [8] M. Nahvi and B. S. Hoyle. “Wideband electrical impedance tomography”. en. In: *Measurement Science and Technology* 19.9 (July 2008). Publisher: IOP Publishing, p. 094011.
- [9] A. Perrone, V. Lapenna, and S. Piscitelli. “Electrical resistivity tomography technique for landslide investigation: A review”. en. In: *Earth-Science Reviews* 135 (Aug. 2014), pp. 65–82.
- [10] Y. F. Mangnall et al. “Applied potential tomography: a new non-invasive technique for assessing gastric function”. In: *Clinical physics and physiological measurement : an official journal of the Hospital Physicists’ Association, Deutsche Gesellschaft für Medizinische Physik and the European Federation of Organisations for Medical Physics* 8 Suppl A. Journal Article (1987). Place: England, p. 119.
- [11] K. Boone, A. M. Lewis, and D. S. Holder. “Imaging of cortical spreading depression by EIT: implications for localization of epileptic foci”. en. In: *Physiological Measurement* 15.2A (May 1994). Publisher: IOP Publishing, A189–A198.
- [12] B. Gowry, A. B. Shahrman, and M. Paulraj. “Electrical bio-impedance as a promising prognostic alternative in detecting breast cancer: A review”. In: *2015 2nd International Conference on Biomedical Engineering (ICoBE)*. Mar. 2015.
- [13] E.J. Woo et al. “Measuring lung resistivity using electrical impedance tomography”. In: *IEEE Transactions on Biomedical Engineering* 39.7 (July 1992). Conference Name: IEEE Transactions on Biomedical Engineering, pp. 756–760.
- [14] Athanasios Baltopoulos et al. “Damage identification in carbon fiber reinforced polymer plates using electrical resistance tomography mapping”. In: *Journal of Composite Materials* 47.26 (Dec. 1, 2013), pp. 3285–3301.
- [15] A. Zarafshani et al. “Using planar electrical impedance tomography as a structural health monitoring method to detect and evaluate the damage to CFRP composite”. In: *2016 IEEE National Aerospace and Electronics Conference (NAECON) and Ohio Innovation Summit (OIS)*. July 2016, pp. 74–79.

- [16] Susanne Nonn et al. “Application of electrical impedance tomography to an anisotropic carbon fiber-reinforced polymer composite laminate for damage localization”. In: *Composites Science and Technology* 160 (2018), pp. 231–236.
- [17] Flavio Calvano, Guglielmo Rubinacci, and Antonello Tamburrino. “Fast methods for shape reconstruction in Electrical Resistance Tomography”. In: *NDT & E International* 46 (Mar. 2012), pp. 32–40.
- [18] Sandra Gschoßmann, Yingjun Zhao, and Martin Schagerl. “Development of data acquisition devices for electrical impedance tomography of composite materials”. In: *Proceedings of the 17th European Conference on Composite Materials ECCM17*. Vol. 17. Germany, Munich, Aug. 2016, p. 8.
- [19] Kenneth J. Loh et al. “Carbon Nanotube Sensing Skins for Spatial Strain and Impact Damage Identification”. en. In: *Journal of Nondestructive Evaluation* 28.1 (Mar. 2009), pp. 9–25.
- [20] Donghai Zhang et al. “Assessment of transverse impact damage in GF/EP laminates of conductive nanoparticles using electrical resistivity tomography”. In: *Composites Part A: Applied Science and Manufacturing* 43.9 (Sept. 2012), pp. 1587–1598.
- [21] B. R. Loyola et al. “Spatial Sensing Using Electrical Impedance Tomography”. In: *IEEE Sensors Journal* 13.6 (June 2013), pp. 2357–2367.
- [22] Tyler N. Tallman et al. “Damage detection via electrical impedance tomography in glass fiber/epoxy laminates with carbon black filler”. en. In: *Structural Health Monitoring* 14.1 (Jan. 2015), pp. 100–109.
- [23] A. Baltopoulos et al. “Exploiting carbon nanotube networks for damage assessment of fiber reinforced composites”. In: *Composites Part B: Engineering* 76 (July 2015), pp. 149–158.
- [24] T. N. Tallman et al. “On the inverse determination of displacements, strains, and stresses in a carbon nanofiber/polyurethane nanocomposite from conductivity data obtained via electrical impedance tomography”. en. In: *Journal of Intelligent Material Systems and Structures* 28.18 (Nov. 2017), pp. 2617–2629.
- [25] T. N. Tallman and J. A. Hernandez. “The effect of error and regularization norms on strain and damage identification via electrical impedance tomography in piezoresistive nanocomposites”. In: *NDT & E International* 91 (Oct. 2017), pp. 156–163.
- [26] A. J. Thomas et al. “Damage detection in self-sensing composite tubes via electrical impedance tomography”. en. In: *Composites Part B: Engineering* 177 (Nov. 2019), p. 107276.
- [27] Steven L. Donaldson and Daniel B. Miracle. *ASM Handbook Composites Volume 21*. English. 10 edition. Materials Park, Ohio: ASM International, Dec. 2001.
- [28] Douglas Gough. *The success story of the transfer and development of methods from geophysics to helioseismology*. 1996.
- [29] M. Glidewell and K. T. Ng. “Anatomically constrained electrical impedance tomography for anisotropic bodies via a two-step approach”. eng. In: *IEEE transactions on medical imaging* 14.3 (1995), pp. 498–503.
- [30] M. Vauhkonen et al. “Electrical impedance tomography with basis constraints”. In: *Inverse Problems* 13.2 (1997), p. 523.
- [31] M. Vauhkonen et al. “Tikhonov regularization and prior information in electrical impedance tomography”. In: *IEEE Transactions on Medical Imaging* 17.2 (Apr. 1998). Conference Name: IEEE Transactions on Medical Imaging, pp. 285–293.
- [32] M. Cheney et al. “NOSER: An Algorithm for Solving the Inverse Conductivity Problem”. In: *International Journal of Imaging Systems & Technology* 2.2 (1990), pp. 66–75.
- [33] A. Adler and R. Guardo. “Electrical impedance tomography: regularized imaging and contrast detection”. In: *IEEE Transactions on Medical Imaging* 15.2 (Apr. 1996), pp. 170–179.
- [34] David C. Dobson and Curtis R. Vogel. “Convergence of an Iterative Method for Total Variation Denoising”. In: *SIAM Journal on Numerical Analysis* 34.5 (1997). Publisher: Society for Industrial and Applied Mathematics, pp. 1779–1791.
- [35] Giusti. *Minimal Surfaces and Functions of Bounded Variation*. en. Google-Books-ID: dNgsmArDoeQC. Springer Science & Business Media, Jan. 1984.

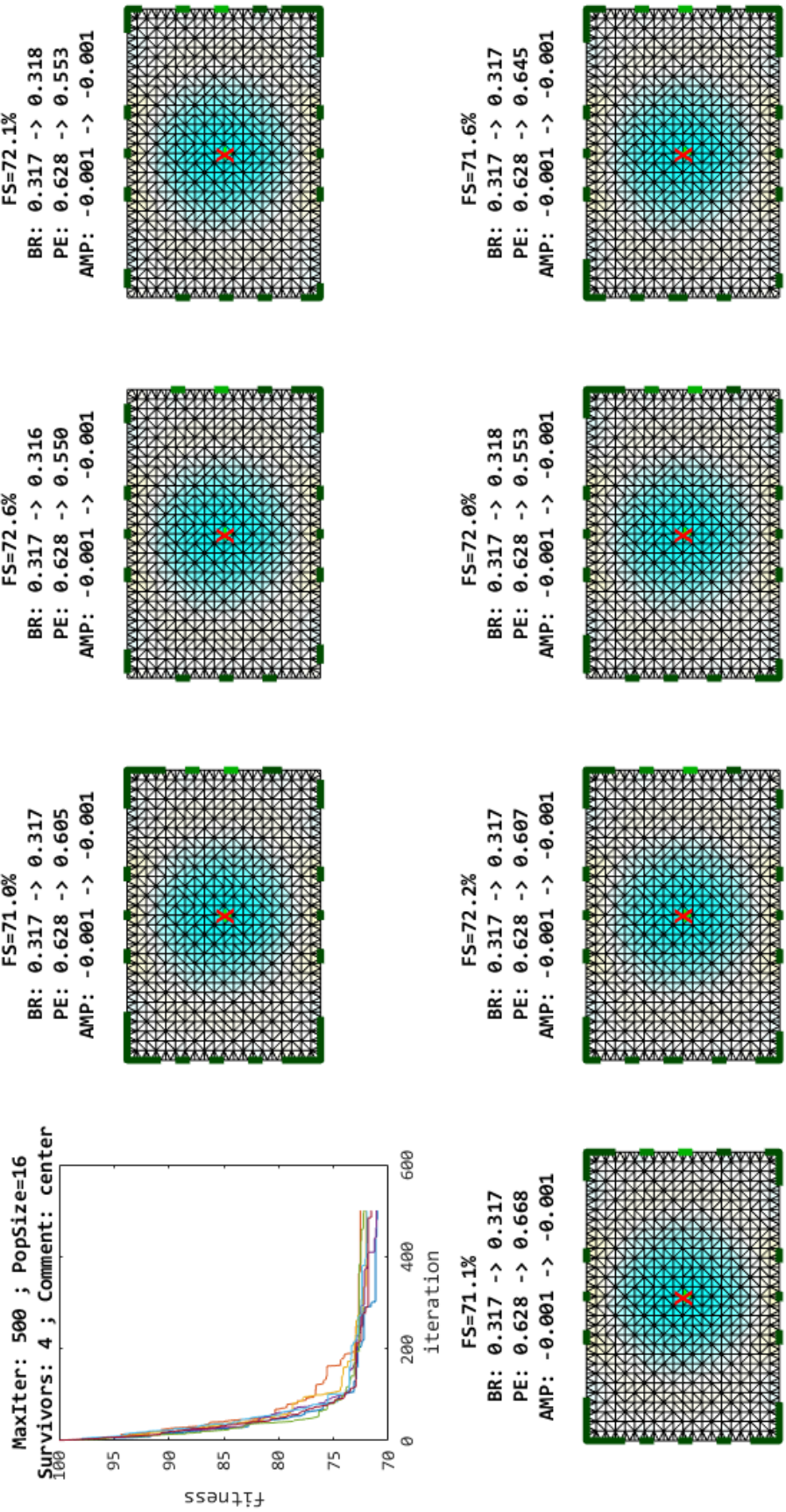
- [36] Erkki Somersalo et al. “Impedance imaging and Markov chain Monte Carlo methods”. In: *Computational, Experimental, and Numerical Methods for Solving Ill-Posed Inverse Imaging Problems: Medical and Nonmedical Applications*. Vol. 3171. SPIE, Dec. 1997, pp. 175–185.
- [37] Nick Polydorides and William R. B. Lionheart. “A Matlab toolkit for three-dimensional electrical impedance tomography: a contribution to the Electrical Impedance and Diffuse Optical Reconstruction Software project”. en. In: *Measurement Science and Technology* 13.12 (2002), p. 1871.
- [38] *Process Tomography: Principles, Techniques and Applications*. English. 1 edition. Oxford ; Boston: Butterworth-Heinemann, Aug. 1995.
- [39] D. Isaacson. “Distinguishability of Conductivities by Electric Current Computed Tomography”. In: *IEEE Transactions on Medical Imaging* 5.2 (June 1986), pp. 91–95.
- [40] Andy Adler. *Strange Effect: Opposite vs Adjacent measurement/stimulation*. URL: http://eidors3d.sourceforge.net/tutorial/strange_effects/opposite_meas.shtml (visited on 10/23/2017).
- [41] D. Gisser, D. Isaacson, and J. Newell. “Electric current computed tomography eigenvalues”. In: (1990).
- [42] R. A. Williams and M. S. Beck. *Process Tomography: Principles, Techniques and Applications*. English. 1 edition. Oxford ; Boston: Butterworth-Heinemann, Aug. 1995.
- [43] Shijie Sun et al. “Signal Demodulation Methods for Electrical Tomography: A Review”. In: *IEEE Sensors Journal* 19.20 (Oct. 2019). Conference Name: IEEE Sensors Journal, pp. 9026–9035.
- [46] Tsung-Chin Hou, Kenneth J. Loh, and Jerome P. Lynch. “Spatial conductivity mapping of carbon nanotube composite thin films by electrical impedance tomography for sensing applications”. In: *Nanotechnology* 18.31 (2007), p. 315501.
- [47] Daojun Wang and D. D. L. Chung. “Comparative evaluation of the electrical configurations for the two-dimensional electric potential method of damage monitoring in carbon fiber polymer–matrix composite”. In: *Smart Materials and Structures* 15.5 (2006), p. 1332.
- [48] Yoshiro Suzuki et al. “Impact-damage visualization in CFRP by resistive heating: Development of a new detection method for indentations caused by impact loads”. In: *Composites Part A: Applied Science and Manufacturing* 43.1 (Jan. 2012), pp. 53–64.
- [49] Kensuke Suzuki Akira Todoroki. “Durability Estimates of Copper Plated Electrodes for Self-sensing CFRP Composites”. In: *Journal of Solid Mechanics and Materials Engineering* 4.6 (2010), pp. 610–620.
- [50] Mathias Haingartner et al. “Improved current injection pattern for the detection of delaminations in carbon fiber reinforced polymer plates using electrical impedance tomography”. In: *Structural Health Monitoring* (Dec. 31, 2020). Publisher: SAGE Publications, p. 1475921720972308.
- [51] Khaled Almuhammadi et al. “Laser-based surface preparation of composite laminates leads to improved electrodes for electrical measurements”. In: *Applied Surface Science* 359 (Dec. 30, 2015), pp. 388–397.
- [52] J. Šedek. “Modelling the failure of near-edge impacted carbon fibre-reinforced composite subjected to shear loading”. en. In: *IOP Conference Series: Materials Science and Engineering* 369 (May 2018), p. 012035.
- [53] Jakub Šedek and Petr Bělský. “Numerical evaluation of barely visible impact damage in a carbon fibre-reinforced composite panel with shear loading”. In: *WIT Transactions on Engineering Sciences* 116 (2017), pp. 73–85.
- [54] Martin Kadlec and Roman Růžek. “A Comparison of Laser Shearography and C-Scan for Assessing a Glass/Epoxy Laminate Impact Damage”. In: *Applied Composite Materials* 19.3 (2012), pp. 393–407.
- [55] Francesco Ciampa et al. “Recent Advances in Active Infrared Thermography for Non-Destructive Testing of Aerospace Components”. English. In: *Sensors; Basel* 18.2 (2018), p. 609.
- [57] Ruediger Schueler, Shiv P. Joshi, and Karl Schulte. “Damage detection in CFRP by electrical conductivity mapping”. In: *Composites Science and Technology* 61.6 (May 2001), pp. 921–930.
- [58] William R. B. Lionheart and Kyriakos Paridis. “Finite elements and anisotropic EIT reconstruction”. In: *Journal of Physics: Conference Series* 224.1 (2010), p. 012022.

- [59] Paridis Kyriakos. “The inverse conductivity problem: anisotropy, finite elements and resistor networks”. PhD thesis. School of Mathematics: The University of Manchester, 2013.
- [60] D. C. Barber and B. H. Brown. “Errors in reconstruction of resistivity images using a linear reconstruction technique”. en. In: *Clinical Physics and Physiological Measurement* 9.4A (Nov. 1988), pp. 101–104.
- [61] William R. B. Lionheart. “EIT Reconstruction Algorithms: Pitfalls, Challenges and Recent Developments”. In: *Physiological Measurement* 25.1 (Feb. 2004). arXiv: physics/0310151, pp. 125–142.
- [62] SWISS-COMPOSITE. *Style 450-5 Carbon Fabric for Aerospace Applications*. Feb. 2020.
- [63] Josef Krautkrämer and Herbert Krautkrämer. *Ultrasonic Testing of Materials*. 4th ed. Berlin Heidelberg: Springer-Verlag, 1990.
- [64] *MIL-HDBK-1823A: Nondestructive Evaluation System Reliability Assessment*. English. Apr. 2009.
- [65] Emile Greenhalgh. *Failure Analysis and Fractography of Polymer Composites*. en. Elsevier, Sept. 2009.
- [66] Bhagwan D. Agarwal, Lawrence J. Broutman, and K. Chandrashekhara. *Analysis and Performance of Fiber Composites*. English. 4 edition. Hoboken, NJ: Wiley, Oct. 2017.
- [67] L. Daudeville, O. Allix, and P. Ladevèze. “Delamination analysis by damage mechanics: Some applications”. In: *Composites Engineering* 5.1 (Jan. 1995), pp. 17–24.
- [68] Zeng Shen. “Characterisation of Low Velocity Impact Response in Composite Laminates”. en. PhD thesis. Hertfordshire (UK): University of Hertfordshire, 2014.
- [70] A. Borsic, W. R. B. Lionheart, and C. N. McLeod. “Generation of anisotropic-smoothness regularization filters for EIT”. In: *IEEE Transactions on Medical Imaging* 21.6 (June 2002), pp. 579–587.
- [71] Andy Adler et al. “GREIT: a unified approach to 2D linear EIT reconstruction of lung images”. en. In: *Physiological Measurement* 30.6 (2009), S35.
- [72] Kevin Paulson, William Breckon, and Michael Pidcock. “A hybrid phantom for electrical impedance tomography”. en. In: *Clinical Physics and Physiological Measurement* 13.A (1992), p. 155.
- [73] Y. Wang et al. “Simulation Study of Electrode System Optimization in Electrical Impedance Tomography”. In: *2010 4th International Conference on Bioinformatics and Biomedical Engineering (iCBBE)*. June 2010, pp. 1–4.
- [74] Luis Waldo Escalona Galvis, Paulina Diaz-Montiel, and Satchi Venkataraman. “Optimal Electrode Selection for Electrical Resistance Tomography in Carbon Fiber Reinforced Polymer Composites”. en. In: *Materials* 10.2 (Feb. 2017), p. 125.
- [75] N. HyvÄrinen, A. SeppÄnen, and S. Staboulis. “Optimizing Electrode Positions in Electrical Impedance Tomography”. In: *SIAM Journal on Applied Mathematics* 74.6 (Jan. 2014), pp. 1831–1851.
- [76] Sean Luke. *Essentials of Metaheuristics*. English. lulu.com, June 2013.

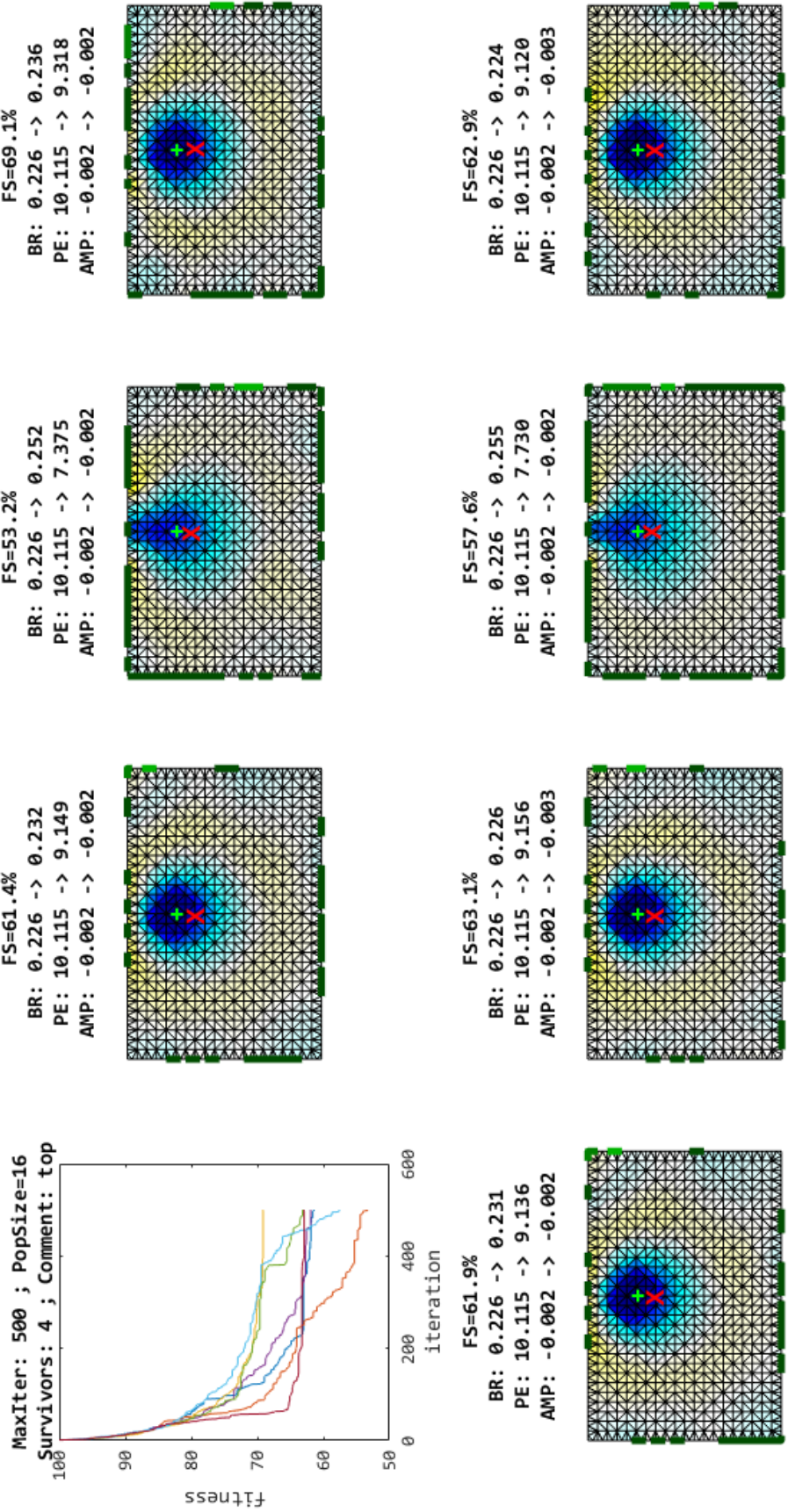
Appendix A

Example of GA population

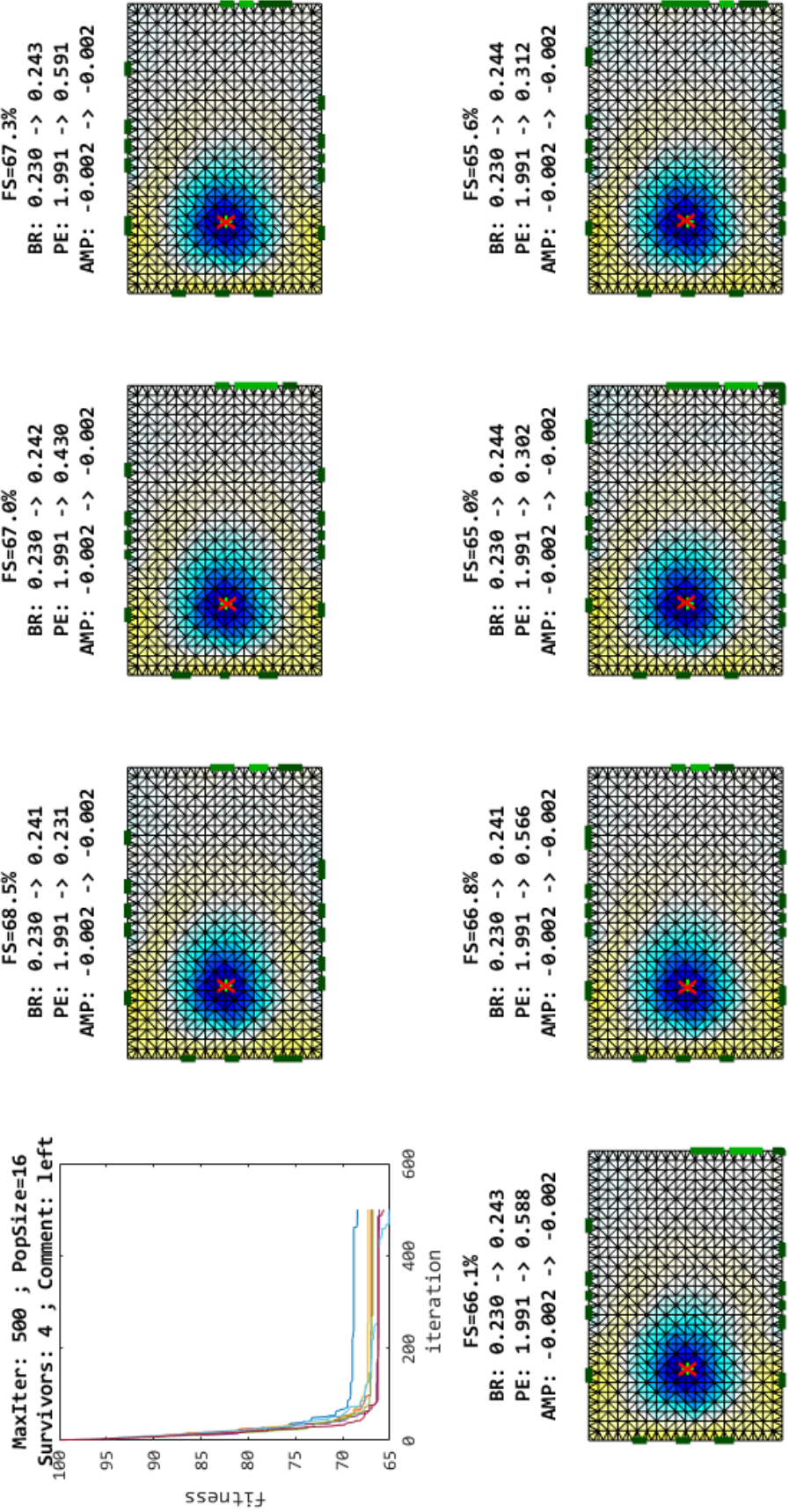
A.1 Position of inhomogeneity in the CENTER



A.2 Position of inhomogeneity on the TOP



A.3 Position of inhomogeneity on the LEFT



A.4 Position of inhomogeneity on the RIGHT

